Materials Development for All-Solid-State Battery Electrolytes

by

Weimin Wang

A dissertation submitted in partial fulfillment
of the requirements for the degree of
Doctor of Philosophy
(Materials Science and Engineering)
in the University of Michigan
2017

Doctoral Committee:

Professor John Kieffer, Chair
Assistant Professor John T. Heron
Professor Richard M. Laine
Professor Johannes W. Schwank

Weimin Wang

weimin@umich.edu

ORCID iD: 0000-0002-8144-0547

TABLE OF CONTENT

LIST OF FIGURES

LIST OF TABLES

ABSTRACT

Solid electrolytes in all solid-state batteries, provide higher attainable energy density and improved safety. Ideal solid electrolytes require high ionic conductivity, a high elastic modulus to prevent dendrite growth, chemical compatibility with electrodes, and ease of fabrication into thin films. Although various materials types, including polymers, ceramics, and composites, are under intense investigation, unifying design principles have not been identified. In this thesis, we study the key ion transport mechanisms in relation to the structural characteristics of polymers and glassy solids, and apply derived material design strategies to develop polymer-silica hybrid materials with improved electrolyte performance characteristics.

Poly(ethylene) oxide-based solid electrolytes containing ceramic nanoparticles are attractive alternatives to liquid electrolytes for high-energy density Li batteries. We compare the effect of $Li_{1.3}Al_{0.3}Ti_{1.7}(PO_4)_3$ active nanoparticles, passive TiO_2 nanoparticles and fumed silica. Up to two orders of magnitude enhancement in ionic conductivity is observed for composites with active nanoparticles, attributed to cation migration through a percolating interphase region that develops around the active nanoparticles, even at low nanoparticle loading.

We investigate the structural origin of elastic properties and ionic migration mechanisms in sodium borosilicate and sodium borogermanate glass electrolyte system. A new statistical thermodynamic reaction equilibrium model is used in combination with data from nuclear magnetic resonance and Brillouin light scattering measurements to determine network structural unit fractions. The highly coordinated structural units are found to be predominantly responsible for effective mechanical load transmission, by establishing three-dimensional covalent connectivity. A strong correlation exists between bulk modulus and the activation energy for ion conduction. We describe the activated process in glasses as involving a jump by the migrating cation and transient reversible isotropic displacement of atoms in the immediate vicinity, and express the activation energy as a sum of Coulomb and elastic terms. By fitting our experimental data to this model, we find that the number of affected atoms in the vicinity ranges between 20 and 30. Furthermore, elastic deformations in ion jumping are almost purely hydrostatic and hardly shear. Considering that the energy required for the cation jump is made available by concentrating thermal phonons at the jump site, we establish a relationship between structural stiffness and activation energy. Moreover, the more atoms that partake in the cation jump, the more degrees of freedom for atomic motion can be relied upon to achieve the required net outward expansion to facilitate the passage of the jumping cation, lowering the activation energy.

To combine the flexibility of polymers and the good mechanical and electrochemical properties of silica, we use sol-gel methods for fabricating silica-

based hybrid organic-inorganic electrolytes. Polyethylene glycol is covalently grafted onto the silica backbone as the organic filler that provides the environment for ion conduction. We developed synthesis methods in which grafting and polycondensation occur concurrently, or the grafting occurs after the silica backbone has formed. Small angle x-ray scattering measurements reveal that different structures are achieved depending on the method used. The two-step procedure allows for a larger amount of conducting polymer to be embedded into network pores than in the one-pot method. This greatly enhances the ionic conductivity without sacrificing mechanical stability afforded by the continuous silica backbone. Here we provide a cumulative account of a systematic materials design efforts, in which we sequentially implement several important design aspects to identify their respective importance and influence on the materials performance characteristics.

CHAPTER 1

INTRODUCTION

1.1 Background and Motivation

In light of the rapidly increasing global energy needs, the associated CO_2 emission, and the global warming trend, efficient, clean, and sustainable energy sources are needed. Renewable energy such as solar and wind power are intermittent and are not reliably synchronized with the energy demand, which motivates the development of efficient energy storage devices. Batteries are among the most versatile and economically viable devices, whose application can be from small electronic devices, to electric vehicles, and large grid scale energy storage.

The essential components of a battery are the anode, the cathode, and the electrolyte. As the electrodes are where the oxidation and reduction happens, the role of the electrolyte is to effectively separate the redox pairs, selectively mediate the transport of specific ions that establish the electrochemical process responsible for energy release or storage, and provide sufficient structural stiffness to ensure the mechanical stability of the device. Currently, organic solvents are used as liquid electrolytes in most commercially available batteries

due to their high transport rate, but they are flammable, require careful containment, and cannot be load bearing. Foremost, they can only accommodate a relatively small potential difference between anode and cathode, limiting the energy and power capacity of the battery. [1–3] In lithium ion batteries, development of solid electrolytes not only solves these problems but also provides the possibility of using lithium metal as the anode. Metallic lithium has the most negative reduction potential, high specific capacity (3,860 mAh g^{-1}), and it has low atomic weight. It therefore constitutes the anode with the highest theoretical energy capacity. [4–6] Unfortunately, lithium exhibits poor chemical compatibility with liquid electrolytes, and upon repeated charge cycling the metal tends to deposit on the anode in the form of dendrites that protrude into the electrolyte and eventually cause catastrophic failure of the battery by short circuiting with the cathode. [4, 7–10] In order to take advantage of the large energy density of metallic lithium, it is necessary to develop electrolyte materials that are chemically compatible with both electrodes, offer high mobility and large transference numbers for Li+ ions, and possess sufficiently high mechanical rigidity. According to Monroe and Newman [11], the shear moduli of electrolyte material needs to be at least ~7 GPa to suppress dendrite growth on the anode.

The primary figure of merit to evaluate the suitability of a solid electrolyte for battery applications is the conductivity. Ionic conductivities exceeding 10^{-4} $S \cdot cm^{-1}$ at room temperature are desired. While high ion mobility is inherent to liquids, it is not so trivial to achieve in solid or composite electrolytes. Thus, in developing novel electrolytes, efforts have been predominantly focused on maximizing ion

transport rates. One additional factor that crucially affects the performance of an electrolyte is its mechanical rigidity. Electrolytes that are mechanically rigid allow simple design and easy manufacturing by eliminating the need for elaborate seals, separators and support structures.

Different categories of materials have been studied for this application, from inorganic compounds to organic chain-like polymers and from crystalline to amorphous. Faraday observed high ionic mobility in inorganic crystalline compounds as early as 1832. [12] The structures of these superionic conductors, which are materials with conductivity higher than 10^{-3} $S \cdot cm^{-1}$, such as Na super ionic conductor (NASICON)_ [13–15], Li super ionic conductor (LISICON) [16–18], Lithium phosphorus oxynitride (LIPON), [19–21] exhibit interstitial channels that are pathways for ion migration. Glasses, the structures of which exhibit atomic disorder similar to that of liquid, provide isotropy and more free volume for ions to migrate, making them candidates for solid battery electrolytes. [22–25] Heat treatment of these glasses yields glass ceramic materials that have both highly conducting crystalline regions and large volume fractions of strongly disordered and spatially percolating interfacial regions separating crystallites from the residual glass matrix. [24, 26–28] On the other hand, polymer electrolytes, which are organic chain-like molecules containing a salt that serves as the cation donor, demonstrate good electrochemical stability and structural flexibility. This allows for the material to adapt to volume changes of the electrodes upon charge or discharge, and maintain low interfacial resistance for charge carrier transfer. [29–33] Relaxation and segmental motion of the solvent chains are the key factors that

enable cation transport. Modifications are made to the pristine polymer such as addition of oxide particles (e.g., Al_2O_3, SiO_2, TiO_2, ZrO_2), copolymerization, or crosslinking to reduce the crystallization tendency, which improves its chain mobility and ionic conductivity. [34–37] This led to the exploration of various composite concepts for materials design, including hybrid organic-inorganic materials.

1.2 Project Overview

Evidently, ion conduction can be achieved in solids in seemingly disparate ways. Multifarious studies have been done in this field to explore materials with high ionic conductivity, however, the relationship between structure and mechanisms of ion migration are not sufficiently understood. Instead of solely pursuing high ionic mobility, what is more important is to understand the underlying mechanisms and identify a unified set of design criteria. As long as this knowledge is lacking, it is impossible to ascertain what the upper limit for ionic conductivity may be, and no clear design target can be identified. This thesis not only focuses on development of materials that are of high conductivity but also aims to advance necessary fundamental understanding, by elucidating the mechanistic underpinnings of the aforementioned materials design concepts.

The overall goal of this thesis is to develop ionic conducting electrolytes that exhibit high cation conductivity and that are mechanically rigid enough to suppress dendrite growth and safely separate electrodes in self-supporting device structures. Several categories of materials are studied, with the focus on

polymers, glassy materials, and polymer-silica hybrid materials. Specific objectives and milestones towards accomplishing this goal are:

- Gain a fundamental understanding of ion transport within polymer based composite electrolytes
- Explore structure-property relationships of oxide glass electrolytes, as well the ion transport mechanism
- Identify synthesis routes for the fabrication of the organic-inorganic materials based on sol-gel chemistry to achieve the desired self-assembly behavior
- Design organic-inorganic hybrid electrolytes that allow for parameters control so that an optimal combination of structural backbone and conducting phase chemistry can be achieved. Obtain optimal parameters for simultaneously achieving high cation mobility and mechanical stability.

1.3 Thesis Overview

The contents of the thesis are divided into eight chapters. The results of three main projects are presented in Chapters 4, 5, 6, and 7.

Chapter 2 gives the background and fundamentals of battery electrolyte materials. A comprehensive literature review of major categories of solid electrolytes that are related to this study is provided, including polymer, polymer composite, and glass electrolytes.

Chapter 3 presents an overview of characterization techniques used in this work as well as the sol-gel synthesis method used for organic-inorganic hybrid

materials. Descriptions are provided for Brillouin light scattering used to measure micromechanical properties, dielectric impedance spectroscopy employed as the characterization of ionic transport properties, and small angle X-ray scattering used for structural characterization.

Chapter 4 presents a comparative study of polymer ceramic nanocomposite electrolytes made with active amorphous $Li_{1.3}Al_{0.3}Ti_{1.7}(PO_4)_3$ (LATP) nanoparticles and passive TiO_2 and SiO_2 in PEO. We performed a parametric study by varying the lithium concentration, particle loading and PEO molecular weight with different ceramic fillers. Results of structural and chemical characterization as well as a proposed conductivity-concentration model for such active nanocomposite are presented.

In Chapter 5, two mixed-network former glass systems, sodium borosilicate $0.2Na_2O + 0.8[xBO_{1.5} + (1-x)SiO_2]$ and sodium borogermanate $0.2Na_2O + 0.8[xBO_{1.5} + (1-x)GeO_2]$ glasses, are investigated. We present a newly developed statistical thermodynamic reaction equilibrium model. The model allows one to determine the relative proportions of all network structural units with the help of NMR and Brillouin light scattering results, is presented. This new analysis reveals the structural origin of the anomalous maxima in elastic moduli with increasing atomic number density.

In chapter 6, the ionic transport properties of the aforementioned two glass systems are studied. A heavily modified Anderson-Stuart model is used to further elucidate the cation migration mechanisms in these glasses, simultaneously accounting for behaviors in ion mobility and structural rigidity. The elastic

deformations of the structure surrounding the migrating cation are found to be purely hydrostatic. A detailed discussion on the source and the effect of the activation for this ion jump process is presented.

Chapter 7 moves on to another class of materials, organic-inorganic hybrid electrolytes. In this chapter, the synthesis methods for two different types of organic-inorganic hybrid electrolytes are introduced. The results of a systematic study on the effect of polymer weight fraction and polymer molecular weight on various properties are presented. The structure-property relations are discussed.

Chapter 8 gives a final summary of all the chapters, including major findings and achievements in this thesis study. An outlook for future research in this field is suggested based on the insights obtained from this work.

1.4 References

1. M. Armand, F. Endres, D.R. Macfarlane, H. Ohno & B. Scrosati, 'Ionic-liquid materials for the electrochemical challenges of the future,' *Nature Materials* **8**, 621 (2009)

2. J.B. Goodenough, 'Rechargeable batteries: Challenges old and new,' *Journal of Solid State Electrochemistry* **16**, 2019 (2012)

3. W.H. Meyer, 'Polymer electrolytes for lithium ion batteries,' *Advanced Materials* **10**, 439 (1998)

4. D. Aurbach & Y. Cohen, 'The application of atomic force microscopy for the study of li deposition processes,' *Journal of The Electrochemical Society* **143**, 3525 (1996)

5. P.G. Bruce, S.A. Freunberger, L.J. Hardwick & J.-M. Tarascon, 'Li-o2 and li-s batteries with high energy storage,' *Nature Materials* **11**, 19 (2012)

6. M.S. Whittingham, 'History, evolution, and future status of energy storage,' *Proceedings of the IEEE* **100**, 1518 (2012)

7. D. Aurbach, E. Zinigrad, Y. Cohen & H. Teller, 'A short review of failure mechanisms of lithium metal and lithiated graphite anodes in liquid electrolyte solutions,' *Solid State Ionics* **148**, 405 (2002)

8. R.R. Chianelli, 'Microscopic studies of transition metal chalcogenides,' *Journal of Crystal Growth* **34**, 239 (1976)

9. L. Gireaud, S. Grugeon, S. Laruelle, B. Yrieix & J.-M. Tarascon, 'Lithium metal stripping/plating mechanisms studies: A metallurgical approach,' *Electrochemistry Communications* **8**, 1639 (2006)

10. C. Monroe & J. Newman, 'The impact of elastic deformation on deposition kinetics at lithium/polymer interfaces,' *Journal of The Electrochemical Society* **152**, A396 (2005)

11. C. Monroe & J. Newman, 'The impact of elastic deformation on deposition kinetics at lithium/polymer interfaces,' *Journal of The Electrochemical Society* **152**, A396 (2005)

12. M. Faraday, 'Experimental researches in electricity,' *Philosophical transactions of the Royal Society of London* **122**, 125 (1832)

13. S. Hasegawa, N. Imanishi, T. Zhang, J. Xie, A. Hirano, Y. Takeda & O. Yamamoto, 'Study on lithium/air secondary batteries—stability of NASICON-type lithium ion conducting glass–ceramics with water,' *Journal Of Power Sources* **189**, 371 (2009)

14. K.S. Nanjundaswamy, A.K. Padhi, J.B. Goodenough, S. Okada, H. Ohtsuka, H. Arai & J. Yamaki, 'Synthesis, redox potential evaluation and electrochemical characteristics of NASICON-related-3d framework compounds,' *Solid State Ionics* **92**, 1 (1996)

15. A.K. Padhi, K.S. Nanjundaswamy, C. Masquelier & J.B. Goodenough, 'Mapping of transition metal redox energies in phosphates with NASICON structure by lithium intercalation,' *Journal of the Electrochemical Society* **144**, 2581 (1997)

16. P.G. Bruce & A.R. West, 'The a c conductivity of polycrystalline LISICON, li2+ 2x zn1- x geo4, and a model for intergranular constriction resistances,' *Journal of The Electrochemical Society* **130**, 662 (1983)

17. R. Kanno, T. Hata, Y. Kawamoto & M. Irie, 'Synthesis of a new lithium ionic conductor, thio-LISICON–lithium germanium sulfide system,' *Solid State Ionics* **130**, 97 (2000)

18. R. Kanno & M. Murayama, 'Lithium ionic conductor thio-LISICON: The Li_2S GeS_2 P_2S_5 system,' *Journal of The Electrochemical Society* **148**, A742 (2001)

19. N.J. Dudney, 'Addition of a thin-film inorganic solid electrolyte (LIPON) as a protective film in lithium batteries with a liquid electrolyte,' *Journal of Power Sources* **89**, 176 (2000)

20. Y. Hamon, A. Douard, F. Sabary, C. Marcel, P. Vinatier, B. Pecquenard & A. Levasseur, 'Influence of sputtering conditions on ionic conductivity of LIPON thin films,' *Solid State Ionics* **177**, 257 (2006)

21. W.C. West, J.F. Whitacre & J.R. Lim, 'Chemical stability enhancement of lithium conducting solid electrolyte plates using sputtered LIPON thin films,' *Journal Of Power Sources* **126**, 134 (2004)

22. S. Komaba, W. Murata, T. Ishikawa, N. Yabuuchi, T. Ozeki, T. Nakayama, A. Ogata, K. Gotoh & K. Fujiwara, 'Electrochemical na insertion and solid electrolyte interphase for hard carbon electrodes and application to na ion batteries,' *Advanced Functional Materials* **21**, 3859 (2011)

23. C.-H. Lee, K.H. Joo, J.H. Kim, S.G. Woo, H.-J. Sohn, T. Kang, Y. Park & J.Y. Oh, 'Characterizations of a new lithium ion conducting $Li_2O–SeO_2–B_2O_3$ glass electrolyte,' *Solid State Ionics* **149**, 59 (2002)

24. J. Swenson & L. Börjesson, 'Correlation between free volume and ionic conductivity in fast ion conducting glasses,' *Physical Review Letters* **77**, 3569 (1996)

25. K. Takada, N. Aotani, K. Iwamoto & S. Kondo, 'Electrochemical behavior of Li_xMO_2 (M= Co, Ni) in all solid state cells using a glass electrolyte,' *Solid State Ionics* **79**, 284 (1995)

26. A. Hayashi, K. Noi, A. Sakuda & M. Tatsumisago, 'Superionic glass-ceramic electrolytes for room-temperature rechargeable sodium batteries,' *Nature Communications* **3**, 856 (2012)

27. D.R. Macfarlane, J. Huang & M. Forsyth, 'Lithium-doped plastic crystal electrolytes exhibiting fast ion conduction for secondary batteries,' *Nature* **402**, 792 (1999)

28. F. Mizuno, A. Hayashi, K. Tadanaga & M. Tatsumisago, 'High lithium ion conducting glass-ceramics in the system Li_2S-P_2S_5,' *Solid State Ionics* **177**, 2721 (2006)

29. K.M. Abraham, Z. Jiang & B. Carroll, 'Highly conductive PEO-like polymer electrolytes,' *Chemistry of Materials* **9**, 1978 (1997)

30. G.B. Appetecchi, G. Dautzenberg & B. Scrosati, 'A new class of advanced polymer electrolytes and their relevance in plastic like, rechargeable lithium batteries,' *Journal of The Electrochemical Society* **143**, 6 (1996)

31. G.B. Appetecchi, F. Croce, G. Dautzenberg, M. Mastragostino, F. Ronci, B. Scrosati, F. Soavi, A. Zanelli, F. Alessandrini & P.P. Prosini, 'Composite polymer

electrolytes with improved lithium metal electrode interfacial properties I. Elechtrochemical properties of dry PEO Li_x systems,' *Journal of the Electrochemical Society* **145**, 4126 (1998)

32. B. Scrosati & J. Garche, 'Lithium batteries: Status, prospects and future,' *Journal of Power Sources* **195**, 2419 (2010)

33. J.H. Shin, K.W. Kim, H.J. Ahn & J.H. Ahn, 'Electrochemical properties and interfacial stability of $(PEO)_{10}$ $LiCF_3SO_3$–Ti_nO_{2n-1} composite polymer electrolytes for lithium/sulfur battery,' *Materials Science and Engineering: B* **95**, 148 (2002)

34. F. Capuano, F. Croce & B. Scrosati, 'Composite polymer electrolytes,' *Journal of the Electrochemical Society* **138**, 1918 (1991)

35. J.R. MacCallum & C.A. Vincent, *Polymer Electrolyte Reviews*. Springer Science & Business Media, (1989)

36. E. Quartarone, P. Mustarelli & A. Magistris, 'PEO-based composite polymer electrolytes,' *Solid State Ionics* **110**, 1 (1998)

37. A.M. Stephan & K.S. Nahm, 'Review on composite polymer electrolytes for lithium batteries,' *Polymer* **47**, 5952 (2006)

CHAPTER 2

LITERATURE REVIEW

2.1 Solid Battery Electrolytes

Current studies on solid electrolytes can be divided into two general categories, organic and inorganic solid electrolytes. Organic solid electrolytes are cation-conducting polymers, which include dry solid and gel type polymer electrolytes. [1] Inorganic electrolytes include crystalline oxides and glassy materials.

Gel type electrolytes are in between solid and liquid electrolytes, which have solid skeletons and liquid electrolyte inside pores. Although they offer conductivity close to that of liquid electrolytes, poor mechanical stability and flammability are still problems.[2] Crystalline oxide materials including LIPON, NASICON, and LISICON structures are commonly studied, but the compatibility with lithium metal remains a problem. [3–11] In this chapter we will not review the gel type electrolytes and crystalline inorganics, but focus mainly on the literature review of amorphous inorganic materials and dry organic electrolytes, including dry polymer electrolytes and polymer composite electrolytes.

2.2 Ionic Conduction in Glass Materials

Solid glassy electrolytes have attracted attention for their possible use in providing a hard surface capable of suppressing side reactions and inhibiting dendritic growth of lithium that is responsible for cell short-circuiting. [12] Glassy materials may provide ionic conductivity higher than that of the corresponding crystals, as glasses retain some of the liquid-state structural features. The anisotropy and grain boundaries present in polycrystalline materials lead to resistive loss, decreasing cell efficiency, as well as chemical attack, raising safety concerns. [13, 14] The glassy solid electrolytes have other advantages over their polycrystalline counterparts, e.g. more "free volume" (Figure 2 - 1) due to open structure [15] and flexibility of size and shape at a satisfactory cost. [16] More importantly, glasses can be prepared over a wide range of compositions, allowing for better control of properties. [13, 17, 18] Glassy materials have an irregular network, which makes for variable-sized channels.

For Li^+ conducting glasses, as the radius of Li^+ is small, their mobility is higher than that of other ions because of their easy passage through these channels. This makes glass an ideal candidate for solid state electrolyte. Other than Li^+ conducting glasses, Na^+ conducting glasses are commonly studied because of the abundant and geographically uniform distribution of Na^+ recourses. Sodium solid state batteries have attracted much attention recently because of their potential applications in high temperature batteries and stationary large scale energy storage for renewable energies. Fabrication routes

for glassy solid electrolytes include conventional melt quenching techniques, rapid quenching, sol-gel synthesis, mechanical milling techniques, etc.

Ionic conducting glasses generally consist of a network former, a network modifier, and sometimes a doping salt. Network formers are covalent oxides or sulfides that make up the network such as SiO_2, P_2O_5, B_2O_3, SiS_2 etc. The oxygen or sulfur that link network former polyhedra together are known as bridging oxygen (BO), and bridging sulfur (BS). Network modifiers, like Na_2O or Li_2S, when added, break the covalent oxygen or sulfur bridges, createing non-bridging oxygens (NBO) or sulfurs (NBS) and each molecule of the modifier introduces mobile ions. Adding network modifiers decreases the average length of network linkage and makes the glass less rigid, usually decreasing the glass transition temperature. [19] Doping salts, such as LiI or Li_2SO_4 are added to increase the ionic conduction. These salts do not react chemically with the network formers but remain dissociated in solution. The associated anion must have a very low transference number, [19, 20] typically attributable to its size.

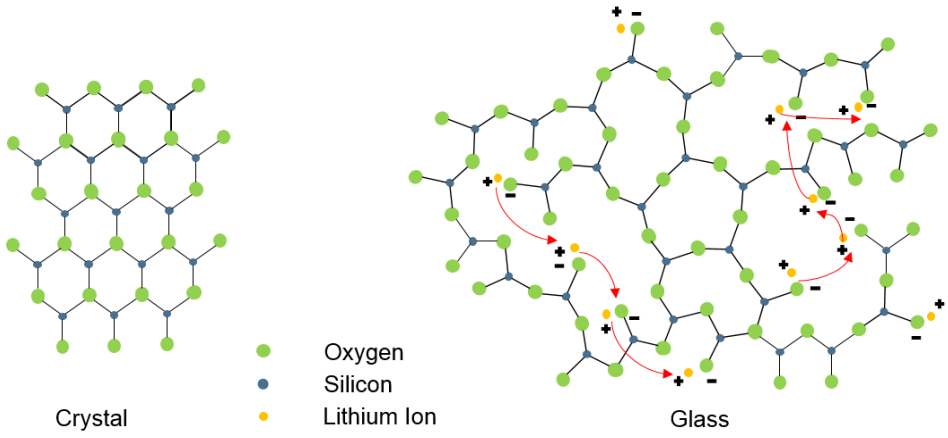

Figure 2 - 1 Glassy solids have "free volume" due to their open structure compared to the corresponding crystal. Ion hops from one site to the other.

There are two categories of ion conducting glasses, oxides and sulfides. Oxide glass electrolytes for solid-state batteries have been widely studied because they are stable in air and can be fabricated with relative ease. However, their ionic conductivities have not yet reached acceptable levels for practical use. Figure 2 - 2 shows that most of the lithium ion conducting oxide glasses have conductivities in the range of 10^{-7}-10^{-8} S·cm^{-1} at room temperature. Systems based on the Li^+ conducting B_2O_3-SiO_2 mixed glass formers have the highest room temperature conductivity of around ~10^{-5} S·cm^{-1}. [21–25] There are fewer studies on sodium ion conducting glasses due to their lower conductivities. Bhide and Hariharan reported that in $NaPO_3$ glass systems, the ionic conductivity can increase up to one order of magnitude for the maximum content of Na_2SO_4, reaching 9.4×10^{-6} S·cm^{-1} at 450K. [26] Some other studied glass systems include Na_2O–MoO_3–P_2O_5 [27], Na_2O-B_2O_3-P_2O_5 [28, 29], and Na_2O-B_2O_3-SiO_2 [30]

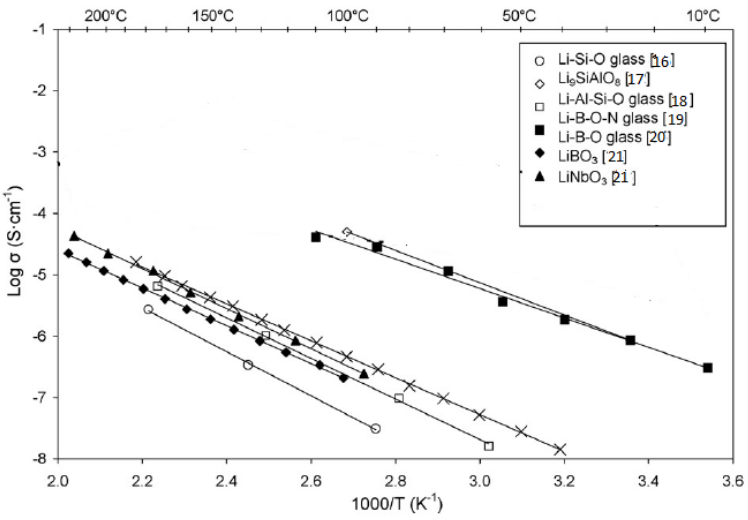

Figure 2 - 2 Ionic conductivity for oxide glasses [21]

Changing the oxygen atoms to sulfur generally increases the ionic conductivity. Sulfur has a larger ion size and a smaller electronegativity, which

bonds ions less tightly and widens the conduction pathways. For lithium conducting glasses, room temperature conductivity can reach as high as 10^{-3}-10^{-5} $S \cdot cm^{-1}$. [8, 21, 31] Commonly studied systems include Li_2S-P_2S_5 and Li_2S-SiO_2. [32, 33] However, sulfide glasses are very reactive in ambient conditions. The chemical instability in oxidizing atmospheres makes the synthesis and handling of the sulfide glasses significantly more difficult and costly. Sulfide glasses can also react with the lithium metal, hence work on sulfide glasses has been restricted.[19]

Several approaches have been pursued to enhance ionic conductivity in glass electrolytes. Deshpande et al [16] reported that increasing modifier content, adding salts and using mixed glass formers increases the ionic conductivity. The effect of adding modifier content in the glass has been commonly observed for lithium borate, lithium phosphate and lithium silicate glasses, in which the Li^+ conductivity increases with increasing Li_2O content.[16, 34] Figure 2 - 3 shows the relation between lithium content and the ionic conductivity for lithium borosilicate and lithium borophosphate glasses. For lithium borosilicate glasses, the conductivity increases monotonically with the Li_2O modifier content; conversely, for lithium borophosphate glasses, saturation occurs at 45 mol% of Li_2O. It is reported that the tendency for crystallization in the Li_2O–B_2O_3–P_2O_5 glass system rapidly increases at 45% Li_2O, and for even higher Li_2O content, it is almost impossible to suppress crystallization. [24, 35] Meanwhile, when the modifier content is too high, the density and the T_g decrease, indicating weakening of the glass structure.[16] Similarly, adding lithium salts like Li_2SO_4, LiI and LiCl is another approach that has led to increased conductivity in lithium borate and lithium

borosilicate glasses. Ions like I, Cl- and SO_4 which are relatively large, expand the lattice interstices and thereby enlarge the pathway for the ion conduction. Similar to adding network modifiers, too much of the lithium salt lowers T_g and weakening the glass structure [16, 36]. Figure 2 - 3(b) shows the decrease of glass transition temperature with increases in LiI salt content. [37]

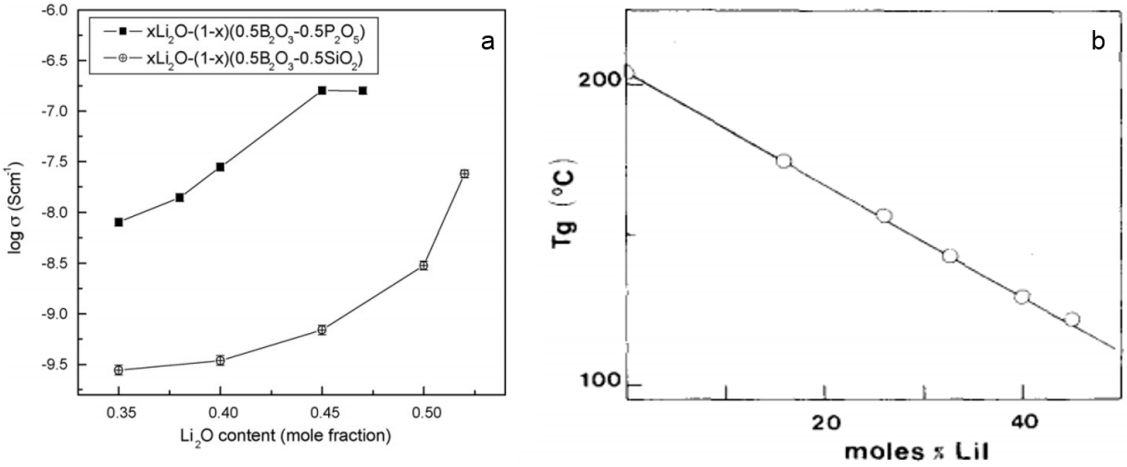

Figure 2 - 3 a) increased conductivity for higher amount of Li_2O modifier content. (b) Decreased glass transition temperature for higher Lithium salt content.[24]

Mixing two different network formers in alkali glasses is another approach to improve transport properties in glasses. Mixed network former glasses such as B_2O_3+Bi_2O_3+LiO_2 [38] and Li_2S+SiS_2+GeS_2 [39] exhibit two orders of magnitude enhancement in ionic conductivity. However, not all mixed network former glasses show increases in conductivity; instead, there exist both positive and negative mixed network former effects. $0.4R_2O + xB_2O_3 + (0.6\text{-}x)P_2O_5$ borophosphate glasses containing R_2O (R=Na or Li) [40] show two orders of magnitude increases in conductivity while $0.4Li_2O + 0.6[xB_2O_3 + (1\text{-}x)Si_2O_4]$ [41] and $27.5Li_2O + (72.5\text{-}x)B_2O_3 + xAl_2O_3$ [42] show lower conductivity compared to

either of the binary glasses. Although the effect of mixing network formers on the ionic conductivity is observed in many studies, the cause of the effect is not clear.

Magistris explains the enhancement using the weak electrolyte theory, which assumes that the mixed network formers hinder phase separation.[43] However, Pradel et al. explain their increase in ionic conductivity of $0.3Li_2S + 0.7[(1- x)SiS_2 + xGeS_2]$ differently. They argue that phase separation happens and that there is one phase containing all the lithium ions, which raises the conductivity. [44] Gedam and Deshpande followed the Anderson Stuart model [45] and reported that in the $27.5Li_2O + (72.5-x)B_2O_3 + xAl_2O_3$ system, it is the interionic bond distance change that modifies the network structure, which in turn changes the ion transport properties, i.e., larger ions expand the network and increase the conductivity. [42]

It is believed that the mechanism of ion conduction in glasses involves successive jumps of the lithium ion between energetically most stable positions in the vicinity of a charge-compensating network moiety. Accordingly, the ionic conductivity σ in the glasses depends on the concentration, charge, and mobility of mobile ions as

$$\text{Eq. 2-1} \qquad \sigma = nq\mu$$

where n is available carrier concentration, q is the charge and μ is the mobility. The latter is defined as the average jump frequency times the average distance between cation equilibrium sites, per applied electrostatic field strength. The d.c conductivity of glass electrolyte usually follows a classical “Arrhenius” behavior,

Eq. 2-2 $$\sigma(T) = \sigma_0 \exp\left(\frac{\Delta E_a}{RT}\right)$$

which describes a linear dependence of the logarithm of the conductivity vs. 1/T. Figure 2 - 4 shows an Arrhenius plot of some oxide glass electrolytes. Different models have been proposed for the ion transport mechanism, one example is the aforementioned Anderson-Stuart model. It describes ion hopping as a process in which the ion first overcomes a bonding energy and then passes through the pathway between adjacent interstices.

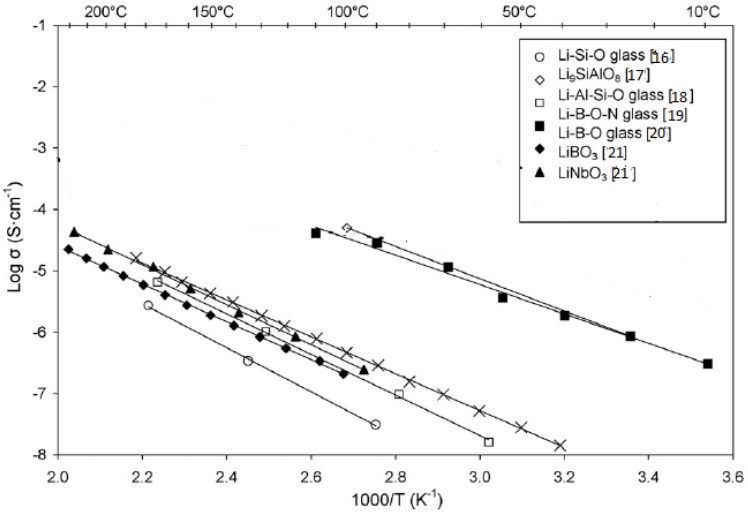

Figure 2 - 4 Ionic conductivity for oxide glasses [46]

2.3 Ionic Conduction in Polymer Electrolytes

Solvent-free dry polymer electrolytes are currently under intense scrutiny for use in high-energy density batteries. They have good processability and flexibility, and they can be easily made into various shapes including thin film membranes to have good contact with the electrodes.[10, 47] Despite the advantages of solid polymer electrolyte, the ionic conductivity is still relatively low at close to ambient operating temperatures. Also, the low elastic modulus still allows dendrite growth.

Several types of polymers, including PVDF ,PVDF-HFP, PMMA, PEO and PAN, have been investigated extensively. PVDF and PVDF-HFP are mostly studied for gel-type polymer electrolytes, in which liquid electrolytes are entrapped inside the polymer matrix. Since they do not belong to the category of dry solid electrolytes and still present a potential fire hazard, they are not the focus of this thesis. [48–50] PAN based electrolytes exhibit room temperature conductivities as high as 10^{-3} $S \cdot cm^{-1}$. Their electrochemical stability window is wide but they have high reactivity with lithium metal. [51, 52] PMMA offers acceptable ionic conductivities and stability in contact with lithium metal. Its poor mechanical strength, however, doesn't prevent dendrite growth from the metal anode. [53, 54] PVC based electrolytes possess greater stiffness; however, the highest reported ionic conductivity is still far below what is required for practical use and they are not compatible with lithium anodes. [55]

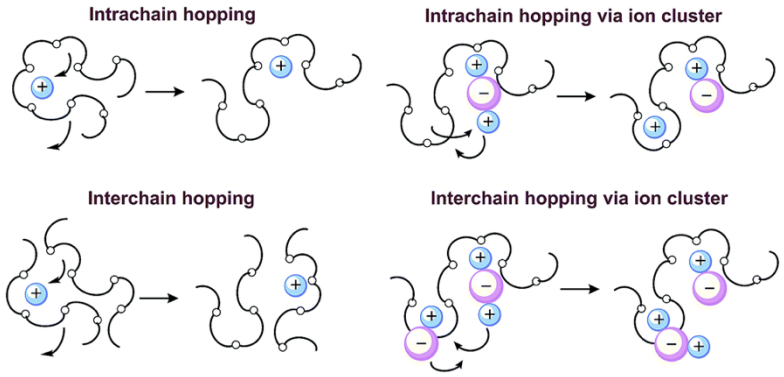

Figure 2 - 5 Segmental motion of the polymer chain and intrachain (top) and interchain (bottom) ion hopping

Among polymer electrolytes, poly(ethylene oxide) (PEO) is the most interesting base material for hosting lithium salts because it contains ether

coordination sites, which assist the dissociation of salts incorporated in the polymer, as well as a flexible macromolecular structure, which promotes facile ionic transport. [47, 56–59]

The ionic conduction of solid polymer electrolytes is facilitated by segmental motion of the polymer chains. [60, 61] In solid polymer electrolytes, lithium salts are solvated by the polymer chains. Proposed mechanisms for inter- and intra-molecular motion of the chains are illustrated in Figure 2 - 5. [62] The cation displacement along the polymer chain and between chains is accomplished by 180˚ rotations of C-O bonds, which results in the reorientation of chain segments so as to expose the cation to different neighboring sites. The highest ionic conductivity of solid polymer electrolytes occurs for ion transport in the amorphous region where the polymeric chains are more flexible, resulting in higher polymer segmental mobility. [56] As a result, the conductivity decreases when the degree of crystallinity increases.

Various salts are used in PEO based polymer electrolytes, including lithium trifluoromethanesulfonate ($LiCF_3SO_3$) (LiTF) lithium bis (trifluoromethanesulfonimidate) ($Li(CF_3SO_2)_2N$) (LiTFSI), lithium bis (trifluoromethanesulfonimide) ($Li(C_2F_5SO_2)_2N$) (LiBETI)], lithium perchlorate ($LiClO_4$) and lithium bis(oxalato)borate ($LiB(C_2O_4)_2$) (LiBOB). Figure 2 - 6 a and b show that the conductivity of electrolytes with different salts fall within a similar range, with the differences determined mainly by the lithium concentration in the polymer, i.e., the EO/Li ratio.[46] It is reported by several authors[63–70] that higher lithium concentration results in a lower degree of crystallinity in general because

more polymer chains are used to dissociate the lithium ion such that the freedom of polymer segments to reorient for crystallization is reduced.

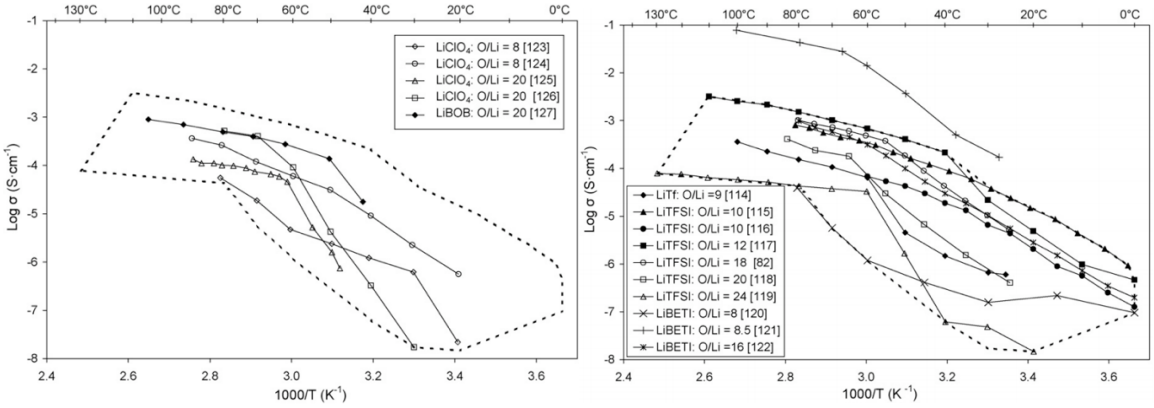

Figure 2 - 6 Conductivity of PEO with (a) $LiClO_4$ or LiBOB salts b) LiTF, LiTFSI or LIBETI salts.

To improve the ionic conductivity of PEO-based polymer electrolytes near room temperature, i.e., to stabilize amorphous regions, other units are incorporated into PEO by copolymerization, cross-linking, branching, and blending.[47, 71–74] These new structures exhibit a lower degree of crystallinity and lower glass transition temperature at ambient condition. As a consequence, the room temperature chain mobility and ionic conductivities are improved. [1]

Blending PEO with other non-crystalline polymers to reduce the degree of crystallinity is an easy and cost effective way of controlling physical properties such as mechanical strength and thermal stability without chemical interaction.[75–78] In order to achieve miscible polymer blends, intermolecular interaction with negative enthalpy to the free energy of mixing is advantageous.[79] Some examples of such polymers are polyacrylonitrile (PAN),[80] hyperbranched polymers (poly[bis(triethylene glycol)benzoate] with terminal acetyl groups),[81] poly(oligo[oxyethylene]oxysebacoyl) (PES),[82] and PEO-functionalized

polyoctahedral silsesquioxanes [83] Abraham and Alamgir[84] studied a polymer blend of [bis(methoxyethoxy-ethoxide)phosphazene] (MEEP) and PEO with $LiN(CF_3SO_2)_2$ doping, which showed a promising room temperature conductivity of 6.7×10^{-6} $S\cdot cm^{-1}$ for 55 wt. % MEEP/45 wt. % PEO and was anodically stable up to 4.5 V versus Li^+/Li. [84] When poly(bisphenol A-co-epi chlorohydrin) (PBE), and poly(vinyl ethylether) (PVEE) are blended with PEO, the crystallinity decreases, and an ionic conductivity of 10^{-3} $S\cdot cm^{-1}$ can be reached.[85] The mechanical stability of such a blend, however, is still not practical enough.

Crosslinking helps prevent crystallization and increase the mechanical stability.[86] Borghini et al. synthesized completely amorphous PEG 2000-crosslinked electrolytes with improved ionic conductivity and high mechanical strength.[87] Zhang et al. synthesized a cross-linked polysiloxane backbone network polymer with pendant oligo- (ethylene glycol) groups as internally plasticizing chains, resulting in room temperature conductivity up to 1.33×10^{-4} $S\cdot cm^{-1}$ for EO/Li of 20 and LiTFSI doping. This improvement was attributed to segmental motion of the pendant short PEO chains and the high flexibility of the siloxane backbone.[88]

Block copolymers of PEO provide structures with both sufficient mechanical stability and good ionic conductivity. The two properties can be simultaneously controlled by different blocks within the copolymer. [89–93] Examples of commonly studied block copolymer electrolytes include LiTFSI-doped polystyrene-block-poly(ethylene oxide),[94] poly(styrene-b-(styrene-g-ethylene oxide)-b -styrene) (PS-P(S-g-EO)-PS),[95] and poly(isoprene-b-styrene-b-ethylene oxide)[90] triblock

copolymers. These copolymers exhibit elastic moduli as high as ~1GPa between 0 and 100ºC, much higher than that of PEO homopolymers.[95] Although the shear moduli of electrolyte materials needs to be at least 7 GPa to suppress dendrite growth on the anode according to Monroe and Newman [96], the fact that conductivity and elastic moduli are decoupled enables further increases in the moduli without sacrificing mobility.[93]

2.4 Composite Electrolytes

Polymer composite materials with ceramic fillers have attracted much attention recently because the large interfacial regions created in such materials may have properties that cannot be achieved with pure constituents.[97, 98] Numerous studies have been published on such composite materials, with solid electrolytes in lithium ion batteries as one application. Typically, a composite electrolyte consists of an ion-conducting host polymer matrix and micro- or nano-sized ceramic particles.

As shown in Figure 2 - 7, in polymer-ceramic composite materials, the ceramic particles and polymer can form a variety of configurations composed of strong ionic bonds and weak hydrogen bonds. In polymer-ceramic composites, control over particle dispersion is of great importance to achieve predictable properties and performance because the interparticle forces typically favor particle agglomeration, which reduces the interfacial area. [62] The dispersion of particles is dependent on several factors, such as surface chemistry, synthesis method of the particle, dispersion method, and the interactions between the host

polymer matrix and the particles. To achieve good dispersion, it is necessary to carefully control these factors so that the polymer-particle interaction is favored over particle-particle interactions. [99–101] Specially treated particles with tethered ligands have been studied to avoid particle-particle agglomeration and achieve better dispersion. [102] One example is the use of oligomeric PEG ligands on nanoparticles such as SiO_2 [103] or SnO.[104] The optimum chain lengths of the tethering ligand ,for which crystallization is suppressed while segmental mobility is still good have been studied. With complete dispersion, crystallinity is inhibited, and room temperature conductivity is enhanced.[103, 104] However, generally, the dispersion of small particles into the host polymer remains a challenge and a fundamental topic in the field of polymer nanocomposites.

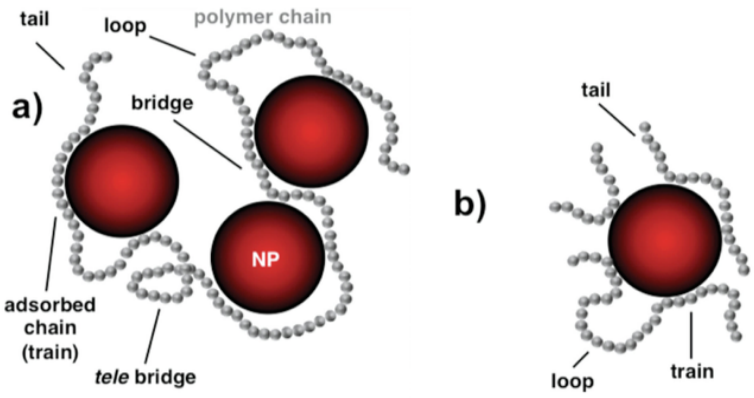

Figure 2 - 7 Configurations of ceramic particles in polymer-ceramic composite.

Early in 1982, Weston and Steele reported improved mechanical stability when 10 vol% inert α-alumina ceramic fillers (Analar grade, ~300mesh) were introduced into PEO. The composite electrolytes showed no evidence of creep and limited deformation up to a temperature of 120°C over 166 hours, in contrast to 51% creep within 42 hours for electrolytes without ceramic particles.

Furthermore, the addition of ceramic fillers had negligible effect on the conductivity.[105] Much research has been done since then, focusing more on improving transport properties by introducing ceramic particles. Various nano-composite systems and fabrication methods have been reported.[106–109] TiO_2,[110–113] Al_2O_3,[114, 115] ZnO,[116] ZrO_2,[117] and SiO_2 are commonly studied fillers.[118, 119] Such nanocomposite electrolytes provide high ionic conductivities, good electrical insulation, and good mechanical, chemical and thermal stability.[116, 120–122] They also show improved interfacial properties in contact with the lithium electrode.[123]

Most of these studies attribute the enhancement in ionic conductivity to the inhibition of crystallization in the polymer phases. When small particles are dispersed in a polymer, they act as solid plasticizers, occupying free volume, increasing the intermolecular distance, reducing secondary bonding, and creating obstacles that inhibit crystallization.[72, 120] Many authors reported a lower degree of crystallinity and glass transition temperature with particle loading up to 10-15 wt. %. This coincided with an increase in ionic conductivity, suggesting a correlation between conductivity and crystallinity.[72, 105, 124] Although the optimum loading of particles is influenced by the dispersion state and particle properties, various studies reported the optimum loading to be between 10 and 15 wt. %.This results in up to 3 orders of magnitude enhancement in room temperature ionic conductivity compared to ceramic-free electrolytes, whose conductivities are on the order of 10^{-8} $S \cdot cm^{-1}$ at room temperature. [118, 121, 125]

Besides the decrease in degree of crystallinity, some authors report that the ion transport in composite electrolytes appears to take place along the surface of the nanoparticles or through the interfacial (or interphase) region.[110, 126–129] Lithium ions are therefore able to move both via the segmental motion of polymer chains as well as by activated hops along the surface of the fillers, where vacant void space are large enough to accommodate the ions. The ceramic fillers can also improve the mechanical integrity, which is of great importance since higher ionic conductivity and poor mechanical stiffness are often times found to be coupled.[130]

So far, most of the ceramic fillers studied are passive, i.e., they do not contribute to the ionic conductivity of the nanocomposite electrolyte by providing migration pathways within their bulk or by acting as a source of charge carriers. Active fillers either share the lithium species with the polymer matrix, or directly affect the ion transport in some way. Several types of active fillers have recently been studied, such as $Li_{1.4}Al_{0.4}Ge_{1.7}(PO_4)_3$, $Li_{0.33}La_{0.557}TiO_3$ (LLTO) and $Li_{1.3}Al_{0.3}Ti_{1.7}(PO_4)_3$ (LATP), which drastically increase ionic conductivities in these composite electrolytes up to the order of 10^{-4} $S \cdot cm^{-1}$ in various polymeric systems.[131–133] According to Liu et al., pathways for fast ion transport on the surface of the ceramic nano-filler establish a conductive network in the polymer matrix.

Another category of composite material distinct from most of the PEO-ceramic composites consists of so-called hybrid materials. The difference between the two is that instead of physically blending inorganic particles into

organic matrix with weak secondary bonds, in hybrid materials typically covalent bonds connect the organic and inorganic phases.[134] As a consequence, the resulting materials can have properties that are better than their components. For electrolyte applications, the materials show higher chain mobility in the organic phase as well as the thermal stability from the inorganic phase. [91, 102, 104, 134–145]

In terms of microstructures, hybrid materials can be analogous to polymer-particle composites, with chemical bonding between the surface groups of particles and polymer matrix,[135, 136, 138, 139] but they also can differ significantly. For example, the inorganic phase can form a network in addition to the polymer matrix,[91, 140, 141, 144] which provides better mechanical and electrochemical stability. Among such hybrids, silica-based materials with polyether polymer chains hold a prominent place. Silica-polymer hybrid materials combine the solvating power of the ether units with the presence of an amorphous silica network, which provides good mechanical resistance, thermal stability and natural amorphous character simultaneously.[146] The sol-gel method is usually used to make such hybrid materials due to its low reaction temperature and mild reaction conditions, which allow fine control over each component. Details of this synthesis method can be found in the next charter.

2.5 References

1. F.B. Dias, L. Plomp & J.B.J. Veldhuis, 'Trends in polymer electrolytes for secondary lithium batteries,' *Journal of Power Sources* **88**, 169 (2000)

2. S. Chintapalli & R. Frech, 'Effect of plasticizers on high molecular weight PEO-$LiCF_3SO_3$ complexes,' *Solid State Ionics* **86**, 341 (1996)

3. P.G. Bruce & A.R. West, 'The a c conductivity of polycrystalline LISICON, $Li_{2+2x}Zn_{1-x}GeO_4$, and a model for intergranular constriction resistances,' *Journal of The Electrochemical Society* **130**, 662 (1983)

4. N.J. Dudney, 'Addition of a thin-film inorganic solid electrolyte (LIPON) as a protective film in lithium batteries with a liquid electrolyte,' *Journal of Power Sources* **89**, 176 (2000)

5. Y. Hamon, A. Douard, F. Sabary, C. Marcel, P. Vinatier, B. Pecquenard & A. Levasseur, 'Influence of sputtering conditions on ionic conductivity of LIPON thin films,' *Solid State Ionics* **177**, 257 (2006)

6. S. Hasegawa, N. Imanishi, T. Zhang, J. Xie, A. Hirano, Y. Takeda & O. Yamamoto, 'Study on lithium/air secondary batteries—stability of NASICON-type lithium ion conducting glass–ceramics with water,' *Journal of Power Sources* **189**, 371 (2009)

7. R. Kanno & M. Murayama, 'Lithium ionic conductor thio-LISICON: The Li_2S-GeS_2-P_2S_5 system,' *Journal of The Electrochemical Society* **148**, A742 (2001)

8. M. Murayama, N. Sonoyama, A. Yamada & R. Kanno, 'Material design of new lithium ionic conductor, thio-LISICON, in the Li_2S–P_2S_5 system,' *Solid State Ionics* **170**, 173 (2004)

9. K.S. Nanjundaswamy, A.K. Padhi, J.B. Goodenough, S. Okada, H. Ohtsuka, H. Arai & J. Yamaki, 'Synthesis, redox potential evaluation and electrochemical characteristics of NASICON-related-3d framework compounds,' *Solid State Ionics* **92**, 1 (1996)

10. P. Vashishta, J.N. Mundy & G. Shenoy, 'Fast ion transport in solids: Electrodes and electrolytes,' (1979)

11. W.C. West, J.F. Whitacre & J.R. Lim, 'Chemical stability enhancement of lithium conducting solid electrolyte plates using sputtered LIPON thin films,' *Journal Of Power Sources* **126**, 134 (2004)

12. van Schalkwijk W. & B. Scrosati. 2002. Advances in lithium ion batteries introduction(ed.) *Advances in Lithium-Ion Batteries*: 1-5. Springer.

13. T. Minami, 'Recent progress in superionic conducting glasses,' *Journal of Non-Crystalline Solids* **95**, 107 (1987)

14. T. Minami, Y. Takuma & M. Tanaka, 'Superionic conducting glasses: Glass formation and conductivity in the AgI-Ag_2O-P_2O_5 system,' *Journal of The Electrochemical Society* **124**, 1659 (1977)

15. M. Tatsumisago, 'Glassy materials based on Li_2S for all-solid-state lithium secondary batteries,' *Solid State Ionics* **175**, 13 (2004)

16. V.K. Deshpande, 'Science and technology of glassy solid electrolytes,' IOP Conference Series: Materials Science and Engineering **2**, 012011 (2009)

17. D. Ravaine, 'Glasses as solid electrolytes,' *Journal of Non-Crystalline Solids* **38**, 353 (1980)

18. D. Ravaine, 'Ionic transport properties in glasses,' *Journal of Non-Crystalline Solids* **73**, 287 (1985)

19. M. Duclot & J.-L. Souquet, 'Glassy materials for lithium batteries: Electrochemical properties and devices performances,' *Journal of Power Sources* **97**, 610 (2001)

20. E. Robinel, A. Kone, M.J. Duclot & J.L. Souquet, 'Silver sulfide based glasses:(ii). Electrochemical properties of GeS_2-Ag_2S-AgI glasses: Transference number measurement and redox stability range,' *Journal Of Non-Crystalline Solids* **57**, 59 (1983)

21. I. Seo & S.W. Martin, *New developments in solid electrolytes for thin-film lithium batteries*. INTECH Open Access Publisher, (2012)

22. M. Tatsumisago, K. Yoneda, N. Machida & T. Hinami, 'Ionic conductivity of rapidly quenched glasses with high concentration of lithium ions,' *Journal of Non-Crystalline Solids* **95**, 857 (1987)

23. P. Heitjans, E. Tobschall & M. Wilkening, 'Ion transport and diffusion in nanocrystalline and glassy ceramics,' *The European Physical Journal Special Topics* **161**, 97 (2008)

24. C.-H. Lee, K.H. Joo, J.H. Kim, S.G. Woo, H.-J. Sohn, T. Kang, Y. Park & J.Y. Oh, 'Characterizations of a new lithium ion conducting Li_2O–SeO_2–B_2O_3 glass electrolyte,' *Solid State Ionics* **149**, 59 (2002)

25. M. Nogami & Y. Moriya, 'Glass formation of the s SiO_2-B_2O_3 system by the gel process from metal alkoxides,' *Journal of Non-Crystalline Solids* **48**, 359 (1982)

26. A. Bhide & K. Hariharan, 'Sodium ion transport in $NaPO_3$–Na_2SO_4 glasses,' *Materials Chemistry and Physics* **105**, 213 (2007)

27. L. Bih, M. El Omari, J.M. Reau, A. Nadiri, A. Yacoubi & M. Haddad, 'Electrical properties of glasses in the Na_2O–MoO_3–P_2O_5 system,' *Materials Letters* **50**, 308 (2001)

28. R. Christensen, G. Olson & S.W. Martin, 'Ionic conductivity of mixed glass former 0.35 Na_2O+ 0.65 [x B_2O_3+(1–x) P_2O_5] glasses,' *The Journal of Physical Chemistry B* **117**, 16577 (2013)

29. P.S. Anantha & K. Hariharan, 'Structure and ionic transport studies of sodium borophosphate glassy system,' *Materials Chemistry And Physics* **89**, 428 (2005)

30. A. Grandjean, M. Malki, V. Montouillout, F. Debruycker & D. Massiot, 'Electrical conductivity and 11B NMR studies of sodium borosilicate glasses,' *Journal of Non-Crystalline Solids* **354**, 1664 (2008)

31. M. Tatsumisago, S. Hama, A. Hayashi, H. Morimoto & T. Minami, 'New lithium ion conducting glass-ceramics prepared from mechanochemical Li_2S-P_2S_5 glasses,' *Solid State Ionics* **154**, 635 (2002)

32. N. Machida & T. Shigematsu, 'An all-solid-state lithium battery with sulfur as positive electrode materials,' *Chemistry Letters* **33**, 376 (2004)

33. T. Ohtomo, A. Hayashi, M. Tatsumisago, Y. Tsuchida, S. Hama & K. Kawamoto, 'All-solid-state lithium secondary batteries using the $75Li_2S$ -$25P_2S_5$ glass and the $70Li_2S$ -$30P_2S_5$ glass–ceramic as solid electrolytes,' *Journal of Power Sources* **233**, 231 (2013)

34. A. Levasseur, M. Kbala, P. Hagenmuller, G. Couturier & Y. Danto, 'Elaboration and characterization of lithium conducting thin film glasses,' *Solid State Ionics* **9**, 1439 (1983)

35. S.H. Lee, K.I. Cho, J.B. Choi & D.W. Shin, 'Phase separation and electrical conductivity of lithium borosilicate glasses for potential thin film solid electrolytes,' *Journal of Power Sources* (2006)

36. P.R. Gandhi, V.K. Deshpande & K. Singh, 'Conductivity enhancement in Li_2SO_4 incorporated Li_2O-B_2O_3 glass system,' *Solid State Ionics* (1989)

37. B.A. Boukamp & R.A. Huggins, 'Fast ionic conductivity in lithium nitride,' *Materials Research Bulletin* **13**, 23 (1978)

38. A. Agarwal, V.P. Seth, P.S. Gahlot, S. Khasa, M. Arora & S.K. Gupta, 'Study of electron paramagnetic resonance, optical transmission and dc conductivity of vanadyl doped Bi_2O_3· B_2O_3· Li_2O glasses,' *Journal Of Alloys And Compounds* **377**, 225 (2004)

39. A. Pradel, N. Kuwata & M. Ribes, 'Ion transport and structure in chalcogenide glasses,' *Journal of Physics: Condensed Matter* **15**, S1561 (2003)

40. T. Tsuchiya & T. Moriya, 'Anomalous behavior of physical and electrical properties in borophosphate glasses containing R_2O and V_2O_5,' *Journal of Non-Crystalline Solids* **38**, 323 (1980)

41. L.F. Maia & A.C.M. Rodrigues, 'Electrical conductivity and relaxation frequency of lithium borosilicate glasses,' *Solid State Ionics* **168**, 87 (2004)

42. R.S. Gedam & V.K. Deshpande, 'An anomalous enhancement in the electrical conductivity of Li_2O : B_2O_3 : Al_2O_3 glasses,' *Solid State Ionics* **177**, 2589 (2006)

43. A. Magistris, G. Chiodelli & M. Duclot, 'Silver borophosphate glasses: Ion transport, thermal stability and electrochemical behavior,' *Solid State Ionics* **9**, 611 (1983)

44. A. Pradel, C. Rau, D. Bittencourt, P. Armand, E. Philippot & M. Ribes, 'Mixed glass former effect in the system 0.3 Li_2S - 0.7 [(1- x)SiO_2 - xGeO_2]: A structural explanation,' *Chemistry of Materials* **10**, 2162 (1998)

45. O.L. Anderson & D.A. Stuart, 'Calculation of activation energy of ionic conductivity in silica glasses by classical methods,' *Journal of the American Ceramic Society* **37**, 573 (1954)

46. J.W. Fergus, 'Ceramic and polymeric solid electrolytes for lithium-ion batteries,' *Journal of Power Sources* **195**, 4554 (2010)

47. Gray F.M. 1991. *Solid polymer electrolytes*. VCH New Tork etc.

48. C. Capiglia, Y. Saito, H. Kataoka, T. Kodama, E. Quartarone & P. Mustarelli, 'Structure and transport properties of polymer gel electrolytes based on PVDF-HFP and LiN $(C_2F_5SO_2)_2$,' *Solid State Ionics* **131**, 291 (2000)

49. H.S. Choe, J. Giaccai, M. Alamgir & K.M. Abraham, 'Preparation and characterization of poly (vinyl sulfone)-and poly (vinylidene fluoride)-based electrolytes,' *Electrochimica Acta* **40**, 2289 (1995)

50. D. Saikia & A. Kumar, 'Ionic conduction in P (VDF-HFP)/PVDF–(PC+ DEC)–$LiClO_4$ polymer gel electrolytes,' *Electrochimica Acta* **49**, 2581 (2004)

51. H. Hong, C. Liquan, H. Xuejie & X. Rongjian, 'Studies on PAN-based lithium salt complex,' *Electrochimica Acta* **37**, 1671 (1992)

52. Z. Wang, B. Huang, H. Huang, L. Chen, R. Xue & F. Wang, 'Infrared spectroscopic study of the interaction between lithium salt $LiClO_4$ and the plasticizer ethylene carbonate in the polyacrylonitrile-based electrolyte,' *Solid State Ionics* **85**, 143 (1996)

53. G.B. Appetecchi, F. Croce & B. Scrosati, 'Kinetics and stability of the lithium electrode in poly (methylmethacrylate)-based gel electrolytes,' *Electrochimica Acta* **40**, 991 (1995)

54. G. Feuillade & P. Perche, 'Ion-conductive macromolecular gels and membranes for solid lithium cells,' *Journal of Applied Electrochemistry* **5**, 63 (1975)

55. A.M. Sukeshini, A. Nishimoto & M. Watanabe, 'Transport and electrochemical characterization of plasticized poly (vinyl chloride) solid electrolytes,' *Solid State Ionics* **86**, 385 (1996)

56. S. Ibrahim & M.R. Johan, 'Thermolysis and conductivity studies of poly (ethylene oxide)(PEO) based polymer electrolytes doped with carbon nanotube,' *International Journal of Electrochemical Science* **7**, 2596 (2012)

57. M.B. Armand, M.J. Duclot & P. Rigaud, 'Polymer solid electrolytes: Stability domain,' *Solid State Ionics* **3**, 429 (1981)

58. J.R. MacCallum & C.A. Vincent, *Polymer Electrolyte Reviews*. Springer Science & Business Media, (1989)

59. B. Scrosati & R.J. Neat. 'Lithium polymer batteries(ed.)' *Applications of Electroactive Polymers*: 182-222. SpringeR, (1993)

60. D.E. Fenton, J.M. Parker & P.V. Wright, 'Complexes of alkali metal ions with poly (ethylene oxide),' *Polymer* **14**, 589 (1973)

61. P.V. Wright, 'Electrical conductivity in ionic complexes of poly (ethylene oxide),' *Polymer International* **7**, 319 (1975)

62. S. Srivastava, J.L. Schaefer, Z. Yang, Z. Tu & L.A. Archer, '25th anniversary article: Polymer–particle composites: Phase stability and applications in electrochemical energy storage,' *Advanced Materials* **26**, 201 (2014)

63. N. Angulakshmi, T.P. Kumar, S. Thomas & A.M. Stephan, 'Ionic conductivity and interfacial properties of nanochitin-incorporated polyethylene oxide–LiN $(C_2F_5SO_2)_2$ polymer electrolytes,' *Electrochimica Acta* **55**, 1401 (2010)

64. G. Derrien, J. Hassoun, S. Sacchetti & S. Panero, 'Nanocomposite peo-based polymer electrolyte using a highly porous, super acid zirconia filler,' *Solid State Ionics* **180**, 1267 (2009)

65. L.-Z. Fan, X.-L. Wang, F. Long & X. Wang, 'Enhanced ionic conductivities in composite polymer electrolytes by using succinonitrile as a plasticizer,' *Solid State Ionics* **179**, 1772 (2008)

66. J. Kumar, S.J. Rodrigues & B. Kumar, 'Interface-mediated electrochemical effects in lithium/polymer-ceramic cells,' *Journal of Power Sources* **195**, 327 (2010)

67. H.M.J.C. Pitawala, M.A.K.L. Dissanayake, V.A. Seneviratne, B.-E. Mellander & I. Albinson, 'Effect of plasticizers (EC or PC) on the ionic conductivity and thermal properties of the $(PEO)_9$ LiTF: Al_2O_3 nanocomposite polymer electrolyte system,' *Journal of Solid State Electrochemistry* **12**, 783 (2008)

68. C. Shen, J. Wang, Z. Tang, H. Wang, H. Lian, J. Zhang & C.-N. Cao, 'Physicochemical properties of poly (ethylene oxide)-based composite polymer electrolytes with a silane-modified mesoporous silica SBA-15,' *Electrochimica Acta* **54**, 3490 (2009)

69. H.H. Sumathipala, J. Hassoun, S. Panero & B. Scrosati, 'High performance PEO-based polymer electrolytes and their application in rechargeable lithium polymer batteries,' *Ionics* **13**, 281 (2007)

70. C. Zhu, H. Cheng & Y. Yang, 'Electrochemical characterization of two types of PEO-based polymer electrolytes with room-temperature ionic liquids,' *Journal of the Electrochemical Society* **155**, A569 (2008)

71. M. Matsumoto, T. Uno, M. Kubo & T. Itoh, 'Electrochemical and thermal properties of polymer electrolytes based on the random and triblock copolymers of poly (ethylene oxide) with poly (propylene oxide),' *Journal of Materials Science and Engineering A: Structural Materials: Properties, Microstructure and Processing* **1**, 607 (2011)

72. F. Croce, G.B. Appetecchi, L. Persi & B. Scrosati, 'Nanocomposite polymer electrolytes for lithium batteries,' *Nature* **394**, 456 (1998)

73. J. Lipkowski & P.N. Ross *The electrochemistry of novel materials*. VCH Publishers, (1994)

74. A. Nishimoto, M. Watanabe, Y. Ikeda & S. Kohjiya, 'High ionic conductivity of new polymer electrolytes based on high molecular weight polyether comb polymers,' *Electrochimica Acta* **43**, 1177 (1998)

75. L. Cohen & A. Rocco, 'Study of the crystallization kinetics. Poly (ethylene oxide) and a blend of poly (ethylene oxide) and poly (bisphenol a-co-epichlorohydrin),' *Journal of Thermal Analysis and Calorimetry* **59**, 625 (2000)

76. C.R. Herrero & J.L. Acosta, 'Effect of poly (epichlorhydrin) on the crystallization and compatibility behavior of poly (ethylene oxide)/polyphosphazene blends,' *Polymer Journal* **26**, 786 (1994)

77. A.M. Rocco, R.P. Pereira & M.I. Felisberti, 'Miscibility, crystallinity and morphological behavior of binary blends of poly (ethylene oxide) and poly (methyl vinyl ether–maleic acid),' *Polymer* **42**, 5199 (2001)

78. A.M. Rocco, C.P. Da Fonseca & R.P. Pereira, 'A polymeric solid electrolyte based on a binary blend of poly (ethylene oxide), poly (methyl vinyl ether-maleic acid) and $LiClO_4$,' *Polymer* **43**, 3601 (2002)

79. J.M.G. Cowie & C. Love, 'The use of molecular recognition to obtain selective blending in polymer systems,' *Polymer* **42**, 4783 (2001)

80. B.K. Choi, Y.W. Kim & H.K. Shin, 'Ionic conduction in PEO–PAN blend polymer electrolytes,' *Electrochimica Acta* **45**, 1371 (2000)

81. Z. Wen, T. Itoh, Y. Ichikawa, M. Kubo & O. Yamamoto, 'Blend-based polymer electrolytes of poly (ethylene oxide) and hyperbranched poly [bis (triethylene glycol) benzoate] with terminal acetyl groups,' *Solid State Ionics* **134**, 281 (2000)

82. D.-W. Kim, J.-K. Park & H.-W. Rhee, 'Conductivity and thermal studies of solid polymer electrolytes prepared by blending poly (ethylene oxide), poly (oligo [oxyethylene] oxysebacoyl) and lithium perchlorate,' *Solid State Ionics* **83**, 49 (1996)

83. H. Zhang, S. Kulkarni & S.L. Wunder, 'Blends of poss- PEO (n= 4) 8 and high molecular weight poly (ethylene oxide) as solid polymer electrolytes for lithium batteries,' *The Journal of Physical Chemistry B* **111**, 3583 (2007)

84. K.M. Abraham & M. Alamgir, 'Dimensionally stable MEEP-based polymer electrolytes and solid-state lithium batteries,' *Chemistry of Materials* **3**, 339 (1991)

85. A.M. Rocco, A. De Assis Carias & R.P. Pereira, 'Polymer electrolytes based on a ternary miscible blend of poly (ethylene oxide), poly (bisphenol a-co-epichlorohydrin) and poly (vinyl ethyl ether),' *Polymer* **51**, 5151 (2010)

86. J.F. Le Nest, S. Callens, A. Gandini & M. Armand, 'A new polymer network for ionic conduction,' *Electrochimica Acta* **37**, 1585 (1992)

87. M.C. Borghini, M. Mastragostino & A. Zanelli, 'Reliability of lithium batteries with crosslinked polymer electrolytes,' *Electrochimica Acta* **41**, 2369 (1996)

88. Z. Zhang, D. Sherlock, R. West, R. West, K. Amine & L.J. Lyons, 'Cross-linked network polymer electrolytes based on a polysiloxane backbone with oligo (oxyethylene) side chains: Synthesis and conductivity,' *Macromolecules* **36**, 9176 (2003)

89. H.R. Allcock, R. Prange & T.J. Hartle, 'Poly (phosphazene- ethylene oxide) di-and triblock copolymers as solid polymer electrolytes,' *Macromolecules* **34**, 5463 (2001)

90. T.H. Epps, T.S. Bailey, R. Waletzko & F.S. Bates, 'Phase behavior and block sequence effects in lithium perchlorate-doped poly (isoprene-b-styrene-b-ethylene oxide) and poly (styrene-b-isoprene-b-ethylene oxide) triblock copolymers,' *Macromolecules* **36**, 2873 (2003)

91. H.M. Kao & C.L. Chen, 'An organic–inorganic hybrid electrolyte derived from self assembly of a poly (ethylene oxide)–poly (propylene oxide)–poly (ethylene oxide) triblock copolymer,' *Angewandte Chemie International Edition* **43**, 980 (2004)

92. P.P. Soo, B. Huang, Y.I. Jang, Y.M. Chiang, D.R. Sadoway & A.M. Mayes, 'Rubbery block copolymer electrolytes for solid state rechargeable lithium batteries,' *Journal of the Electrochemical Society* **146**, 32 (1999)

93. W.S. Young, W.F. Kuan & T.H. Epps, 'Block copolymer electrolytes for rechargeable lithium batteries,' *Journal of Polymer Science Part B: Polymer Physics* **52**, 1 (2014)

94. A. Panday, S. Mullin, E.D. Gomez, N. Wanakule, V.L. Chen, A. Hexemer, J. Pople & N.P. Balsara, 'Effect of molecular weight and salt concentration on conductivity of block copolymer electrolytes,' *Macromolecules* **42**, 4632 (2009)

95. C. Wang, T. Sakai, O. Watanabe, K. Hirahara & T. Nakanishi, 'All solid-state lithium-polymer battery using a self-cross-linking polymer electrolyte,' *Journal Of The Electrochemical Society* **150**, A1166 (2003)

96. C. Monroe & J. Newman, 'The impact of elastic deformation on deposition kinetics at lithium/polymer interfaces,' *Journal of The Electrochemical Society* **152**, A396 (2005)

97. E.P. Giannelis, 'Polymer layered silicate nanocomposites,' *Advanced materials* **8**, 29 (1996)

98. S.S. Ray & M. Okamoto, 'Polymer/layered silicate nanocomposites: A review from preparation to processing,' *Progress In Polymer Science* **28**, 1539 (2003)

99. B.J. Anderson & C.F. Zukoski, 'Rheology and microstructure of entangled polymer nanocomposite melts,' *Macromolecules* **42**, 8370 (2009)

100. N. Jouault, P. Vallat, F. Dalmas, S. Said, J. Jestin & F. Boué, 'Well-dispersed fractal aggregates as filler in polymer- silica nanocomposites: Long-range effects in rheology,' *Macromolecules* **42**, 2031 (2009)

101. Q. Zhang & L.A. Archer, 'Poly (ethylene oxide)/silica nanocomposites: Structure and rheology,' *Langmuir* **18**, 10435 (2002)

102. J. Guo, Z. Yang, Y. Yu, H.C.D. Abrun A & L.A. Archer, 'Lithium– sulfur battery cathode enabled by lithium–nitrile interaction,' *Journal of the American Chemical Society* **135**, 763 (2012)

103. J.L. Nugent, S.S. Moganty & L.A. Archer, 'Nanoscale organic hybrid electrolytes,' *Advanced Materials* **22**, 3677 (2010)

104. H.-M. Xiong, D.-P. Liu, H. Zhang & J.-S. Chen, 'Polyether-grafted SnO_2 nanoparticles designed for solid polymer electrolytes with long-term stability,' *Journal of Materials Chemistry* **14**, 2775 (2004)

105. J.E. Weston & B.C.H. Steele, 'Effects of inert fillers on the mechanical and electrochemical properties of lithium salt-poly (ethylene oxide) polymer electrolytes,' *Solid State Ionics* **7**, 75 (1982)

106. D.R. Macfarlane, P.J. Newman, K.M. Nairn & M. Forsyth, 'Lithium-ion conducting ceramic/polyether composites,' *Electrochimica Acta* **43**, 1333 (1998)

107. M. Morita, T. Fujisaki, N. Yoshimoto & M. Ishikawa, 'Ionic conductance behavior of polymeric composite solid electrolytes containing lithium aluminate,' *Electrochimica Acta* **46**, 1565 (2001)

108. H.Y. Sun, Y. Takeda, N. Imanishi, O. Yamamoto & H.J. Sohn, 'Ferroelectric materials as a ceramic filler in solid composite polyethylene oxide based electrolytes,' *Journal of the Electrochemical Society* **147**, 2462 (2000)

109. Z. Wen, T. Itoh, T. Uno, M. Kubo, T. Wen & O. Yamamoto, 'Polymer electrolytes based on poly (ethyleye oxide) and cross-linked poly (ethylene oxide-co-propylene oxide),' *Solid State Ionics* **175**, 739 (2004)

110. J. Adebahr, A.S. Best, N. Byrne, P. Jacobsson, D.R. Macfarlane & M. Forsyth, 'Ion transport in polymer electrolytes containing nanoparticulate TiO_2: The influence of polymer morphology,' *Physical Chemistry Chemical Physics* **5**, 720 (2003)

111. H.W. Han, W. Liu, J. Zhang & X. Zhao, 'A hybrid poly (ethylene oxide)/poly (vinylidene fluoride)/TiO_2 nanoparticle solid-state redox electrolyte for dye-sensitized nanocrystalline solar cells,' *Advanced Functional Materials* **15**, 1940 (2005)

112. P. Johansson & P. Jacobsson, 'TiO_2 nano-particles in polymer electrolytes: Surface interactions,' *Solid State Ionics* (2004)

113. B. Kumar, L.G. Scanlon & R.J. Spry, 'On the origin of conductivity enhancement in polymer-ceramic composite electrolytes,' *Journal of Power Sources* **96**, 337 (2001)

114. S.A. Suthanthiraraj & D.J. Sheeba, 'Structural investigation on PEO-based polymer electrolytes dispersed with Al_2O_3 nanoparticles,' *Ionics* (2007)

115. W. Wieczorek, J.R. Stevens & Z. Florjańczyk, 'Composite polyether based solid electrolytes. The Lewis acid-base approach,' *Solid State Ionics* **85**, 67 (1996)

116. H.-M. Xiong, X. Zhao & J.-S. Chen, 'New polymer-inorganic nanocomposites: PEO-ZnO and PEO-ZnO-$LiClO_4$ films,' *The Journal of Physical Chemistry B* **105**, 10169 (2001)

117. B. Kumar & L.G. Scanlon, 'Polymer–ceramic composite electrolytes: Conductivity and thermal history effects,' *Solid State Ionics* **124**, 239 (1999)

118. H.J. Walls, J. Zhou, J.A. Yerian, P.S. Fedkiw, S.A. Khan, M.K. Stowe & G.L. Baker, 'Fumed silica-based composite polymer electrolytes: Synthesis, rheology, and electrochemistry,' *Journal of Power Sources* **89**, 156 (2000)

119. X.W. Zhang, Y. Li, S.A. Khan & P.S. Fedkiw, 'Inhibition of lithium dendrites by fumed silica-based composite electrolytes,' *Journal of The Electrochemical Society* (2004)

120. B. Scrosati, F. Croce & L. Persi, 'Impedance spectroscopy study of PEO-based nanocomposite polymer electrolytes,' *Journal of The Electrochemical Society* **147**, 1718 (2000)

121. C.-W. Nan, L. Fan, Y. Lin & Q. Cai, 'Enhanced ionic conductivity of polymer electrolytes containing nanocomposite SiO_2 particles,' *Physical Review Letters* **91**, 266104 (2003)

122. H.M.J.C. Pitawala, M.A.K.L. Dissanayake & V.A. Seneviratne, 'Combined effect of Al_2O_3 nano-fillers and EC plasticizer on ionic conductivity enhancement in the solid polymer electrolyte $(PEO)_9$ LITF,' *Solid State Ionics* **178**, 885 (2007)

123. A.M. Stephan, 'Review on gel polymer electrolytes for lithium batteries,' *European Polymer Journal* **42**, 21 (2006)

124. F. Capuano, F. Croce & B. Scrosati, 'Composite polymer electrolytes,' *Journal of the Electrochemical Society* **138**, 1918 (1991)

125. J.-H. Ahn, G.X. Wang, H.K. Liu & S.X. Dou, 'Nanoparticle-dispersed PEO polymer electrolytes for li batteries,' *Journal of Power Sources* **119**, 422 (2003)

126. A.S. Best, J. Adebahr, P. Jacobsson, D.R. Macfarlane & M. Forsyth, 'Microscopic interactions in nanocomposite electrolytes,' *Macromolecules* **34**, 4549 (2001)

127. C.-Y. Chiang, M.J. Reddy & P.P. Chu, 'Nano-tube TiO_2 composite PVDF/$LiPF_6$ solid membranes,' *Solid State Ionics* **175**, 631 (2004)

128. P.P. Chu, M.J. Reddy & H.M. Kao, 'Novel composite polymer electrolyte comprising mesoporous structured SiO_2 and PEO/Li,' *Solid State Ionics* **156**, 141 (2003)

129. M. Wagemaker, G.J. Kearley, A.A. Van Well, H. Mutka & F.M. Mulder, 'Multiple Li positions inside oxygen octahedra in lithiated TiO_2 anatase,' *Journal of the American Chemical Society* **125**, 840 (2003)

130. J.F. Snyder, R.H. Carter & E.D. Wetzel, 'Electrochemical and mechanical behavior in mechanically robust solid polymer electrolytes for use in multifunctional structural batteries,' *Chemistry of Materials* **19**, 3793 (2007)

131. C.J. Leo, G.V.S. Rao & B.V.R. Chowdari, 'Studies on plasticized PEO–lithium triflate–ceramic filler composite electrolyte system,' *Solid State Ionics* **148**, 159 (2002)

132. W. Liu, N. Liu, J. Sun, P.-C. Hsu, Y. Li, H.-W. Lee & Y. Cui, 'Ionic conductivity enhancement of polymer electrolytes with ceramic nanowire fillers,' *Nano Letters* **15**, 2740 (2015)

133. Y.-J. Wang, Y. Pan & L. Chen, 'Ion-conducting polymer electrolyte based on poly (ethylene oxide) complexed with $Li_{1.3}Al_{0.3}Ti_{1.7}(PO_4)_3$ salt,' *Materials Chemistry And Physics* **92**, 354 (2005)

134. D. Ravaine, A. Seminel, Y. Charbouillot & M. Vincens, 'A new family of organically modified silicates prepared from gels,' *Journal of Non-Crystalline Solids* **82**, 210 (1986)

135. P.C. Barbosa, M.M. Silva, M.J. Smith, A. Gonçalves, E. Fortunato, S.C. Nunes & V. De Zea Bermudez, 'Di-ureasil xerogels containing lithium bis (trifluoromethanesulfonyl) imide for application in solid-state electrochromic devices,' *Electrochimica Acta* **54**, 1002 (2009)

136. L.M. Bronstein, R.L. Karlinsey, K. Ritter, C.G. Joo, B. Stein & J.W. Zwanziger, 'Design of organic–inorganic solid polymer electrolytes: Synthesis, structure, and properties,' *Journal of Materials Chemistry* **14**, 1812 (2004)

137. S.M.G. Correia, V. De Zea Bermudez, M.M. Silva, S. Barros, R.A.S. Ferreira, L.D. Carlos, A.P.P. De Almeida & M.J. Smith, 'Morphological and conductivity studies of di-ureasil xerogels containing lithium triflate,' *Electrochimica Acta* **47**, 2421 (2002)

138. K. Dahmouche, C.V. Santilli, M. Da Silva, C.A. Ribeiro, S.H. Pulcinelli & A.F. Craievich, 'Silica–PEG hybrid ormolytes: Structure and properties,' *Journal Of Non-Crystalline Solids* **247**, 108 (1999)

139. K. Dahmouche, M. Atik, N.C. Mello, T.J. Bonagamba, H. Panepucci, M.A. Aegerter & P. Judeinstein, 'Investigation of new ion-conducting ormolytes: Structure and properties,' *Journal of Sol-Gel Science and Technology* **8**, 711 (1997)

140. V. De Zea Bermudez, L. Alcácer, J.L. Acosta & E. Morales, 'Synthesis and characterization of novel urethane cross-linked ormolytes for solid-state lithium batteries,' *Solid State Ionics* **116**, 197 (1999)

141. H.-M. Kao, T.-T. Hung & G.T.K. Fey, 'Multinuclear solid-state nmr characterization, ion dissociation, and dynamic properties of lithium-doped organic- inorganic hybrid electrolytes based on ureasils,' *Macromolecules* **40**, 8673 (2007)

142. N.C. Mello, T.J. Bonagamba, H. Panepucci, K. Dahmouche, P. Judeinstein & M.A. Aegerter, 'NMR study of ion-conducting organic- inorganic nanocomposites poly (ethylene glycol)- silica- $LiClO_4$,' *Macromolecules* **33**, 1280 (2000)

143. S.C. Nunes, V. De Zea Bermudez, D. Ostrovskii, M.M. Silva, S. Barros, M.J. Smith, L.D. Carlos, J. Rocha & E. Morales, 'Diurea cross-linked poly (oxyethylene)/siloxane ormolytes for lithium batteries,' *Journal of The Electrochemical Society* **152**, A429 (2005)

144. Y.-C. Pan, D. Saikia, J. Fang, L.-D. Tsai, G.T.K. Fey & H.-M. Kao, 'Synthesis and characterization of a new hyperbranched organic–inorganic solid polymer electrolyte with cyanuric chloride as a core element,' *Electrochimica Acta* **56**, 8519 (2011)

145. M.M. Silva, S.C. Nunes, P.C. Barbosa, A. Evans, V. De Zea Bermudez, M.J. Smith & D. Ostrovskii, 'Sol–gel preparation of a di-ureasil electrolyte doped with lithium perchlorate,' *Electrochimica Acta* **52**, 1542 (2006)

146. L.D. Carlos, V. De Zea Bermudez, R.A. Sá Ferreira, L. Marques & M. Assunção, 'Sol- gel derived urea cross-linked organically modified silicates. 2. Blue-light emission,' *Chemistry of Materials* **11**, 581 (1999)

CHAPTER 3

METHODOLOGY

3.1 Synthesis

3.1.1 Sol-gel Synthesis

The sol-gel process is a method for producing homogeneous, high-purity inorganic metal oxides from small molecules at ambient temperatures, particularly oxides of silicon and titanium materials. It is based on the polymerization of molecular precursors such as metal alkoxides, which are simple and readily available.

The sol-gel process involves dispersion of solid nanoparticles in a liquid to make a colloidal solution (sol), which acts as the precursor to form a continuous three-dimensional network extending throughout the liquid (gel). Typical precursors are metal alkoxides such as tetraethoxysilane (TEOS) because they react readily with water. The precursors first undergo a hydrolysis reaction in which Si-OH groups are produced. Complete hydrolysis of $Si(OR)_4$ results in silicic acid, $Si(OH)_{4;}$ however, condensation reactions can occur instead between two silanol or one silanol and an ethoxy group to form Si-O-Si (Figure 3 - 1). The small molecules formed after condensation continue to grow

larger and larger by polymerization. When catalyzed in acidic conditions, hydrolysis is slower, and the polymerization happens in a more linear fashion with some branches and crosslinks. The gelation occurs due to the branches and entanglement of the molecular chain. On the other hand, under basic conditions, highly branched clusters form because hydrolysis is faster. These discrete clusters are linked and form a 3-dimensional network during gelation. [1–3]

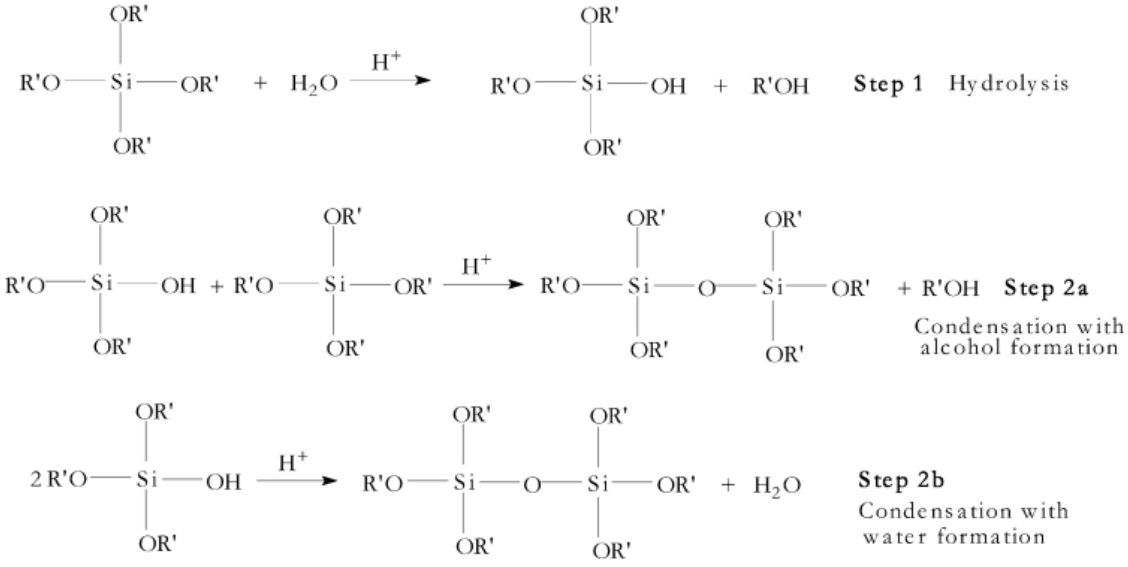

Figure 3 - 1 Hydrolysis and condensation reactions involved in the sol-gel process.

If the gels are supercritically dried, they form aerogels, which have very high surface area and ultra-low densities. The silica skeleton is maintained during extraction of solvent. Xerogels have lower surface area and higher density than aerogels due to drying at ambient conditions. The solvent evaporation rate in xerogel is controlled to be very slow so the network may shrink 50% up to 95% of the original size. [1, 2] Xerogel films can be made by coating, and fibers can be

made by spinning. A schematic of different types of sol-gel products and their structure is shown in Figure 3 - 2. [4]

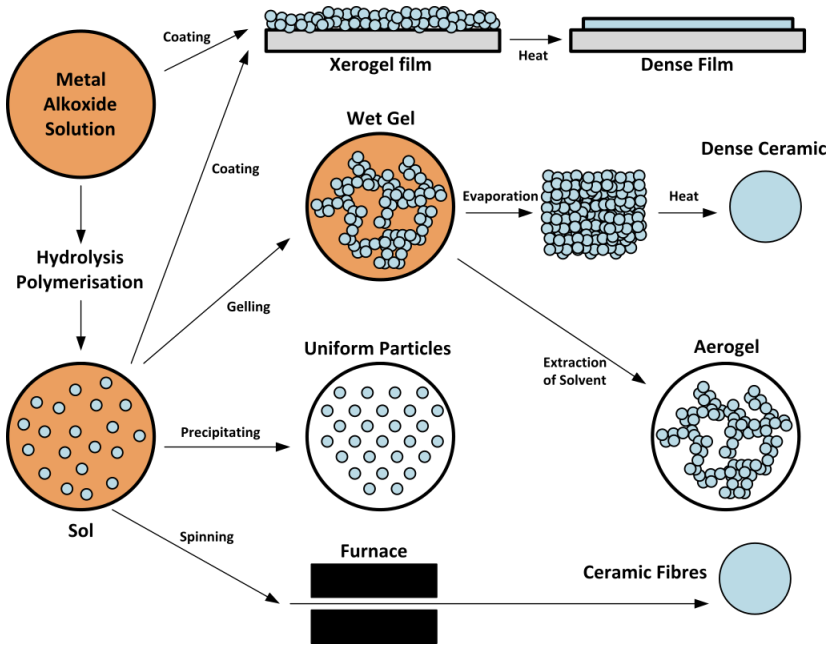

Figure 3 - 2 Different kinds of products made by the sol-gel method.

3.1.2 Sol-gel Synthesis of Organic-inorganic Hybrid Materials

The precursors used in the sol-gel process can be chemically tailored, which makes it possible for sol-gel derived materials to achieve a variety of applications. One area with huge potential has emerged from the wide variety of property modifications that can be achieved by incorporating organic polymers into inorganics by the sol-gel method. This new class of materials are called organic-inorganic hybrid materials. Compared to classical composites which are basically blends of two materials, hybrid materials that combine the organic and inorganic phases with proper chemical interaction may provide totally new properties that combine the good elasticity, toughness, and formability from the

organic phase with the stiffness and stability from the inorganic phase. [3] For example, siloxane based hybrid materials demonstrate tunable properties between those of glasses and polymers, with improved optical properties expand the application to sensors, optics, and membranes. The sol-gel technique is especially suitable for processing organic-inorganic hybrid materials and has been widely used [3, 5–10] because of if its mild reaction conditions, which allow not only incorporation of various organic materials but also well-controlled organic-inorganic composition.

Organic-inorganic hybrid materials can be produced with various starting components and molecular structures. [10] To introduce organics into inorganic materials without phase separation, proper chemical bonding between the two phases during materials processing is necessary. Low molecular weight organoalkoxysilanes can be used as precursors for the sol-gel reaction in which organic groups are combined with an inorganic network through the ≡Si-C-bond. [11–14] Silane coupling agents such as aminoalkyl and glycidyloxyalkyl sialnes can also be used to connect the silica with a desired organic molecule. If the organoalkoxysilanes are not pre-synthesized, co-condensation of functionalized oligomers or polymers with metal alkoxides can also establish organic-inorganic bonds. [15–17] From an opposite point of view, hybrid materials can be achieved via infiltration of previously formed wet gels with properly functionalized organic phases in which chemical interaction can occur between phases. [18–20] In this case, the structure of the inorganic phase can be controlled separately from that of the organics.

3.2 Experimental Techniques

3.2.1 Impedance Spectroscopy

Dielectric impedance spectroscopy (DIS) is a powerful tool to investigate the mechanisms of electrochemical reactions and to measure the dielectric and transport properties of materials. DIS is commonly used to measure the Li^+ transfer mechanisms, including charge transfer resistance, double layer capacitance and diffusion resistance, as well as to monitor the electrolyte for any degrading electrochemical reactions.

With this method, the electrochemical system is under steady state condition in equilibrium. Dielectric impedance is a measure of the ability of a circuit to resist the flow of electrical current.

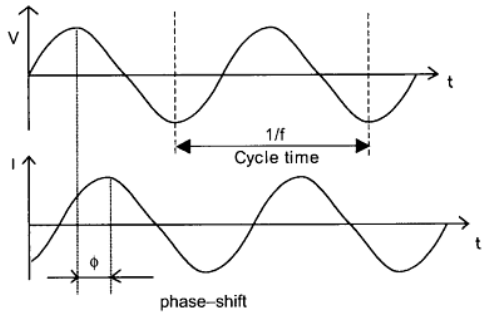

Figure 3 - 3 Sinusoidal voltage input, V, at a single frequency, f, and current response I. [21]

Usually, measurement is done by applying a small AC excitation potential to an electrochemical cell and then measuring the response current signal through the cell. The sinusoidal excitation potential has the form $E_t=E_0 \sin(\omega t)$ where E_t is the potential at time t, E_0 is the amplitude of the potential signal and ω is the radial frequency. Since the excitation signal is small, the response of the sample

is pseudo-linear and the current response is a sinusoid with the same frequency and a phase shift, which has the form $I_t=I_0 \sin(\omega t+\varphi)$, where φ is the phase shift (Figure 3 - 3). [21, 22] It is possible to transform the voltage perturbation and the current response in the Euler representation. The ratio between the perturbation and the response is a frequency-dependent complex number, called impedance. The impedance of the system can be represented as $Z(\omega)=E/I=Z_0(\cos \varphi +j\sin \varphi)$.

DIS data is typically presented in two forms, the Nyquist plot and the Bode plot. In a Nyquist plot, the real and imaginary parts of the impedance are plotted on the X and Y axes, respectively. However, the data points on the Nyquist do not provide any information about the frequency. In the Bode plot, the impedance is plotted with log frequency on the x-axis and both the absolute values of the impedance (|Z|=Z0) and the phase-shift on the y-axis. Typical Nyquist and Bode plots are shown in Figure 3 - 4.[21, 22] Nyquist plots are often used for data analysis because they contain information about capacitance and resistance simultaneously.

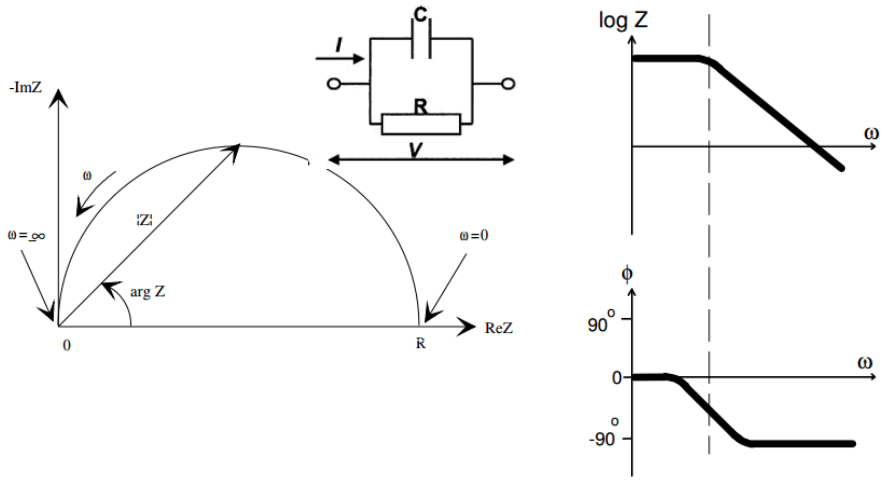

Figure 3 - 4 Typical Nyquist plot (left) and its equivalent circuit and Bode plots.

Since impedance is a measure of the response of a system to an electric signal, it is best to describe the result in terms of electrical components. Equivalent circuit model fitting is the common method used to analyze the DIS data. For example, the semicircle in the Nyquist plot is actually based on the equivalent circuit in Figure 3 - 4. Most of the circuit elements are linear electrical elements such as resistors, capacitors, and inductors. The goal of the model is to find electrical circuits that exhibit a frequency response which is equivalent to that of the cell. This then provides insight into the transport and reaction mechanisms in the sample. The constant-phase element (CPE) and the Warburg element are two other elements that are used to model the behavior of the electrolyte. The impedance and modeling behavior of those elements are summarized in table 1. [21, 22] Warburg elements are commonly used to represent a resistance to mass transfer such as diffusion control. The CPE element is a general element used to model "imperfect" capacitors, in which the degree of imperfection is represented as n. The equivalent circuit models are not unique because there might be several combinations of circuit elements that all fit the experimental spectrum. Therefore, it is necessary to have some basic idea of the behavior of the system in order to pick the right circuit elements.

Table 3 - 1 Commonly used circuit elements in DIS equivalent circuit model analysis

Equivalent Element	Impedance	Modeling behavior
R	R	Resistive behavior

C	$\frac{1}{j\omega C}$	Capacitive behavior
Constant-Phase Element	$\frac{1}{Q_o(j\omega)^n}$	Double-layer
Warburg Element	$\frac{A_W}{\sqrt{\omega}} + \frac{A_W}{j\sqrt{\omega}}$	Semi-infinite diffusion

3.2.2 Brillouin Light Scattering

Brillouin light scattering (BLS) is used to measure the elastic properties of samples based on the interactions between incident light and propagating acoustic phonons in condensed matter. It probes inelastic light scattering events when photons exchange energy with propagating sound waves. The density oscillations associated with acoustic phonons in the solids create fluctuations in the dielectric constant, and consequently give rise to patterns in the refractive index that can be described by a linear combination of plane waves, which establish moving optical gratings. Wave interference among scattered light destroys all but the light scattered from a phonon with wavelength and propagation direction that obeys the diffraction conditions for a given choice of incident and observation optical paths. In other words, the scattering geometry allows one to single out specific sound propagation directions. The energy exchange that takes place during the inelastic scattering event can be thought of as similar to a Doppler effect: if the probed phonon propagates towards the collection optics, i.e., the direction in which the scattered photon emanates, the latter has a higher frequency than the incident light; if the phonon propagates in the opposite direction, the scattered light has a lower frequency. One refers to

these events as anti-Stokes and Stokes, respectively. This frequency shift, ω, is proportional to the phonon velocity, *c*, of the scattering medium according to $\omega = qc$, where q is the wavevector of the phonon. It is defined as the difference between the wavevector of the scattered light and the incident light.

Eq. 3-1 $$\pm\vec{q} = \overrightarrow{k_s} - \overrightarrow{k_i}$$

In BLS, the spectrum of scattered light is analyzed using a Fabry-Pérot interferometer and the interpretation of the spectrum is based on the generalized hydrodynamic theory. The two important quantities that can be obtained from this spectrum are the real and imaginary components of the complex mechanical modulus. The real part, the elastic storage modulus, is derived from the frequency shift between elastically and inelastically scattered light ω.

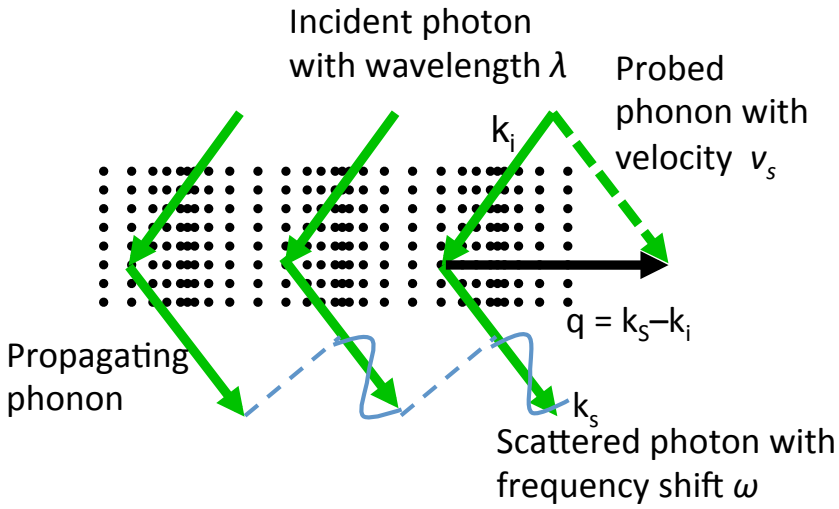

Figure 3 - 5 Schematic of the mechanism of Brillouin light scattering.

Eq. 3-2 $$M'(\omega) = \frac{\rho_0 \omega^2}{q^2}$$

The imaginary part, the loss modulus, is related to the widths of the Brillouin and Rayleigh peaks.

Eq. 3-3 $$M'(\omega) = \frac{\rho_0 \omega}{q^2}[\Delta\omega_B - \frac{\Delta\omega_B}{2}\frac{I_R}{2I_B}]$$

I_R and I_B are the intensities of the Rayleigh and Brillouin peaks, respectively. With the knowledge of the density ρ_0 the elastic modulus of the material can be determined. [23] For sol-gel derived samples, the real part of this modulus reflects the structural integrity and the degree of networking, while the imaginary component provides a measure of the mechanical losses associated with aperiodic motions of structural moieties. [24]

Importantly, because visible light interacts with phonons in the GHz frequency range, this measurement yields the adiabatic elastic moduli. This means no heat is imparted or withdrawn from the scattering medium during the measurement, and no mechanical forcing occurs. The moduli so determined are therefore representative of the equilibrium structure of the sample under consideration here.

3.2.3 Small Angle X-ray Scattering (SAXS)

X-ray scattering provides information about the local electron density in materials. In conventional X-ray scattering, the angle between the incident beam and the scattered beam is labeled as 2θ. This angle is inversely related to the length scale being probed. Therefore, when 2θ is small the probed length scale is large. More specifically, typical 2θ for SAXS range from 0 to 5°, which translate to the feature sizes at the order of 5 to 100 nm length scale. The scattering can be due to chemical heterogeneity and density variations within the sample. As a nanoscale structural characterization tool, SAXS has wide application in determining size of particulates and other ordered systems such as colloids,

fractals, lamellae, and inhomogeneous systems such as two phase systems and polymer chains. The results of SAXS are statistically significant and representative because the signal getting collected is the average over the sample within the beam size area. The electron density inhomogeneity in the samples gives contrast which is related to a net electron density of a scatterer, defined as the difference between it and its environment, ρ_S.

$$\text{Eq. 3-4} \qquad \Delta\rho(\vec{r}) = \rho(\vec{r}) - \rho_S$$

The amplitude of the scattered X-ray, $A(\vec{q})$, is a Fourier transform of the atomic electron density, where $\vec{q}$ is the scattering vector. The scattering intensity per unit volume[25–28] is

$$\text{Eq. 3-5} \qquad I(\vec{q}) = \frac{A(\vec{q})A^*(\vec{q})}{V}$$

Measurement for SAXS is relatively straightforward, with very little of sample preparation, and can potentially provide abundant information about the structure. For example, for a particulate system, the spectrum contains information about mean particle size, size distribution, particle shape, surface of the structure, and mean interparticle distance [29]. However, it is an indirect measure of sizes, and the contrast is relative; complementary measurements such as electron microscopy are necessary for complete determination of the microstructure.

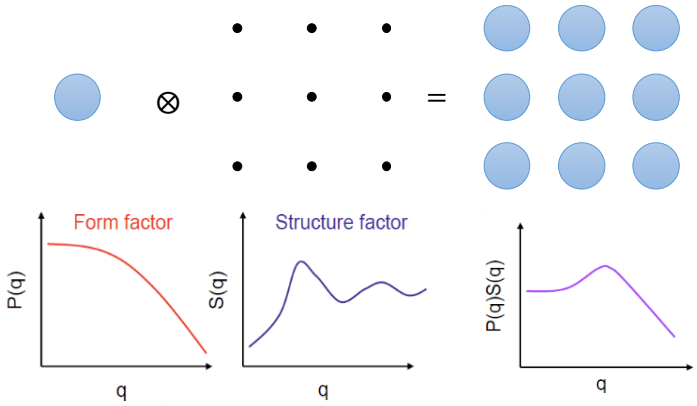

Figure 3 - 6 Structure and form factors in SAXS.

Moreover, the data analysis requires some basic knowledge of the structure. For a typical monodispersed system, the scattering intensity can be written as $I(q) = P(q)S(q)$. $P(q)$ is the form factor, which is a measure of the scattering intensity of a single scatterer assuming it is homogeneous and has contrast with respect to the environment. $S(q)$ is the structure factor which is a description of common spacing between scatterers [30], as represented in Figure 3 - 6. Several theories including Guinier law and Porod law are commonly used in data interpretation of SAXS. Guinier approximation applies at small q and provides information about the radius of gyration R_G of the scatterer.

Eq. 3-6 $$\lim_{q\to 0} I(q) = I(0)\exp\left(-\frac{1}{3}R_G q^2\right)$$

Porod law, on the other hand, is applied at large q values, and is related to interface structures. For different surface features, such as surface or mass fractal or rough surfaces, the spectra of different surface features have different slopes in the Porod region. (Figure 3 - 7)

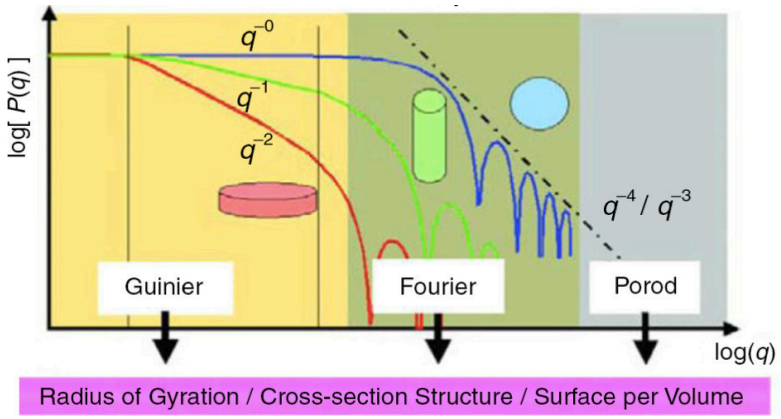

Figure 3 - 7 Regions of SAXS profile and data that may be extracted from each. [31]

3.3 References

1. Brinker C.J. & G.W. Scherer 1990. Sol-gel science: the physics and chemistry of sol-gel processing. Academic press.

2. A.M. Buckley & M. Greenblatt, 'The sol-gel preparation of silica gels,' *Journal of Chemical Education* **71**, 599 (1994)

3. Y.-H. Han, A. Taylor, M.D. Mantle & K.M. Knowles, 'Sol–-gel-derived organic–inorganic hybrid materials,' *Journal Of Non-Crystalline Solids* **353**, 313 (2007)

4. Claudionico, 'Schematic representation of the different stages and routes of the sol-gel technology,' (2013)

5. B. Boury & R.J.P. Corriu, 'Auto-organisation of hybrid organic–inorganic materials prepared by sol–gel chemistry,' *Chemical Communications* 795 (2002)

6. J.J.E. Moreau, L. Vellutini, M. Wong Chi Man & C. Bied, 'New hybrid organic- inorganic solids with helical morphology via h-bond mediated sol- gel hydrolysis of silyl derivatives of chiral (r, r)-or (s, s)-diureidocyclohexane,' *Journal of the American Chemical Society* **123**, 1509 (2001)

7. C. Sanchez, F. Ribot & B. Lebeau, 'Molecular design of hybrid organic-inorganic nanocomposites synthesized via sol-gel chemistry,' *Journal of Materials Chemistry* **9**, 35 (1999)

8. U. Schubert, N. Huesing & A. Lorenz, 'Hybrid inorganic-organic materials by sol-gel processing of organofunctional metal alkoxides,' *Chemistry of Materials* **7**, 2010 (1995)

9. Q.-M. Wang & B. Yan, 'Novel luminescent molecular-based hybrid organic–inorganic terbium complex covalently bonded materials via sol–gel process,' *Inorganic Chemistry Communications* **7**, 747 (2004)

10. J. Wen & G.L. Wilkes, 'Organic/inorganic hybrid network materials by the sol- gel approach,' *Chemistry of Materials* **8**, 1667 (1996)

11. G. Philipp & H. Schmidt, 'New materials for contact lenses prepared from si-and ti-alkoxides by the sol-gel process,' *Journal of Non-Crystalline Solids* **63**, 283 (1984)

12. H. Schmidt, 'Organically modified silicates by the sol-gel process,' MRS Proceedings 32, 327 (1984)

13. H. Schmidt, H. Scholze & A. Kaiser, 'Principles of hydrolysis and condensation reaction of alkoxysilanes,' *Journal of Non-Crystalline Solids* **63**, 1 (1984)

14. H. Schmidt, 'New type of non-crystalline solids between inorganic and organic materials,' *Journal of Non-Crystalline Solids* **73**, 681 (1985)

15. G.L. Wilkes, B. Orler & H.-H. Huang, 'Ceramers-hybrid materials incorporating polymeric oligomeric species into inorganic glasses utilizing a sol-gel approach,' Abstracts of Papers of the American Chemical Society **190**, 109 (1985)

16. G.L. Wilkes, H.-H. Huang & R.H. Glaser, 'New inorganic-organic hybrid materials through the sol-gel approach,' *Advances In Chemistry Series* **224**, 207 (1990)

17. G.L. Wilkes, A.B. Brennan, H.-H. Huang, D. Rodrigues & B. Wang, 'The synthesis, structure and property behavior of inorganic-organic hybrid network materials prepared by the sol gel process,' MRS Proceedings **171**, 14 (1989)

18. B.L. Abramoff & L.C. Klein, 'Pmma-impregnated silica gels: Synthesis and characterization,' San Dieg-DL Tentative, 241 (1990)

19. E.J.A. Pope & J.D. Mackenzie, 'Incorporation of organic dyes in polymer/oxide composites,' *MRS Bulletin* **12**, 29 (1987)

20. E.J.A. Pope, M. Asami & J.D. Mackenzie, 'Transparent silica gel –pmma composites,' *Journal of Materials Research* **4**, 1018 (1989)

21. Lvovich V.F. 2012. *Impedance spectroscopy: applications to electrochemical and dielectric phenomena*. John Wiley & Sons.

22. Barsoukov E. & J.R. Macdonald 2005. *Impedance spectroscopy: theory, experiment, and applications*. John Wiley & Sons.

23. J. Kieffer, 'Mechanical degradation and viscous dissipation in B_2O_3,' *Physical Review B* **50**, 17 (1994)

24. R.E. Youngman, J. Kieffer, J.D. Bass & L. Duffrene, 'Extended structural integrity in network glasses and liquids,' *Journal of Non-Crystalline Solids* **222**, 190 (1997)

25. Feigin L.A., D.I. Svergun & G.W. Taylor 1987. *Structure analysis by small-angle X-ray and neutron scattering*. Springer.

26. G. Fournet & A. Guinier, 'Small angle scattering of x-rays,' *Translated by Walker, CB and Yudowitch, KL In: New York: John Wiley & Sons* 7 (1955)

27. Roe R.-J. 2000. *Methods of X-ray and neutron scattering in polymer science*. Oxford University Press on Demand.

28. Zemb T. & P. Lindner 2002. *Neutrons, X-rays and light: scattering methods applied to soft condensed matter*. North-Holland.

29. A.P. Radlinski, M. Mastalerz, A.L. Hinde, M. Hainbuchner, H. Rauch, M. Baron, J.S. Lin, L. Fan & P. Thiyagarajan, 'Application of SAXS and SANS in evaluation of porosity, pore size distribution and surface area of coal,' *International Journal of Coal Geology* **59**, 245 (2004)

30. J.S. Pedersen, 'Analysis of small-angle scattering data from colloids and polymer solutions: Modeling and least-squares fitting,' *Advances in Colloid And Interface Science* **70**, 171 (1997)

31. H. Schnablegger & Y. Singh, 'The SAXS guide: Getting acquainted with the principles,' *Anton Paar GmbH, Austria* (2011)

CHAPTER 4

POLYMER NANOCOMPOSITE ELECTROLYTES

4.1 Introduction

Polymer solid electrolytes have attracted increasing attention during the past decade because of the higher attainable energy density, the improved safety, and the reduction in weight that these materials can bring about when replacing flammable liquid electrolytes, while maintaining good mechanical flexibility.[1–3] Polyether compounds such as poly(ethylene) oxide (PEO) have good solvation power for lithium salt and can form ethylene oxide-lithium (EO/Li+) complexes.[4–6] However, the room temperature conductivities are often limited by the semicrystalline nature of such polymers because cation transport is largely assisted by the segmental reorientations of the neighboring polymer chains.[7,8] Several approaches have been taken to improve the conductivities of polymers. Plasticizing polymer electrolytes results in higher conductivities but comes at a cost of increased reactivity, where in contact with lithium metal electrode and the gradual loss of the originally intended geometry, which exacerbates the mechanical stability.[9,10]

Introducing ceramic nanoparticle fillers in the polymeric matrix were found to be effective in improving ionic conductivities, mechanical, chemical, and thermal stability.[8,11–13]There are two categories of fillers, passive fillers such as TiO_2,[14–17] Al_2O_3,[18,19] ZnO,[13] ZrO_2,[20] and SiO_2[21,22] does not participate in ion transport directly. The inhibition of crystallinity is believed to be the cause of the enhancement in conductivity, although surface interaction between the fillers and the polymer may occur which provide interfacial region (interphase) for ions to hop through.[14,23–26] Active fillers, such as $Li_{1.4}Al_{0.4}Ge_{1.7}(PO_4)_3$, $Li_{0.33}La_{0.557}TiO_3$ (LLTO) and $Li_{1.3}Al_{0.3}Ti_{1.7}(PO_4)_3$ (LATP) [27–29] share Li species with the matrix and may be able to contribute to the ion transport. High ionic conductivities, up to the order of 10^{-4} $S{\cdot}cm^{-1}$ were reported, however, the underlying mechanism is so far not clear.

However, in these studies for active fillers, the fillers are crystalline and are either particles of 1-10 μm diameter, or fibers with a diameter of 220 nm and a high aspect ratio. Previous research on polymer ceramic composite electrolytes shows that nano-sized fillers are much more effective in improving ionic transport properties than micro-sized fillers due to their large specific surface areas.[17,30] $Li_{1.3}Al_{0.3}Ti_{1.7}(PO_4)_3$ is a Li superionic conductor with a room temperature conductivity of 7×10^{-4} $S{\cdot}cm^{-1}$ in crystalline form. Even amorphous LATP reaches a conductivity of 2.46×10^{-5} $S{\cdot}cm^{-1}$ at ambient conditions.[31] Hence, dispersion of LATP nanoparticles in a PEO polymeric host presents a unique opportunity for

investigating the interplay between Li conducting filler and polymeric host at the interphase.

In the present study, amorphous $Li_{1.3}Al_{0.3}Ti_{1.7}(PO_4)_3$ nanoparticles were synthesized using liquid-feed flame spray pyrolysis (LF-FSP) and nanocomposite electrolytes were fabricated by dispersing these particles in a PEO matrix.[32] We performed a parametric study of the role of lithium ion concentration, particle loading, the type of ceramic filler, and the PEO molecular weight, in affecting cation transport properties. X-ray diffraction (XRD), differential scanning calorimery (DSC), scanning electron microscopy (SEM), Fourier-transform infrared (FTIR) spectrometry, and electrochemical impedance spectrometry (EIS) were employed for characterization. Our study reveals that, besides having an effect on crystallinity and acting as potential source for additional lithium, ionically conducting LATP nanoparticles embedded in a PEO matrix create an interfacial region that is key to enhancing the room temperature ionic conductivity to about 1.7×10^{-4} $S \cdot cm^{-1}$ and reducing the activation energy for cation transport.

4.2 Experimental

4.2.1 Materials

All starting materials are reagent grade and commercially available. Lithium perchlorate [$LiClO_4$], polyethylene oxide [PEO 4M and 900k], lithium hydroxide monohydrate [$LiOH \cdot H_2O$], triethyl phosphate [$(C_2H_5O)_3PO$], triethanolamine [$N(CH_2CH_2OH)_3$], propionic acid [CH_3CH_2COOH], titanium oxide [TiO_2] (Aeroxide® P25) were procured from Sigma-Aldrich (Milwaukee, WI). Acetonitrile and titanium isopropoxide [$Ti(OiPr)_4$] was purchased from Fischer

Scientific (Pittsburgh, PA), aluminum tri-sec-butoxide $Al[OCH(CH_3)CH_2CH_3]_3$ from Chattem Chemicals (Chattanooga, TN), fumed silica (CAB-O-SIL® M-5) from Cabot Corp (Boston, MA), and absolute ethanol from Decon Labs (King of Prussia, PA).

4.2.2 Synthesis of LATP

Amorphous $Li_{1.3}Al_{0.3}Ti_{1.7}(PO_4)_3$ (LATP) nanopowders were synthesized using the LF-FSP method. In this process, stoichiometric amounts of lithium propionate $[LiO_2CCH_2CH_3]$, alumatrane $[Al(OCH_2CH_2)_3N]$, titanatrane $Ti(OCH_2CH_2)_3N[OCH_2CH_2N(CH_2CH_2OH)_2]$, and triethyl phosphate $[(C_2H_5O)_3PO]$, are dissolved in ethanol to give a 3 wt. % ceramic yield solution, which is then aerosolized with oxygen into a quartz chamber where it combusts with oxygen/methane pilot torches. Powders are collected downstream in electrostatic precipitators operated at 10 kV. Details of the nanopowder and the metallo-organic precursor syntheses can be found in our previous publications.[33] From the nitrogen adsorption measurement, the average particle size is determined to be 65 nm, with a standard deviation of 8 nm. The density of the particles is determined as 2.69 g/cm^3.

4.2.3 Synthesis of Polymer-nanocomposite Electrolyte Film

The PEO polymer with molecular weights of 900 K and 4M are dissolved in acetonitrile and magnetically stirred until fully dissolved. $LiClO_4$ is dissolved in the acetonitrile with ethylene oxide at EO/Li molar ratios of 5, 8, 10, 20, 30 or 50. Ceramic nanoparticles are weighed and dispersed in ethanol using ultrasonication for two hours. LATP nanoparticle content is controlled so as to

result in 5, 10, 15, and 20 wt. % loading. The PEO polymer solution is then combined with the lithium salt solution, and subsequently the nanoparticle suspension is added to the polymer-salt solution. The mixture is magnetically stirred for additional 5 hours and cast onto a Teflon plate. Solvent is slowly evaporated under ambient conditions for 24 hours. The PEO-nanocomposite films are peeled from the substrate and further dried under vacuum of $5.0 \cdot 10^{-3}$ Torr and at 50°C for 24 h. The electrolyte films are about 200 μm thick. We used titanium oxide P25 (TiO_2) with an average particle size of 21 nm and fumed silica M5 (SiO_2) with 200-300 nm particle sizes as fillers to create the composite electrolytes with non-conducting fillers.

4.2.4 Materials Characterization

A Bruker Tensor 37 Fourier Transform infrared (FT-IR) spectrometer was used to obtain FTIR spectra over the range of 400-4000 cm^{-1}. The composite electrolyte films as well as the polymer and nanoparticle powders were analyzed using a Rigaku rotating anode goniometer (Rigaku Denki., Ltd., Tokyo, Japan). XRD scans were made using the Cu Kα radiation (1.541 Å) operating at 40 kV and 100 mA in the range of 10° to 40° 2θ, and using a step width of 0.02°. Nanocomposite fracture surface images are taken using FEI Helios Nanolab scanning electron microscopy (SEM). Impedance spectroscopy was used to determine the ionic conductivity. To this end, samples are placed in between two polished stainless steel blocking electrodes and are measured using the Novocontrol broadband dielectric impedance spectrometer from 0 °C to 80 °C, in the frequency range from 0.1 Hz to 10 MHz. Differential scanning calorimetry

(DSC) measurements were performed with a TA2000 calorimeter. Samples are cooled to –75 °C and DSC measurements are performed up to 120 °C with a heating rate 10 K min^{-1} for two cycles. Glass transition temperatures, T_g, are determined from the midpoint of the characteristic step in the experimental heat flow curve.

4.3 Results and Discussion

In this study, a series of nanocomposite samples were prepared with PEO 4M and PEO 900k, LATP nanoparticles with $LiClO_4$ as the lithium source. FTIR spectroscopy is used to investigate chemical complexation between phases. Morphology and particle dispersion are studied using SEM imaging. We assess the effects of lithium composition, different polymer molecular weights, and LATP nanoparticle loadings on the degree of crystallinity and glass transition temperatures by combining XRD and DSC analyses. Each of these factors is evaluated as to how it affects, the ionic conductivity and activation energy for cation migration in polymer matrix nanocomposite electrolytes.

4.3.1 FT-IR Spectroscopy

The IR spectra of pure PEO polymer, LATP nanoparticles, $LiClO_4$ and a typical PEO-nanocomposite films are presented in Figure 4 - 1. The peaks at 2876 and 1095 cm^{-1} in pure PEO 900k are assigned to the vibrations of C-H and C-O bonds, respectively.[34] In addition to those, the peaks at 1090, 1058, 1142 and 839 cm^{-1}, characteristic of pure PEO, also appear in the nanocomposite. The doublet at 950 cm^{-1} has contributions from both LATP and PEO. Comparing spectra of pure PEO and LATP with those of the nanocomposite, there are no

obvious shifts, shape changes, disappearance, or appearance of spectral features, suggesting that LATP is not forming complexes, but is mechanically dispersed in the polymer matrix. Peaks at 617 cm^{-1} and 1052 cm^{-1} in $LiClO_4$ are also observed at corresponding positions in the spectrum of the composite electrolyte. However, peaks at 3547, 3520 cm^{-1} broaden and shift to the right, while the peak at 1620 cm^{-1} broadens and shifts to the left, and the peak at 667 cm^{-1} disappears in the spectrum of the nanocomposite. These results indicate that complexation between $LiClO_4$ and PEO has occurred, which agrees well with previously reported observations.[35,36]

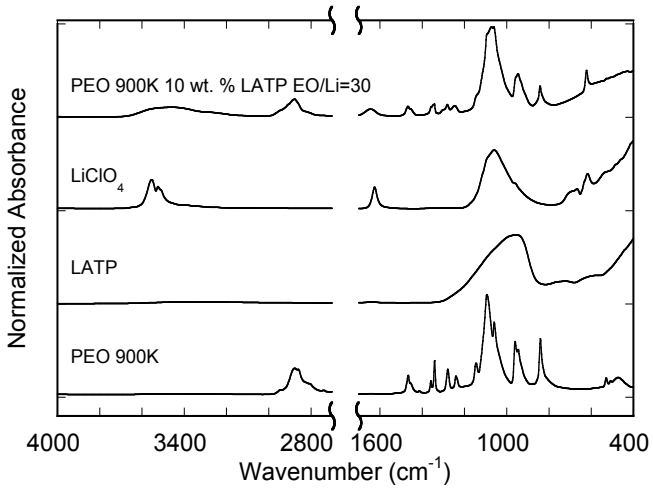

Figure 4 - 1 FTIR spectra of the nanocomposite electrolyte, $LiClO_4$, LATP, and PEO 900k.

4.3.2 Morphology

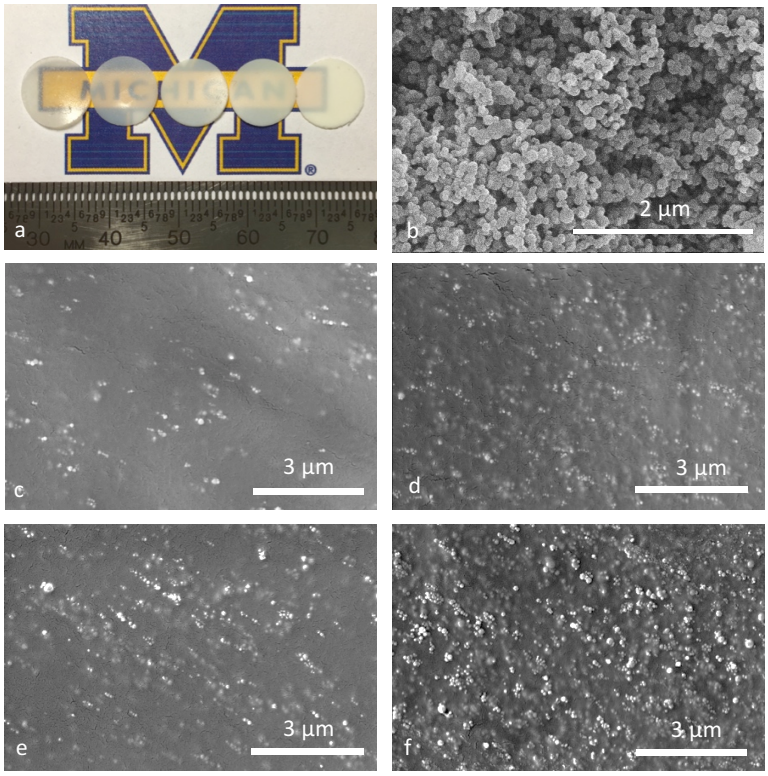

Figure 4 - 2 (a) Photograph of composite films; (b) SEM image of LATP particles, as collected from flame spray pyrolysis; SEM images of nanocomposite samples with (c) 5 wt. % (d) 10 wt. % (e) 15 wt. % and (f) 20 wt. % LATP nanoparticles.

Figure 4 - 2 (a) shows the picture of samples with between 0 and 20 wt.% loading of LATP. The films are free standing and translucent. The translucency decreases with increasing LATP loading. Figure 4 - 2 (b) shows an SEM image of LATP particles. Particles are spherical and homogeneous with average size 65±8 nm. Based on the SEM image, particle sizes are nearly monodisperse, which has already been established in numerous previous studies of nanoparticles synthesized by LF-FSP.[37–39] The fracture surfaces of PEO-$LiClO_4$-LATP nanocomposite films were examined using SEM, and micrographs shown in Figure 4 - 2 (c)-(f) reveal the morphology of PEO 900k-$LiClO_4$-LATP

nanocomposite with LATP varying from 5 to 20 wt.%. Sharp bright dots are the nanoparticles at the fracture surface, while blurry dots are particles beneath the surface. The particle sizes are uniform while the degree of dispersion varies with the LATP loading. Practically complete dispersion is observed at 5 and 10 wt. % of LATP. However, agglomerates of particles start to appear and grow in size as the nanoparticle loading is further increased.

4.3.3 XRD Studies

The XRD patterns of the PEO-LATP-$LiClO_4$ nanocomposites presented in Figure 4 - 3 are normalized with respect to the integral scattering intensity. Figure 4 - 3 shows the results for pure PEO, $LiClO_4$, LATP and nanocomposite electrolyte film with various nanoparticle concentrations. The characteristic peaks for pure PEO at 19.3° and 23.4° reveal the partially crystalline structure of pure PEO. The XRD pattern of LATP shows a weak and very broad feature centered at ~24°, confirming its amorphous nature. The pattern of $LiClO_4$ shows characteristic peaks at 13.5°, 18.3°, 21.3°, 23.3°, 24.6°, 25.0°, 31.7°, 33.2°, 35.8°, and 39.6°. All these peaks disappear for the nanocomposites, indicating that lithium perchlorate salt is fully dissociated to form complexes with the PEO polymer matrix. Figure 4 - 3 also suggests that introducing amorphous LATP nanoparticles suppresses crystallization of the polymer matrix.

The side pane to Figure 4 - 3 shows the XRD patterns for films with different lithium compositions, but with the same nanoparticle loading (10 wt. %). For EO/Li = 20 and 30, a single strong peak at 19.3° and a group of strong peaks at around 23.4° are distinctly visible, indicating a high degree of crystallinity of the

PEO matrix. These peaks diminish as the lithium composition increases, and eventually becomes a very broad band centered at 21° for EO/Li=5, which means that the nanocomposite is almost completely amorphous at this composition. Our observation confirms the plasticizing effect of adding lithium salt to the PEO matrix, which has already been reported by other authors.[8,40] Compared to dispersing LATP nanoparticles in the polymer, the effect of adding $LiClO_4$ on suppressing the polymer crystallinity is more obvious.

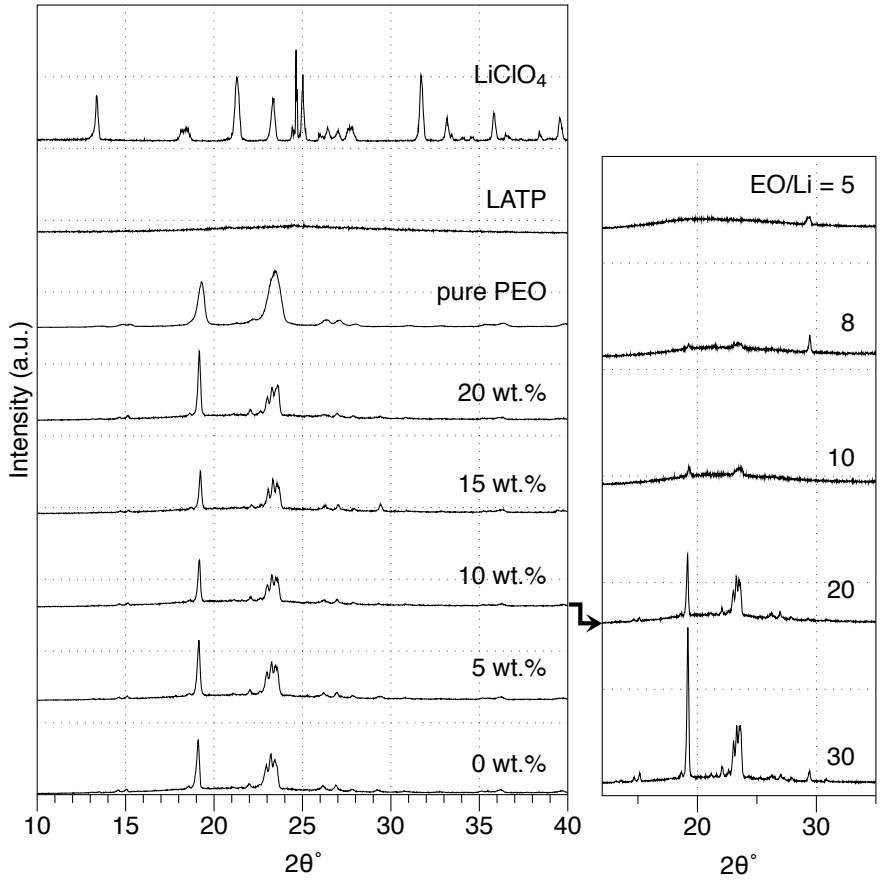

Figure 4 - 3 X-ray diffraction patterns of pure PEO 900k, LATP and $LiClO_4$, PEO-$LiClO_4$-LATP nanocomposite with PEO 900k, EO/Li=20 and various LATP concentrations. Side pane: nanocomposites with 10 wt. % LATP and various EO/Li ratios at room temperature. (The two diffraction patterns linked by the arrow are identical.)

4.3.4 DSC studies and Crystallinity

Thermal properties are determined during the second scan of DSC measurements, while the first scan serves to erase the thermal history the samples had been subject to. Examples of typical DSC thermograms, revealing the glass transition and melting temperatures of polymer obtained for PEO-LATP-$LiClO_4$, PEO-TiO_2-$LiClO_4$ PEO-SiO_2-$LiClO_4$ with PEO Mw 4M are shown in Figure 4 - 4 (a). The downward sigmoidal shapes in the thermal traces, with midpoints, i.e., measured T_g values, ranging from -14°C to -16°C, reflect the glass transition of the nanocomposite. Endothermic peaks are observed at higher temperatures for most of the samples, which are attributed to the melting of the PEO-$LiClO_4$ complex. The percentage of crystallinity, χ_c can be calculated as $\chi_c = \frac{\Delta H_m}{\Delta H_m^0}$, where ΔH_m is the melting enthalpy obtained from the DSC measurement and ΔH_m^0 is the melting enthalpy of pure 100% crystalline PEO (188 J/g).[41]

According to Figure 4 - 4 (a), comparable results are observed for T_g, T_m, and the degree of crystallinity, independent of the type of ceramic filler. By a slight margin, composites with SiO_2 particles exhibit the highest T_g and T_m. TiO_2 nanoparticles lower T_g more, whereas crystallinity is 4 to 10 % higher than for the other composites, as is evident by the deeper melting endotherms. The comparable thermal traces for different types of fillers suggest that the influence of the additive type on the thermal properties and degree of crystallinity is minor. Similarly, no definitive correlation between these properties and particle size or chemical properties is observed.

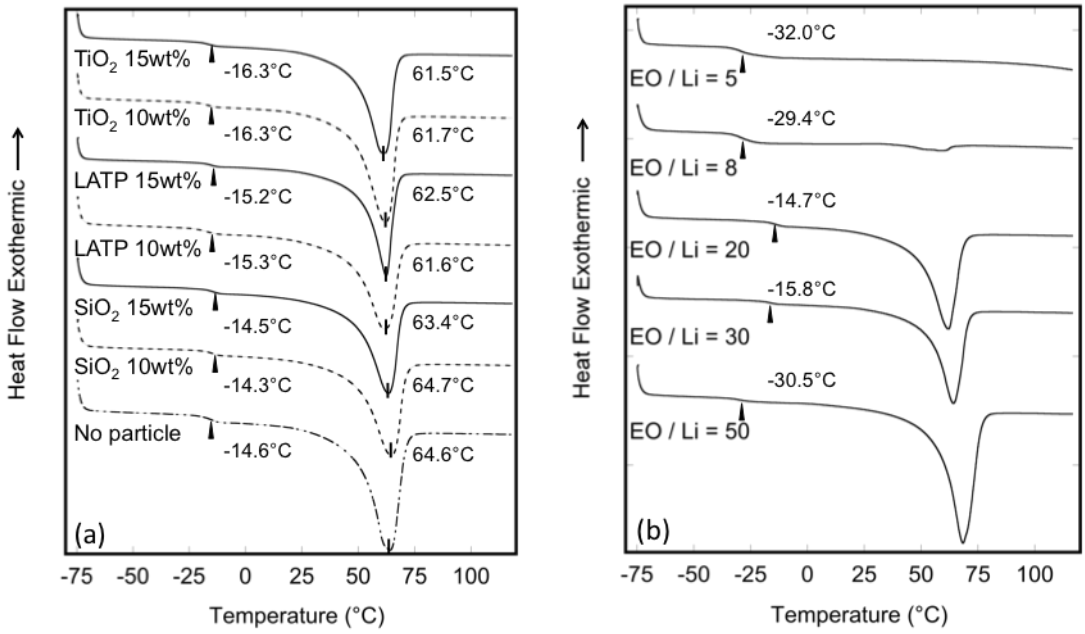

Figure 4 - 4 DSC thermograms of (a) selected PEO 4M-$LiClO_4$ with EO/Li=20 and with no fillers and with different fillers (b) selected PEO-$LiClO_4$-LATP (10 wt. %) nanocomposite with different lithium composition.

Figure 4 - 4(b) illustrates the effect of the lithium concentration on T_g and χ_c. The glass transition becomes more discernable, reaching a maximum at EO/Li =20, whereas the melting endotherms weaken with the addition of lithium salt. As a result, the degree of crystallinity decreases monotonically with increasing Li^+ concentration, from 56% crystallinity for samples with EO/Li=50 to almost completely amorphous at EO/Li=5, as shown in Figure 4 - 5(a). The addition of lithium salt inhibits crystallization of polymer chains because a larger fraction of the chains form complexes with Li^+ and dissociate the salt.

On the other hand, the loading of the ceramic fillers has a minor effect on T_g and χ_c compared to that of lithium concentration. As shown in Figure 4 - 5 (b), the difference in T_g for different LATP wt. % is within 2 °C. T_g reaches a minimum at 10 wt. % LATP nanoparticle concentration. Although the change in

temperature is negligible compared to that achieved by changing the lithium concentration, the minimum in T_g directly aligns with a maximum in conductivity, discussed below. The addition of LATP nanoparticles gradually reduces the χ_c from 45% to 37%. This is expected for most nano- and micro-sized fillers, since they constitute physical obstacles that prevent linear polymer chains from developing a regular alignment. This reduction in the degree of crystallinity due to nano-sized filler is also reported in other studies.[18,42]

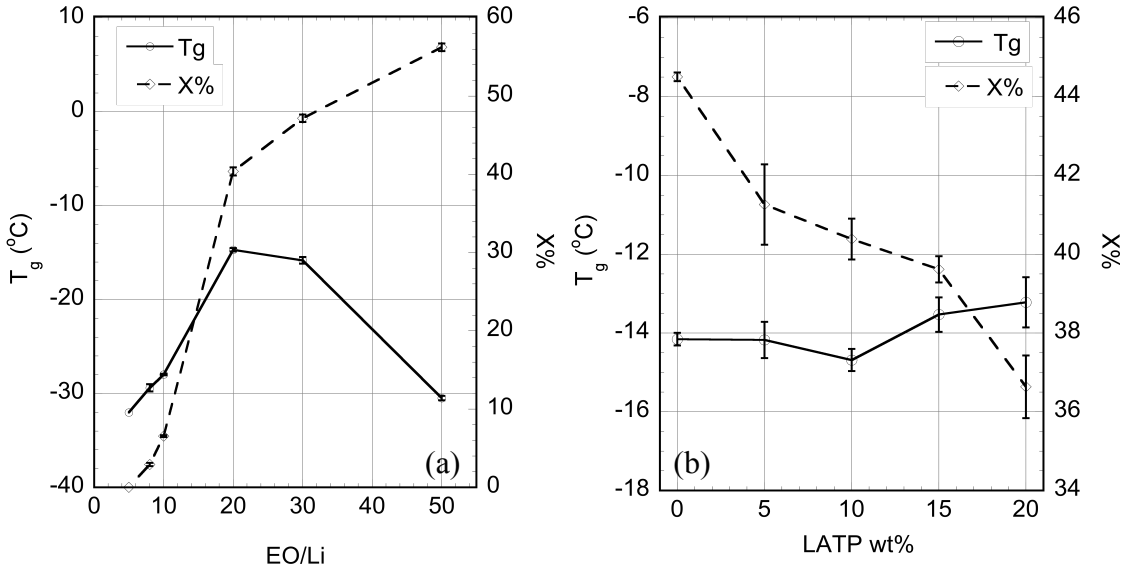

Figure 4 - 5 (a) Effect of lithium ion composition and (b) LATP nanoparticle composition on the glass transition and the degree of crystallinity of PEO 900k-$LiClO_4$-LATP nanocomposite electrolytes with EO/Li=20.

4.3.5 Ionic Conductivity

Conductivity data for samples with different polymer chain length, particle types, and lithium salt concentration are compiled in Figure 4 - 6 (a) through 6(c). The inset in Figure 4 - 6 (c) shows a typical Nyquist plot for the dielectric impedance of the nanocomposite with PEO 900k, 10 wt. % of LATP nanoparticle loading, and a EO/Li ratio of 10 at 0, 20 and 40 °C. A well-defined, slightly

depressed semicircle at high frequencies due to ion conduction and a spike at low frequencies due to electrode polarization, are apparent at all temperatures. As the temperature increases, the radius of the semicircle decreases, indicating an increase in ionic conductivity. The typical equivalent circuit consisting of a parallel RC circuit, where R is the bulk resistance and C is the geometric capacitance, in series with a Warburg element, fits the measured spectra well.

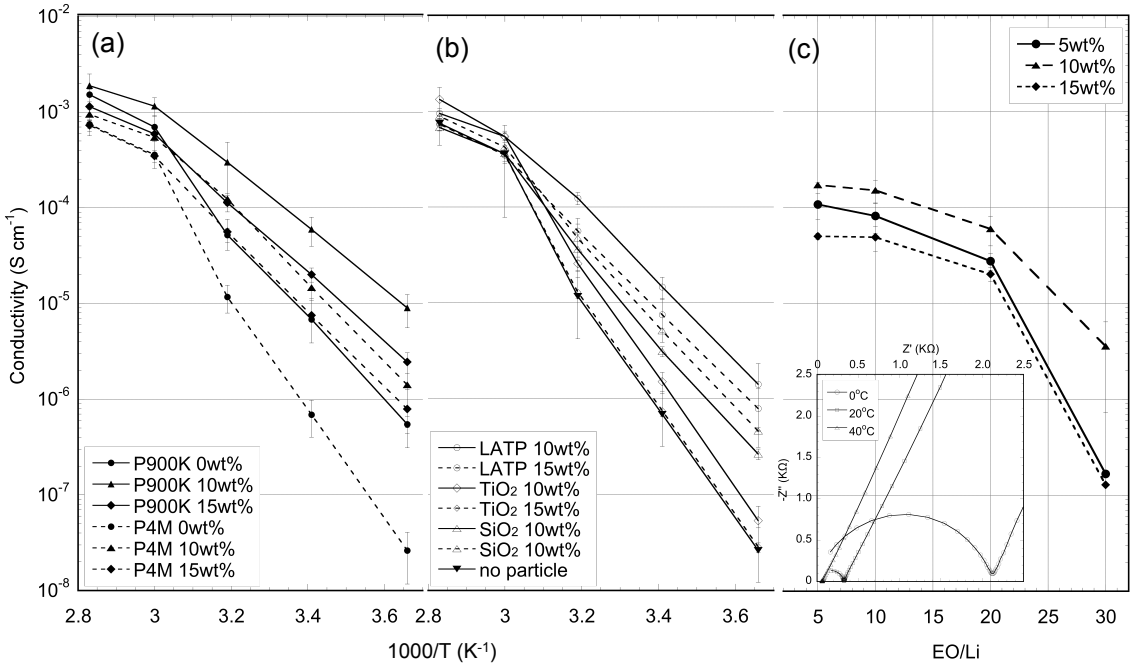

Figure 4 - 6 Arrhenius plots of PEO-LiClO$_4$-LATP nanocomposite at EO/Li=20 with (a) two different PEO molecular weights, and 0, 10, and 15 wt. % LATP, and (b) PEO 4M containing different fillers. (c) Ionic conductivity as a function of EO/Li with PEO 900k, 0, 10, and 15 wt. % LATP at 20°C. Inset: Nyquist plot for nanocomposite with PEO 900k, 10 wt.% LATP nanoparticles, and EO/Li ratio of 10 at 0°C at 20°C and 40°C.

The effect of polymer chain length on conductivity is revealed by comparing data for samples made with PEO 900k and PEO 4M. Figure 4 - 6 (a) shows the temperature dependence of the ionic conductivity of electrolytes with these two different molecular weights, for three different LATP concentrations, and at fixed

EO/Li ratio of 20. For all surveyed LATP concentrations, the electrolyte with the lower molecular weight (PEO 900k) exhibits the higher ionic conductivity. The difference is very obvious at the lowest temperature. As revealed by the DSC measurements, the higher degree of crystallinity that develops with the longer-chain polymer for the same amount of filler correlates with a reduction in ionic conductivity.

The effect of filler type on the ionic conductivity is evaluated by comparing three nanoparticle chemistries. These include active fillers, i.e., where lithium conduction is possible within the filler phase itself, and passive fillers that contain no lithium and block its passage. Figure 4 - 6 (b) shows the Arrhenius plots of nanocomposite electrolytes with different fillers and filler concentrations for PEO 4M. Two different particle concentrations, are compared, i.e. 10 wt. % and 15 wt. %, as several previous studies report this compositional range to be optimal for cation transport,[11,21,34,43] and which is consistent with the result of our study.

To gain insights into the cation transport mechanisms, especially in terms of the molecular structural obstacles lithium have to overcome during migration, we gauge the energy associated with this activated process from the temperature dependence of the Li^+ conductivity. For our materials this temperature dependence is well described by the Vogel-Tammann-Fulcher (VTF) formalism, which is a typical model for describing the ionic mobility in amorphous polymers. The conductivity data below the melting temperature are fitted using the VTF equation

$$\text{Eq. 4-1} \qquad \sigma(T) = AT^{-1/2}\exp\left(\frac{-B}{k_B[T-T_0]}\right)$$

where A is the pre-exponential factor, B is the pseudo-activation energy for ion conduction, k_B is Boltzmann constant and T_0 is a reference temperature. The pseudo-activation energies resulting from the best fits of our data are listed in Table 4 - 2. They range from 1.68 kJ mol^{-1} to 71.62 kJ mol^{-1} for various nanoparticle concentrations below the melting temperature. PEO-LATP systems show lower B values compared to TiO_2 or SiO_2 containing systems. At higher temperatures (≥80 °C), when PEO melts, the polymer chain mobility is naturally higher, and the influence of the fillers on conductivity, regardless of type, is small, and all slopes of the log conductivity vs. reciprocal temperature have similar magnitude. Our calculated pseudo-activation energies for the TiO_2 and SiO_2 nanoparticle systems are in good agreement with those reported in the literature.[44] As shown in Table 4 - 1 and Table 4 - 2, with fixed lithium ion composition, the pseudo-activation energy has a minimum at 10 wt. % of LATP. Again, this concentration of nanoparticles appears to be associated with optimal conditions for ion transport.

Table 4 - 1 Activation energies of PEO 4M-$LiClO_4$ with selected fillers at EO/Li = 20.

Filler type	Filler wt. %	Activation Energy (kJ mol^{-1})
N/A	0	69.44
LATP	10	1.68
LATP	15	6.42
TiO_2	10	33.51
TiO_2	15	61.62
SiO_2	10	71.02
SiO_2	15	32.58

Table 4 - 2 Activation energies of PEO 900k-$LiClO_4$-LATP with various filler content, and EO/Li = 20.

Filler type	Filler wt. %	Activation Energy (KJ mol-1)
LATP	0	49.71
LATP	5	2.49
LATP	10	2.10
LATP	15	4.05
LATP	20	44.23

Finally, the effect of lithium ion concentration on the conductivity of the PEO-LATP nanocomposite series with PEO 900k is illustrated in Figure 4 - 6 (c), where the conductivity at 283 K (20 °C) is plotted as a function of the EO/Li ratio for samples with three different LATP loadings. Samples with low EO/Li ratio exhibit higher ionic conductivities for all three LATP compositions studied. In this study, the highest ionic conductivity of 1.71×10^{-4} S/cm at 20°C is achieved for PEO 900k with 10 wt.% LATP nanoparticles and EO/Li=5. According to the thermal analysis, the degree of crystallinity in these materials decreases with lithium concentration.

Hence, based on the data presented in Figure 4 - 6 we observe that the addition of nano-particles to a polymer matrix, the reduction of the average polymer chain length, and the increase in lithium salt concentration all result in an increase of lithium ion conductivity, while at the same time suppressing crystallization of the polymer phase. Our findings are in agreement with those of several previous studies results reported in the literature,[18,42] and consistent with the interpretation that increasing the volume fraction of amorphous polymer facilitates a stronger participation of the matrix in the transport process, which

increases ionic conductivity, presumably through segmental chain reorientation. However, the reason why active particles exert a so much stronger influence on ionic conductivity than passive ones is not evident from these observations alone, and requires further examination.

First, it is important to note that, based on steric and chemical factors, the mechanism by which Li suppresses crystallization must be different from that by which nanoparticles achieve their influence, i.e., in a more elementary way that stabilizes the structure of the polymer in an amorphous state capable of pronounced segmental motion (plasticizing effect). In other words, the effect that Li salt has on the polymer structure directly enhances the mobility of lithium itself, in a manner that stands apart from suppressing crystallization. This, in turn, could explain why dispersion of lithium containing nano-particles has the ability to effect an interphase formation that is beneficial for cation transport. Second, the fact that the LATP filled composites show the highest conductivities does not correlate with trends that are suggested by either glass transition temperatures, degree of crystallinity, or particle size. Smaller nanoparticles tend to exhibit stronger interactions with the polymer matrix,[9] but average sizes for TiO_2, fumed silica and LATP are 21 nm, 200-300 nm, and 65 nm, respectively. Third, the minimum in the activation energy as a function of the LATP nanoparticle fillers content (see Table 4 - 2) suggests that there exist two opposing influences on the creation of ion transport pathways as a function of the nanoparticle loading. In the following, this behavior is analyzed in detail.

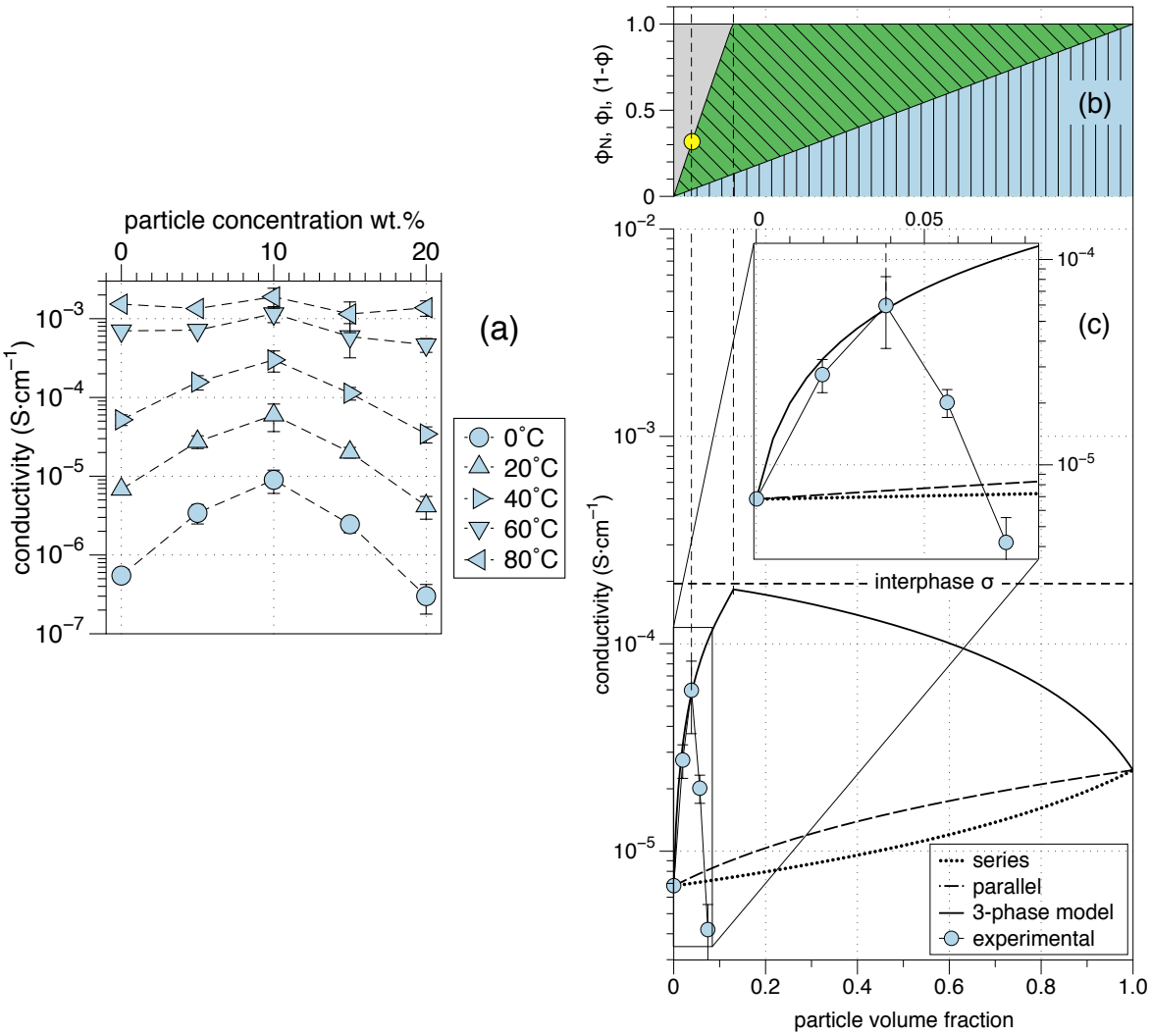

Figure 4 - 7 (a) Ionic conductivities as a function of LATP content in PEO-$LiClO_4$-LATP nanocomposite electrolyte with EO/Li=20 at various temperatures; (b) estimated volume fractions of nanoparticles, interphase, and doped polymer; and (c) three-phase model: measured ionic conductivity at room temperature (circular symbols), as well as the upper and lower bounds of conductivity assuming a mixture of polymer and nanoparticles, and the projected maximum conductivity assuming the participation of an interphase as a third composite component. The ionic conductivity of the interphases is derived from a best fit of a three-phase equivalent circuit model to the ascending flank of the experimental data (see text).

Figure 4 - 7(a) presents the ionic conductivities of PEO-LATP nanocomposite electrolytes as a function of LATP content and at fixed lithium composition, EO/Li=20. A clear maximum is seen at 10 wt. % LATP for all temperatures (i.e. 5.97×10^{-5} S·cm^{-1} at 20 °C and 1.90×10^{-3} S·cm^{-1} at 80 °C). This maximum echoes the minimum in the glass transition temperature that we observed. The reduced degree of crystallinity could account for part of this conductivity enhancement. However, by introducing more lithium sources, the crystallinity is reduced by about 45%, and the ionic conductivity is enhanced by 2-3 orders of magnitude. Whereas, when varying the LATP content, the change in crystallinity is minor, about 2 %, and the enhancement in ionic conductivity is still more than one order of magnitude. This again suggests that suppression of crystallinity is not the dominant variable in controlling conductivity, and that other mechanisms of enhancement are present.

It has been suggested that the presence of ceramic fillers establishes the necessary conditions for a lithium ion hopping mechanism along the surface of these filler particles by creating defects that provide for low-energy barrier hopping conduits for cation migrating.[24–26] However, within the composite, the LATP nanoparticles occupy a volume fraction of less than 7.5%. Unless their spatial placement is highly non-random, we therefore do not expect that, despite being an ion conducting material, these particles would provide percolating conduction pathways that relies on direct contact between particles. We therefore submit the notion that structural features of the polymer that provide for enhanced cation mobility extent substantially beyond a molecularly thin contact

layer. Moreover, because the LATP particles are small, they possess significant interfacial area per unit volume of the host polymer, and consequently, the particles likely affect a much larger volume fraction of the composite in terms of facilitating ionic conduction.

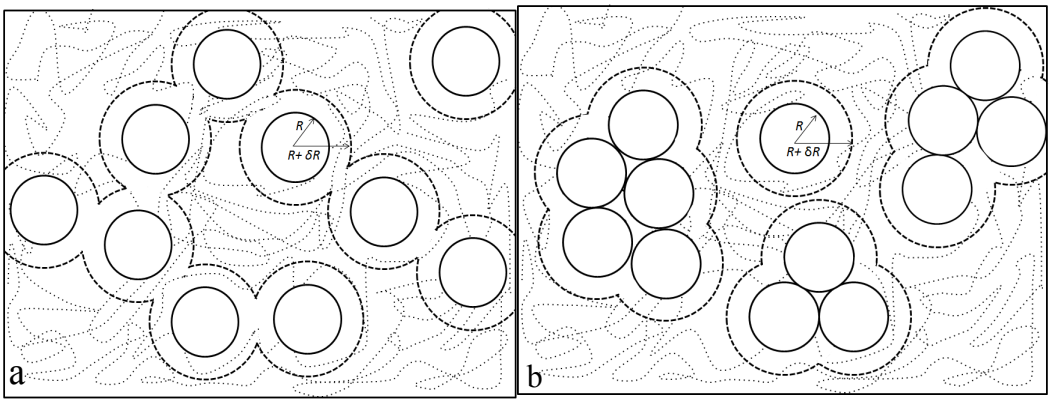

Figure 4 - 8 Schematic representations of the nanoparticle and the interphase region in polymer matrix (a) at percolation and (b) after agglomeration.

It has been posited that near the polymer-particle interface structural effects due to the interaction between phases may range from chain reorientation to chemical or physical bonding between constituents.[45–50] Typically, the more malleable phase is compelled into forming the interphase region, which in our case would be the polymer surrounding the particles. Various authors estimate that the ratio of interphase thickness, h_0, to the particle radius could reach up to 2-3,[46,47,51] depending on particle size. In any event, the interphase structure is disrupted compared to the bulk polymer, and it is reasonable to expect that this structure contains significant quantities of interstices allowing for the aforementioned low-energy barrier ion migration. In terms of Li conductivity, accounting for the interphase region significantly increases the volume fraction of

the more highly conductive phase. Even by merely doubling the effective particle size, i.e., $h_0 = R$, where R is the particle radius, we reach the classical percolation threshold of about 33 vol.% conductive phase with only about 4 vol.% actual nanoparticle loading, which coincides with maximum in conductivity we observe. Moreover, we can expect that the interphase structure adjust in a diffuse manner to that of the bulk near the perimeter of the interfacial region, so that the transitions in properties such as conductivity are not particularly sharp.

4.4 Tri-Phase Model

To quantitatively assess the role of the interphase on the Li ion conduction process, in the following, we offer an analysis that first provides an estimate of the volume fractions of nanoparticles, interphase region, and polymer matrix, and based upon this estimate, especially within the critical low-concentration regime in which we expect percolation across the interphase, we establish an equivalent circuit model to describe the conductivity as a function of the material's phase composition. The schematics of the composite structures shown in Figure 4 - 8 serve to illustrate the rational behind this analysis.

Our starting premise is that the observed maximum in conductivity cannot be explained based on a simple mixture of only two components: amorphous LATP and PEO-$LiClO_4$ with EO/Li=20. The circular symbols in Figure 4 - 7 (b) represent again the measured room temperature conductivity data, this time as a function of the volume fraction of nanoparticles. Superimposed are the expected conductivity bounds. The lower limit corresponds to situation when the two phases are configured in series (thick dotted line) and the upper bound when

they are configured in parallel (thick dashed line). Evidently, the measured values exceed these bounds significantly around 4 vol.% LATP, which already suggest that at least one additional, more highly conducting phase or feature must be involved, and that this is most likely the interphase.

We therefore consider a tri-phase system: the nano-particles, the interfacial region, and the polymer containing lithium salt. All three phases are ionically conducting, and their respective conductivities are σ_N, σ_I, and σ_P. The corresponding volume fractions are ϕ_N, ϕ_I, and $(1-\phi)$, where $\phi = \phi_N+\phi_I$. In this situation, ϕ_N and ϕ_I are linked, as we can envision the interphase to form a halo around the particles that extends to a radius of $(1+\delta)\cdot R$, where δ is a factor that represents the interphase layer thickness, and that ranges between 2 and 3.[46,47,51] To illustrate, consider for simplicity a spherical particle shape, the volume fraction of the nanoparticles can be expressed as

Eq. 4-2 $$\phi_N = \frac{4n\pi R^3}{3V},$$

where n/V is the number density of particles. At low concentrations of nanoparticles, the combined volume fraction of nanoparticles and interphase can be reasonably approximated as

Eq. 4-3 $$\phi = \phi_N + \phi_I = \frac{4n\pi R^3}{3V} + \frac{4n\pi\left[3\delta\left(1+\delta\right)+\delta^3\right]R^3}{3V}.$$

The second term on the right hand side of this equation represents ϕ_I. With increasing concentration of nanoparticles, the interphase regions surrounding each particle begin to overlap, and hence this second term overestimates the

volume fraction of interphase. Moreover, in the higher volume fraction regime, where the geometry of overlapping interphases and impacting nanoparticles is complex, the assumption of spherical shapes is no longer meaningful. We therefore generalize the expression by substituting $\left[3\delta\left(1+\delta\right)+\delta^3\right]=f$, a simple factor that describes the interphase skin, so that the above expression simplifies to

Eq. 4-4 $$\phi=\phi_N\left(1+f\right).$$

Moreover, *f* has to be dependent on ϕ in such a way that it is largest when ϕ is zero and tends to zero when ϕ approaches unity. To obtain a function representation of this composition dependence for *f* we follow an approach similar to that proposed by Johnson et al.,[52] knowing that *f* must decrease as ϕ_N increases. The rate of decrease is inversely proportional to the volume fraction of polymer ($1-\phi_N$), into which the interphase can readily expand into, and can be written as

Eq. 4-5 $$\frac{df}{d\phi_N}=-\frac{k}{1-\varepsilon\phi_N},$$

where the factor $\varepsilon < 1$ has been inserted to avoid the singularity at $\phi_N = 1$ and can be chosen arbitrarily close to, but not equal to one. Separation of variables and integration then yields

Eq. 4-6 $$df=-\frac{k}{\varepsilon}\frac{d\left(\varepsilon\phi_N\right)}{1-\varepsilon\phi_N}=\frac{k}{\varepsilon}d\ln\left(1-\varepsilon\phi_N\right)\Rightarrow f=\frac{k}{\varepsilon}\ln\left(1-\varepsilon\phi_N\right)+f_0$$

At $\phi_N = 0$, $f = f_0 = 3\delta_0\left(1+\delta_0\right)+\delta_0^3$, and at $\phi_N = 1$, $f = 0 \Rightarrow k = -\varepsilon f_0 / \ln\left(1-\varepsilon\right)$.

While this model significantly overestimates the volume fraction of interphase at high nanoparticle concentrations, it provides a reasonable description of the materials behavior upon approaching the threshold at which all remaining polymer phase is sufficiently affected by the nanoparticles to have structurally converted from bulk to interphase. A more accurate model is not warranted, as this analysis only serves to provide a sensible estimate for the ionic conductivity of the interphase and, as we will see, the nanoparticle loading that would provide the highest overall conductivity of the composite. These quantities depend on the materials behavior well below the percolation threshold for conduction across nanoparticles.

The phase proportions derived from this model are shown in Figure 4 - 7(b) in a cumulative fashion: the vertically hashed area corresponds to the volume fraction of LATP nanoparticles, the obliquely hashed area to that of the interphase, and the gray area to that of Li-doped polymer with bulk material structure. The volume fraction of each phase can be taken from this graph at any composition as the vertical distance between demarcations. We assume that interphase layer thickness is equal to the particle radius.[46,47,51] Note that bulk polymer structure only persists to about 13 vol.% nanoparticles, beyond which all remaining polymer as assumed the interphase structure. Also, for $\delta = 1$, percolation in three dimensions across the combined nanoparticle-interphase region occurs at 4 vol.% nanoparticle loading (indicated by the circular mark),

where the measured conductivity has its maximum. Keep in mind that these two phases are always geometrically linked.

Given, that the percolation across the highly conductive phases occurs at such a low concentration, and that because of the expectedly diffuse boundary of the interphase region, the percolation threshold may not be sharply defined, it is appropriate to consider for the prevalent equivalent circuit three elements in parallel: doped bulk polymer that occupies the volume fraction (1–ϕ), continuous channels of interphase contributing ϕ_I to the mixture, and a fraction ϕ_N of the volume occupied by a random mixture of nanoparticles, in which interphase, nanoparticles, and doped bulk polymer act as elements in series. As stated before, percolation across the LATP phase is unlikely in this regime. On the other hand, at low particle concentrations the interphase occupies a volume seven times larger than LATP, and not only can we expect an early onset of percolation, but beyond 13 vol.% LATP, the nanoparticles remain immersed in a continuous interphase making up the rest of the volume. The overall ionic conductivity can then be expressed as

$$\sigma = (1-\phi)\sigma_P + \phi_I\sigma_I + \frac{\phi_N}{(1-\phi)/\sigma_P + \phi_I/\sigma_I + \phi_N/\sigma_N} \qquad \text{Eq. 4-7}$$

The literature values of the polymer and amorphous LATP conductivities are $6.8\cdot10^{-6}$ S·cm^{-1} and $2.46\cdot10^{-5}$ S·cm^{-1}, respectively.[31] The expression in Figure 4 - 8 is plotted in Figure 4 - 7(c) as a function of ϕ_N using these conductivity values, as well as the volume fractions shown in Figure 4 - 7 (b). Finally, the magnitude of σ_I is determined based on a best fit of the expression to

the first three experimental conductivity data points. This yields an estimate for the interphase conductivity of approximately $2.0 \cdot 10^{-4}$ $S \cdot cm^{-1}$, i.e., almost an order of magnitude higher than that of amorphous LATP.

While we do already observe a composite conductivity of $6 \cdot 10^{-5}$ $S \cdot cm^{-1}$ at room temperature for a sample containing 4 vol.% LATP, our analysis suggests that the conductivity should continue to increase until about 13 vol.%, at which point all bulk polymer has been converted to interphase and the volume fraction of the latter, nearly 90%, is at its maximum. The projected ionic conductivity of the system also maximizes at this composition, and is $1.83 \cdot 10^{-4}$ $S \cdot cm^{-1}$ at room temperature, very close to that of pure interphase. Beyond this maximum the conductivity gradually decreases, as an increasing concentration of LATP nanoparticles essentially slows the passage of Li cations. The ideal electrolyte composition would therefore be the one with 13 vol.% LATP, because the interphase exhibits a significantly higher conductivity than this amorphous oxide phase.

The reason why we did not observe a continued increase in conductivity beyond 4 vol.% is because the nanoparticles begin to agglomerate into clusters at higher concentrations. This significantly reduces the ability of the interphase to expand into adjacent bulk polymer, and consequently the interphase volume fraction and conductivity decrease. This is illustrated in Figure 4 - 8(b) and it is also apparent from the SEM images shown in Figure 4 - 2. Nanoparticles are homogenously dispersed at 10 wt.% (4 vol.%), whereas at 15 and 20 wt.% (5.7 and 7.4 vol.%), larger agglomerates form. A similar phenomenon has been

reported with polymer composite electrolyte filled with passive ceramic fillers.[14,53] To achieve better dispersion of nanoparticles at higher loading would require particle surface modification. We chose to defer such an alteration to a future investigation, as the change in interfacial properties may have secondary effects on the interphase development.

Finally, as to the reason why LATP has such a strong influence on the development of an interphase region compared to inert nanoparticles, with lithium, both doped PEO and LATP share a common component. Therefore, for this composite there exists a driving force to balance the chemical potential of lithium between both phases. As a result, we may expect a more significant effect on the structural developments in the polymer when pairing LATP and PEO, possibly even an exchange of lithium between the two.

4.5 Conclusions

The comparative evaluation of the effect of different types of nanoparticles on the lithium ion conductivity of PEO/$LiClO_4$-based nanocomposites shows that amorphous $Li_{1.3}Al_{0.3}Ti_{1.7}(PO_4)_3$ (LATP) nanoparticles, i.e., an active filler with 65±8 nm average particle size that has been synthesized via LF-FSP causes a markedly stronger enhancement of the cation transport than passive fillers such as TiO_2 or fumed silica. To identify the underlying mechanism, samples are analyzed for their degree of crystallinity and glass transition behavior. The lithium salt concentration and polymer chain length has also been varied.

While lithium salt exhibits a plasticizing effect on the polymer, which suppresses crystallization, the disruption it causes in the ability of the network to

reorganize appears to also promote lithium mobility. Moreover, comparable glass transition temperatures and degrees of crystallinity are observed for all filler types, which leads us to conclude that suppressing crystallinity is not the dominant factor for the enhancement in ionic conductivity in these nanocomposites.

A maximum ionic conductivity is achieved at 10 wt.% LATP loading, which corresponds to about 4 vol.%, i.e., a concentration at which percolation via LATP particles involving direct contact is unlikely. Conversely, it is expected that the interfacial region surrounding these particles could easily expand to twice their radius, effectively affecting an eightfold larger volume fraction. The observed maximum in conductivity is then consistent with percolation across the interphase. While the measured value of ionic conductivity already reaches more than twice the magnitude of that of the LATP particles, which is the component with the highest cation mobility, we estimate that the inherent conductivity of the interphase containing one Li cation for every 20 EO groups could be nearly an order of magnitude higher than that of LATP, i.e., 2.0×10^{-4} $S \cdot cm^{-1}$, and that highest system conductivity would occur around 13 vol.% of well-dispersed LATP.

This assessment is based on a simple model for calculating the phase distribution in a three-component system, LATP, polymer, and interphase, and on a corresponding equivalent circuit. The fact that active nanoparticles have a stronger effect than passive ones can be attributed to a more pronounced restructuring within the interphase when polymer and nanoparticles share a

common component, for which the system seeks to establish a balance in chemical potential.

4.6 References

1. M. Armand, 'The history of polymer electrolytes,' *Solid State Ionics* **69**, 309 (1994)

2. J.M. Tarascon & M. Armand, 'Issues and challenges facing rechargeable lithium batteries.,' *Nature* **414**, 359 (2001)

3. J.R. MacCallum & C.A. Vincent, *Polymer Electrolyte Reviews*. Springer Science & Business Media, (1989)

4. P.V. Wright, 'Electrical conductivity in ionic complexes of poly (ethylene oxide),' *British Polymer Journal* **7**, 319 (1975)

5. M. Armand, 'Polymer solid electrolytes-an overview,' *Solid State Ionics* **9**, 745 (1983)

6. M. Watanabe, M. Kanba, H. Matsuda, K. Tsunemi, K. Mizoguchi, E. Tsuchida & I. Shinohara, 'High lithium ionic conductivity of polymeric solid electrolytes,' *Die Makromolekulare Chemie, Rapid Communications* **2**, 741 (1981)

7. F.M. Gray 1991. *Solid Polymer Electrolytes*. VCH New Tork etc.

8. B. Scrosati, F. Croce & L. Persi, 'Impedance spectroscopy study of peo-based nanocomposite polymer electrolytes,' *Journal of The Electrochemical Society* **147**, 1718 (2000)

9. F. Croce, G.B. Appetecchi, L. Persi & B. Scrosati, 'Nanocomposite polymer electrolytes for lithium batteries,' *Nature* **394**, 456 (1998)

10. A.M. Stephan, 'Review on gel polymer electrolytes for lithium batteries,' *European Polymer Journal* **42**, 21 (2006)

11. C.-W. Nan, L. Fan, Y. Lin & Q. Cai, 'Enhanced ionic conductivity of polymer electrolytes containing nanocomposite SiO_2 particles,' *Physical Review Letters* **91**, 266104 (2003)

12. H.M.J.C. Pitawala, M.A.K.L. Dissanayake & V.A. Seneviratne, 'Combined effect of $Al2O3$ nano-fillers and EC plasticizer on ionic conductivity enhancement in the solid polymer electrolyte $(PEO)_9$LiTF,' *Solid State Ionics* **178**, 885 (2007)

13. H.-M. Xiong, X. Zhao & J.-S. Chen, 'New polymer-inorganic nanocomposites: PEO-ZnO and PEO-ZnO-$LiClO_4$ films,' *The Journal of Physical Chemistry B* **105**, 10169 (2001)

14. J. Adebahr, A.S. Best, N. Byrne, P. Jacobsson, D.R. Macfarlane & M. Forsyth, 'Ion transport in polymer electrolytes containing nanoparticulate tio 2: The influence of polymer morphology,' *Physical Chemistry Chemical Physics* **5**, 720 (2003)

15. H.W. Han, W. Liu, J. Zhang & X. Zhao, 'A hybrid poly (ethylene oxide)/poly (vinylidene fluoride)/tio2 nanoparticle solid-state redox electrolyte for dye-sensitized nanocrystalline solar cells,' *Advanced Functional Materials* **15**, 1940 (2005)

16. P. Johansson & P. Jacobsson, 'TiO_2 nano-particles in polymer electrolytes: Surface interactions,' *Solid State Ionics* **170**, 73 (2004)

17. B. Kumar, L.G. Scanlon & R.J. Spry, 'On the origin of conductivity enhancement in polymer-ceramic composite electrolytes,' *Journal of Power Sources* **96**, 337 (2001)

18. S.A. Suthanthiraraj & D.J. Sheeba, 'Structural investigation on peo-based polymer electrolytes dispersed with al2o3 nanoparticles,' *Ionics* **13**, 447 (2007)

19. W. Wieczorek, J.R. Stevens & Z. Florjańczyk, 'Composite polyether based solid electrolytes. The lewis acid-base approach,' *Solid State Ionics* **85**, 67 (1996)

20. B. Kumar & L.G. Scanlon, 'Polymer□ceramic composite electrolytes: Conductivity and thermal history effects,' *Solid State Ionics* **124**, 239 (1999)

21. H.J. Walls, J. Zhou, J.A. Yerian, P.S. Fedkiw, S.A. Khan, M.K. Stowe & G.L. Baker, 'Fumed silica-based composite polymer electrolytes: Synthesis, rheology, and electrochemistry,' *Journal of Power Sources* **89**, 156 (2000)

22. X.W. Zhang, Y. Li, S.A. Khan & P.S. Fedkiw, 'Inhibition of lithium dendrites by fumed silica-based composite electrolytes,' *Journal of The Electrochemical Society* (2004)

23. A.S. Best, J. Adebahr, P. Jacobsson, D.R. Macfarlane & M. Forsyth, 'Microscopic interactions in nanocomposite electrolytes,' *Macromolecules* **34**, 4549 (2001)

24. C.-Y. Chiang, M.J. Reddy & P.P. Chu, 'Nano-tube TiO_2 composite PVDF/lipf 6 solid membranes,' *Solid State Ionics* **175**, 631 (2004)

25. P.P. Chu, M.J. Reddy & H.M. Kao, 'Novel composite polymer electrolyte comprising mesoporous structured SiO_2 and PEO/Li,' *Solid State Ionics* **156**, 141 (2003)

26. M. Wagemaker, G.J. Kearley, A.A. Van Well, H. Mutka & F.M. Mulder, 'Multiple Li positions inside oxygen octahedra in lithiated TiO_2 anatase,' *Journal of the American Chemical Society* **125**, 840 (2003)

27. C.J. Leo, G.V.S. Rao & B.V.R. Chowdari, 'Studies on plasticized peo–lithium triflate–ceramic filler composite electrolyte system,' *Solid State Ionics* **148**, 159 (2002)

28. W. Liu, N. Liu, J. Sun, P.-C. Hsu, Y. Li, H.-W. Lee & Y. Cui, 'Ionic conductivity enhancement of polymer electrolytes with ceramic nanowire fillers,' *Nano Letters* **15**, 2740 (2015)

29. Y.-J. Wang, Y. Pan & L. Chen, 'Ion-conducting polymer electrolyte based on poly (ethylene oxide) complexed with $Li_{1.3}Al_{0.3}Ti_{1.7}(PO_4)_3$ salt,' *Materials Chemistry And Physics* **92**, 354 (2005)

30. B. Kumar & L.G. Scanlon, 'Polymer-ceramic composite electrolytes,' *Journal Of Power Sources* **52**, 261 (1994)

31. H. Chen, H. Tao, Z. Xiujian & W. Qide, 'Fabrication and ionic conductivity of amorphous Li–Al–Ti–PO thin film,' *Journal of the American Chemical Society* **357**, 3267 (2011)

32. E. Yi, W. Wang, J. Kieffer & R.M. Laine, 'Flame made nanoparticles permit processing of dense, flexible, li+ conducting ceramic electrolyte thin films of cubic-$Li_7La_3Zr_2O_{12}$(c-LLZO),' *Journal of Materials Chemistry A* **4**, 12947 (2016)

33. E. Yi, W. Wang, S. Mohanty, J. Kieffer & R. Tamak, 'Materials that can replace liquid electrolytes in li batteries: Superionic conductivities in $Li_{1.7}Al_{0.3}Ti_{1.7}Si_{0.4}P_{2.6}O_{12}$. Processing combustion synthesized nanopowders to free standing thin films,' *Journal of Power Sources* 577 (2014)

34. J.-K. Lee, Y.-J. Lee, W.-S. Chae & Y.-M. Sung, 'Enhanced ionic conductivity in PEO-$LiClO_4$ hybrid electrolytes by structural modification,' *Journal of Electroceramics* **17**, 941 (2006)

35. Y.-J. Wang, Y. Pan & D. Kim, 'Conductivity studies on ceramic li $Li_{1.3}Al_{0.3}Ti_{1.7}(PO_4)_3$-filled peo-based solid composite polymer electrolytes,' *Journal of power sources* **159**, 690 (2006)

36. D. Saikia, H.-Y. Wu, Y.-C. Pan, C.-C. Liao, C.-F. Chen, G.T.K. Fey & H.-M. Kao, 'A highly conductive organic–inorganic hybrid electrolyte based on co-condensation of di-ureasil and ethylene glycol-containing alkoxysilane,' *Electrochimica Acta* **54**, 7156 (2009)

37. M. Kim & R.M. Laine, 'One-step synthesis of core- shell $(Ce_{0.7}Zr_{0.3}O_2)_X$ $(Al_2O_3)_{1-x}$[$(Ce_{0.7}Zr_{0.3}O_2)$@ Al_2O_3] nanopowders via liquid-feed flame spray pyrolysis (lf-fsp),' *Journal of the American Chemical Society* **131**, 9220 (2009)

38. R.M. Laine, J.C. Marchal, H.P. Sun & X.Q. Pan, 'Nano- -Al_2O_3 by liquid-feed flame spray pyrolysis,' *Nature Materials* **5**, 710 (2006)

39. B. Weidenhof, M. Reiser, K. Stowe, W.F. Maier, M. Kim, J. Azurdia, E. Gulari, E. Seker, A. Barks & R.M. Laine, 'High-throughput screening of

nanoparticle catalysts made by flame spray pyrolysis as hydrocarbon/no oxidation catalysts,' *Journal of the American Chemical Society* **131**, 9207 (2009)

40. J.D. Van Heumen & J.R. Stevens, 'The role of lithium salts in the conductivity and phase morphology of a thermoplastic polyurethane,' *Macromolecules* **28**, 4268 (1995)

41. S. Cimmino, E. Di Pace, E. Martuscelli & C. Silvestre, 'Evaluation of the equilibrium melting temperature and structure analysis of poly (ethylene oxide)/poly (methyl methacrylate) blends,' *Die Makromolekulare Chemie* **191**, 2447 (1990)

42. S.K. Fullerton-Shirey & J.K. Maranas, 'Structure and mobility of PEO/LiClO4 solid polymer electrolytes filled with Al_2O_3 nanoparticles,' *The Journal of Physical Chemistry C* **114**, 9196 (2010)

43. J.-H. Ahn, G.X. Wang, H.K. Liu & S.X. Dou, 'Nanoparticle-dispersed peo polymer electrolytes for li batteries,' *Journal of power sources* **119**, 422 (2003)

44. T.M. Ali, N. Padmanathan & S. Selladurai, 'Structural, conductivity, and dielectric characterization of PEO–PEG blend composite polymer electrolyte dispersed with TiO_2 nanoparticles,' *Ionics* **19**, 1115 (2013)

45. F. Deng & K.J.V. Vliet, 'Prediction of elastic properties for polymer–particle nanocomposites exhibiting an interphase,' *Nanotechnology* (2011)

46. L.M. Hamming, R. Qiao, P.B. Messersmith & L.C. Brinson, 'Effects of dispersion and interfacial modification on the macroscale properties of TiO_2 polymer–matrix nanocomposites,' *Composites Science And Technology* **69**, 1880 (2009)

47. M.S. Ozmusul & R.C. Picu, 'Elastic moduli of particulate composites with graded filler matrix interfaces,' *Polymer Composites* **23**, 110 (2002)

48. M.T. Sebastian & H. Jantunen, 'Polymer–ceramic composites of 0–3 connectivity for circuits in electronics: A review,' *International Journal of Applied Ceramic Technology* **7**, 415 (2010)

49. P.A. Tzika, M.C. Boyce & D.M. Parks, 'Micromechanics of deformation in particle-toughened polyamides,' *Journal of the Mechanics and Physics of Solids* **48**, 1893 (2000)

50. H.T. Vo & F.G. Shi, 'Towards model-based engineering of optoelectronic packaging materials: Dielectric constant modeling,' *Microelectronics Journal* **33**, 409 (2002)

51. R. Qiao, H. Deng, K.W. Putz & L.C. Brinson, 'Effect of particle agglomeration and interphase on the glass transition temperature of polymer nanocomposites,' *Journal of Polymer Science Part B: Polymer Physics* **49**, 740 (2011)

52. M. Avrami, ‘Kinetics of phase change I - general theory,’ *Journal Of Chemical Physics* **7**, 1103 (1939)

53. N. Byrne, J. Efthimiadis, D.R. Macfarlane & M. Forsyth, ‘The enhancement of lithium ion dissociation in polyelectrolyte gels on the addition of ceramic nano-fillers,’ *Journal Of Materials Chemistry* **14**, 127 (2004)

CHAPTER 5

STRUCTURAL UNITS AND STRUCTURE PROPERTY RELATIONSHIP FOR MIXED NETWORK FORMER GLASS ELECTROLYTES

5.1 Introduction

Sodium ion containing glasses have attracted increasing attention because of their potential applications in photonics, opto-electronics, and to replace liquid electrolytes in sodium-based batteries.[1, 2] Therefore, their physical properties as well as the relationships that connect their compositions and their atomic level structures to their physical properties are important to better understand the origin of the specific materials responses and develop materials design criteria. Among these, elastic properties are of particular interest, not only because knowledge of elastic constants is necessary for materials selection in accordance with application specifications, but also because elastic moduli are understood to be a fundamental characteristic that is closely related to materials structure. The elastic response of materials originates from the interatomic forces and therefore is a measure of the bonding topology and of the overall structural integrity in the glassy network. Moreover, the elastic behavior of a glass can affect other

phenomena, such as the transport of heat and matter. At low to moderate temperatures, the majority of thermal transport occurs via phonon propagation. The stiffer the glass network, the higher the velocity of sound, and the greater the thermal conductivity. The network elastic response also affects the migration rate of mobile ions. The activation barrier for ion hopping is to a large part associated with the work required for this ion to bypass structural obstacles during its passage from one stable site to another, while the remaining part can be attributed to the energy change the migrating cation experiences when displaced within the electric field created by the net charges of the equilibrium cation sites. There has been considerable debate about the relative magnitudes of these two contributions to the overall activations energy barrier. During the cation jump the surrounding of this mobile ion is subject to an elastic strain field change.[3, 4] A highly cross-linked and stiff network is less likely to provide the compliance necessary for a facile passage of migrating cations. Therefore, an in-depth understanding of elastic properties in glasses at a molecular structural level is helpful in developing glassy ion conductors.

Mixed network former (MNF) glasses exhibit some interesting features such as non-linear and non-additive changes in properties with varying network former (NF) proportions. These glasses provide a system in which the cation concentration can be kept constant while local structural changes due to compositional changes between two binary network forming systems. In this way, structure-property relationships can be investigated over a wide range, as structural changes are significant when replacing one NF species with another.

In this study, we investigate the elastic properties of two mixed network-former systems: $0.2Na_2O + 0.8[xBO_{1.5} + (1\text{-}x)SiO_2]$ (NBS) and $0.2Na_2O + 0.8[xBO_{1.5} + (1–x)GeO_2]$ (NBG). Upon increasing *x*, one formula unit of borate replaces two silica units, so as to maintain a constant balance of network cations.

The elastic properties of glasses are affected by many factors, including interatomic bonding energy, packing density, coordination and molecular organization.[5] Many researchers report that elastic moduli in binary alkali borate glasses strongly correlate with boron coordination.[6–9] Structures that favor the formation of tetrahedrally coordinated boron have higher elastic moduli.[10, 11] For binary silicates, the concentration of bridging oxygens (BO) per glass-forming cation, silicon, which provides a measure of the degree of network crosslinking, as well as the packing density are found to directly influence the elastic moduli.[5,12] In MNF, different coordination can occur for different NFs. Moreover, the way that the additional possible NF paring via BO affects the intermediate range order (IRO). These make the structures of MNF glasses complicated. The relative proportions of differently coordinated NF cations, which constitute the basic materials building blocks in terms of structure and mechanical integrity, are expected to play an important role in the overall structure-property relationships of these glasses. The mixing of NF cations can therefore be considered one of the key materials design parameters for controlling the structure and properties of these glasses. In this study, we focus on using the fraction of short-range order (SRO) structure units to understand the origin of the non-linear and non-additive elastic properties in MNF glasses.

Nuclear magnetic resonance (NMR) spectroscopy is a commonly used characterization method to determine the SRO in glasses. Extensive studies have been carried out to determine coordination at boron.[13–17] However, the SRO of germanium species is extremely hard to quantitatively analyze. The only NMR active isotope (^{73}Ge) suffers from unfavorable NMR characteristics, which makes it impossible to study.[18, 19] In this study, we use a combination of experimental NMR data, adiabatic elastic constants, and a reaction equilibrium model to characterize the SRO in MNF glasses.

5.2 Experimental

5.2.1 Sample Preparation

The NBS samples were prepared by Corning Inc. using reagent grade chemicals, which were turbula-mixed and calcined. The calcined mixtures were melted at 1450^{o}C in platinum crucibles for 6 hours. Melts were poured out and rolled into thin sheets, then ground into cullet. The cullet from each sample was re-melted at a temperature between 1200 – 1550^{o}C, depending on composition. The melts were then poured into bars and annealed for 1 hour at 550^{o}C. Samples were then cut, ground, and polished into 30 x 30 x 1mm, plane-parallel squares. Compositional analysis by Corning of Na, B Si, and O all showed that the compositions in terms of Na_2O, SiO_2 and $BO_{3/2}$ were all within ±2 wt % of target compositions.

The NBG glasses were prepared at Coe College using stoichiometric amounts of Na_2CO_3 (99.97%), H_3BO_3 (99.5%), and GeO_2 (99.5%). All

compounds were obtained from Sigma Aldrich. The mixtures were heated in platinum crucibles after being thoroughly mixed together. The samples were melted between 1000-1200 ^{o}C for 30 minutes with a weight loss measurement taken midway. All melts showed consistent weight loss of water and carbon dioxide. Samples for density were plate quenched and the resulting glassy shards were used in the pycnometer. For ^{11}B MAS NMR and Brillouin light scattering the glasses were annealed at 50 ^{o}C below T_g for one hour and then cooled at 5 ^{o}C/min until removed from the furnace at 80^{o}C. The BLS glasses were made into 25 mm x 1-3 mm polished discs.

5.2.2 Density

Densities of 0.2 Na_2O + 0.8 [$xBO_{1.5}$ + (1-x) SiO_2] glasses were determined using the Archimedes method on bulk glass samples using paraffin oil (Fisher Scientific) as the suspension liquid (ρ = 0.848 ± 0.005 g/cm^3). Reproducibility tests showed that the densities are typically accurate to ± 0.02 g/cm^3.

Densities of the corresponding sodium borogermanate glasses were measured using a Quantachrome Ultrapycnometer 1000, using helium as the working gas, and an analytical balance. Multiple volume measurements were taken and averaged to ensure accurate and reproducible results. High purity aluminum was used as a calibration density material. The densities of the sodium borogermanate glasses are accurate to ± 0.01 g/cm^3.

5.2.3 Nuclear Magnetic Resonance

Single pulse ^{11}B Magic Angle Spin Nuclear Magnetic Resonance (MAS-NMR) spectra were obtained using a Bruker AV-600 Spectrometer on fine

ground powdered samples contained in a 4 mm zirconia probe spinning at 10 or, in most cases, 12 kHz. ^{11}B MAS-NMR spectra were recorded at 192.55 MHz using a 25^{o} tipping angle of 1 μs, a delay of 3s, and 40 scans. The tipping angle of the ^{11}B spectra was determined by finding the pulse length where the resulting area under the curve of trigonal to tetrahedral peaks were equal in borax, ($Na_2B_4O_710H_2O$, Fisher Scientific, 99.5%). Chemical shifts were reported relative to BF_2-Et_2O, $\delta_{cs} = 0\ ppm$.

5.2.4 Brillouin Light Scattering

Brillouin light scattering (BLS) was used to measure the elastic properties of the glasses. For our measurements a Coherent Verdi solid-state laser with a wavelength of 532 nm was used to illuminate the samples at incident powers of less than 40 mW. The spectrum of scattered light is analyzed using a Sandercock six-pass tandem Fabry-Pérot interferometer. In our experimental setup we establish the platelet geometry where the incident light enters and the scattered light exits the sample through parallel faces, and the sample plane bisects the angle formed by the incident and scattered light directions. For this geometry, one can take advantage of Snell's law to cancel out the refractive index in the scattering equation. The phonon wavevector can be derived from the scattering geometry according to

$$q = 2sin\alpha/\lambda_0 \qquad \text{Eq. 5-1}$$

where $\lambda_0$is the wavelength of the incident light and the α is the angle between the incident light and the plane normal of the sample. From this the sound velocity is calculated as

$$c = \frac{\omega}{q} = \frac{\omega\lambda_0}{2\sin\alpha}$$

Eq. 5-2

The elastic storage modulus is derived from the density of the sample and the sound velocity. In our experiments, both longitudinal and transverse acoustic modes are detected. The longitudinal (*M*) and shear (*G*) modulus are derived from the frequency shifts associated with the longitudinal and transverse peaks in the Brillouin spectra, ω_L and ω_T, according to

$$M(\omega) = \rho_0 c_L^2 = \rho_0 \frac{\omega_L^2}{q^2}$$

Eq. 5-3

$$G(\omega) = \rho_0 c_T^2 = \rho_0 \frac{\omega_T^2}{q^2}$$

Eq. 5-4

where c_L and c_T are the longitudinal and transverse sound velocities, respectively, and ρ_0 is the density of the sample.

5.3 Results and Discussion

In the following we analyze the behavior of the elastic moduli for the two families of glasses, and compare them with quantities reflective of the prevalent structural entities and bonding-topological elements. To this end, we first summarize what is known about the structure of these glasses. Specifically, we endeavor to assess the degree of connectivity within the MNF glasses, as this bears a direct relationship to the mechanical stiffness of the glasses and it also affects migration pathways and the spatial configuration of modifier cation (e.g., Na^+) sites. For these two series of glasses, containing 20% modifier oxide, the possible network units are: silicon coordinated by four oxygens, germanium coordinated by four or six oxygens, and boron coordinated by three or by four

oxygens. The oxygen can be either bridging or non-bridging. BO atoms are shared between two network cations, whereas non-bridging oxygens (NBO) are bonded to only one network cation. In the following, the coordination of a network cation by BO is designated using the corresponding number in parenthesis as a superscript. This number corresponds to that in subscript of the Q_n notation used in NMR spectroscopy analysis. We specify the proportion of BO and NBO in the subscript of the oxygen symbol. For example, $M^{(a)}O_{a/2+b}$ refers to network cation *M* that is coordinated by *a*+*b* total oxygen atoms of which *a* are BO and *b* NBO. Dividing the number of BO in the subscript of the O symbol by two indicates that they are shared between two cations.

The concentrations of several network species in the glasses investigated here are known from NMR analysis, others can be inferred based on molar balances, the condition of charge neutrality, and thermodynamic equilibria that describe the incorporation of BO and NBO in the network. In the following we establish the complete set of reaction equations that account for the displacement of oxygen species from one grouping towards another. It is important to note that the equilibria associated with these reactions do not reflect a dynamic process as in the traditional solution chemistry sense, but represent the statistical sampling of processes that occurred when the systems were in the molten state and became by and large arrested when they crossed through the glass transition.

The reaction equations for the borogermanate systems are established first, as these involve a larger set of species. The equations for the NBS system can

be simply obtained by replacing the Ge symbol with Si, but reactions involving octahedrally coordinated silicon can be omitted, as this species has not been found experimentally. Assuming that Na_2O dissociates fully in solution, the modifier cation can be ignored from the molar balances. In the sodium borate system we observe the formation of NBO

Eq. 5-5 $$B^{(3)}O_{3/2} + \frac{1}{2}O^{2-} \rightarrow B^{(2)}O^{-}_{2/2+1} \quad K_{B1},$$

as well as four-fold coordinated boron

Eq. 5-6 $$B^{(3)}O_{3/2} + \frac{1}{2}O^{2-} \rightarrow B^{(4)}O^{-}_{4/2} \quad K_{B2},$$

where all oxygens are bridging but the $B^{(4)}O^{-}_{4/2}$ grouping carries an excess of one negative unit charge. Combining reactions Eq. 5-5 and Eq. 5-6, the free oxygen can be eliminated to yield the balance between the two modified boron species,

Eq. 5-7 $$B^{(2)}O^{-}_{2/2+1} \rightarrow B^{(4)}O^{-}_{4/2}, \qquad K_B = \frac{K_{B2}}{K_{B1}} = \frac{[B^{(4)}]}{[B^{(2)}]}$$

where the square brackets represent the molar fractions of the species. This formulation of the law of mass action is based on the assumption that the degree of connectivity of the different network former cations is dictated by random chance. This assumption is not in conflict with the well-known non-ideal mixing behavior of the underlying oxide constituents, because the coordination of a given network cation by BO is not predicated by the nature of the network cations that share each of these BO. In other words, the assumption of random chance coordination does not interfere with thermodynamic driving forces that would favor or disfavor particular spatial groupings of network cations due to their

chemical affinity or lack thereof. The equilibria of these reactions are controlled by corresponding Gibbs free energy differences, and while their magnitudes are largely unknown, the equilibrium constants can be inferred from known concentrations. Similarly, for sodium germanates the formation of NBO is described by

Eq. 5-8 $$Ge^{(4)}O_{4/2} + \frac{1}{2}O^{2-} \rightarrow Ge^{(3)}O^{-}_{3/2+1} \qquad K_{G1},$$

and that of octahedrally coordinated germanium by

Eq. 5-9 $$Ge^{(4)}O_{4/2} + O^{2-} \rightarrow Ge^{(6)}O^{2-}_{6/2} \qquad K_{G2}.$$

Again, free oxygen can eliminated between the last two equations to obtain

Eq. 5-10 $$2Ge^{(3)}O^{-}_{3/2+1} \rightarrow Ge^{(4)}O_{4/2} + Ge^{(6)}O^{2-}_{6/2}, \quad K_G = \frac{K_{G2}}{K_{G1}^2} = \frac{[Ge^{(6)}][Ge^{(4)}]}{[Ge^{(3)}]^2}$$

Finally, for sodium silicates only the balance between $Si^{(4)}$ and $Si^{(3)}$ species needs to be considered, which is accounted for in the reaction

Eq. 5-11 $$Si^{(4)}O_{4/2} + \frac{1}{2}O^{2-} \rightarrow Si^{(3)}O^{-}_{3/2+1}, \qquad K_{S1}.$$

In the ternary NBS and NBG glass systems, where network building bocks include all boron and all germanium (respectively silicon) species, the above reaction equations can be combined accordingly. For example, for the NBG glasses, subtracting Eq. 5-7 from Eq. 5-10 yields

Eq. 5-12 $$B^{(4)}O^{-}_{4/2} + 2Ge^{(3)}O^{-}_{3/2+1} \rightarrow B^{(2)}O^{-}_{2/2+1} + Ge^{(4)}O_{4/2} + Ge^{(6)}O^{2-}_{6/2}$$

$$K_{TG} = \frac{K_G}{K_B} = \frac{[B^{(2)}][Ge^{(6)}][Ge^{(4)}]}{[B^{(4)}][Ge^{(3)}]^2}$$

Note that all network species in the ternary system are accounted for in Eq. 5-12, except for $B^{(3)}$, the concentration of which can be obtained using either of Eq. 5-5 or Eq. 5-6, or by using one of the additional constraints introduced below. For the borosilicates it is most convenient to eliminate free oxygen by subtracting Eq. 5-6 from Eq. 5-11 to yield

Eq. 5-13 $$Si^{(4)}O_{4/2} + B^{(4)}O^{-}_{4/2} \rightarrow Si^{(3)}O^{-}_{3/2+1} + B^{(3)}O_{3/2}$$

$$K_{TS} = \frac{K_{S1}}{K_{B2}} = \frac{[Si^{(3)}][B^{(3)}]}{[B^{(4)}][Si^{(4)}]}$$

Additional constraints result from the molar balances, i.e.,

Eq. 5-14 $$[B^{(2)}]+[B^{(3)}]+[B^{(4)}] = x\,,$$

which applies to both germanates and silicates, and

Eq. 5-15 (a) $$[Ge^{(3)}]+[Ge^{(4)}]+[Ge^{(6)}] = (1-x)\,,$$

for germanates, or

Eq. 5-15 (b) $$[Si^{(3)}]+[Si^{(4)}] = (1-x)$$

for silicates. Furthermore, the requirement for charge neutrality in germanates is expressed as

Eq. 5-16 (a) $$[B^{(2)}]+[Ge^{(3)}]+[B^{(4)}]+2[Ge^{(6)}] = [Na]\,,$$

and in silicates as

Eq. 5-16 (b) $$[B^{(2)}]+[Si^{(3)}]+[B^{(4)}] = [Na]\,.$$

The concentrations of these various species of both MNF glass systems are now discussed as a function of the borate mole fraction, *x*. The corresponding data are shown in Figure 5 - 1. For the NBS glasses, the concentrations of two boron

species, $B^{(3)}$ and $B^{(4)}$ have been determined using NMR spectroscopy, while those of the remaining three species, $B^{(2)}$, $Si^{(3)}$ and $Si^{(4)}$, have been inferred with the help of Eq. 5-14, Eq. 5-15(b), Eq. 5-16(b). The results are shown as symbols in Figure 5 - 1(a). This data represents the complete set of information from which structural details of the NBS glasses can be deduced. For example, for both boron and silicon, the concentration of species coordinated by four BO exceed those coordinated by three BO, attesting to a strongly networked structure. Below, this data is collapsed onto a unique descriptor characterizing this degree of networking.

Since in the case of NBS glasses the mole fractions of all species are known from measurement and molar and charge balance constraints, this system provides an excellent test bed for benchmarking the accuracy with which such quantitative speciation can be derived from the chemical reaction equilibrium that led to Eq. 5-13. To this end, to Eq. 5-13 is rewritten as

Eq. 5-13' $$[B^{(4)}][Si^{(4)}]K_{TS} = [Si^{(3)}][B^{(3)}],$$

and two of the species concentrations are eliminated using Eq. 5-14,

Eq. 5-17 $$[B^{(3)}] = x - [B^{(4)}]\left(1 + 1/K_B\right)$$

and Eq. 5-16(b)

Eq. 5-18 $$[B^{(4)}] = \left([Na] - [Si^{(3)}]\right)\left(1 + 1/K_B\right)^{-1}$$

In the latter two expressions Eq. 5-7 is also used to eliminate $[B^{(2)}]$. Substituting in to Eq. 5-13' yields

Eq. 5-19 $$\left([Na] - [Si^{(3)}]\right)\left(1 + 1/K_B\right)^{-1}\left(\left(1 - x\right) - [Si^{(3)}]\right)K_{TS} = [Si^{(3)}]\left(x - [B^{(4)}]\left(1 + 1/K_B\right)\right)$$

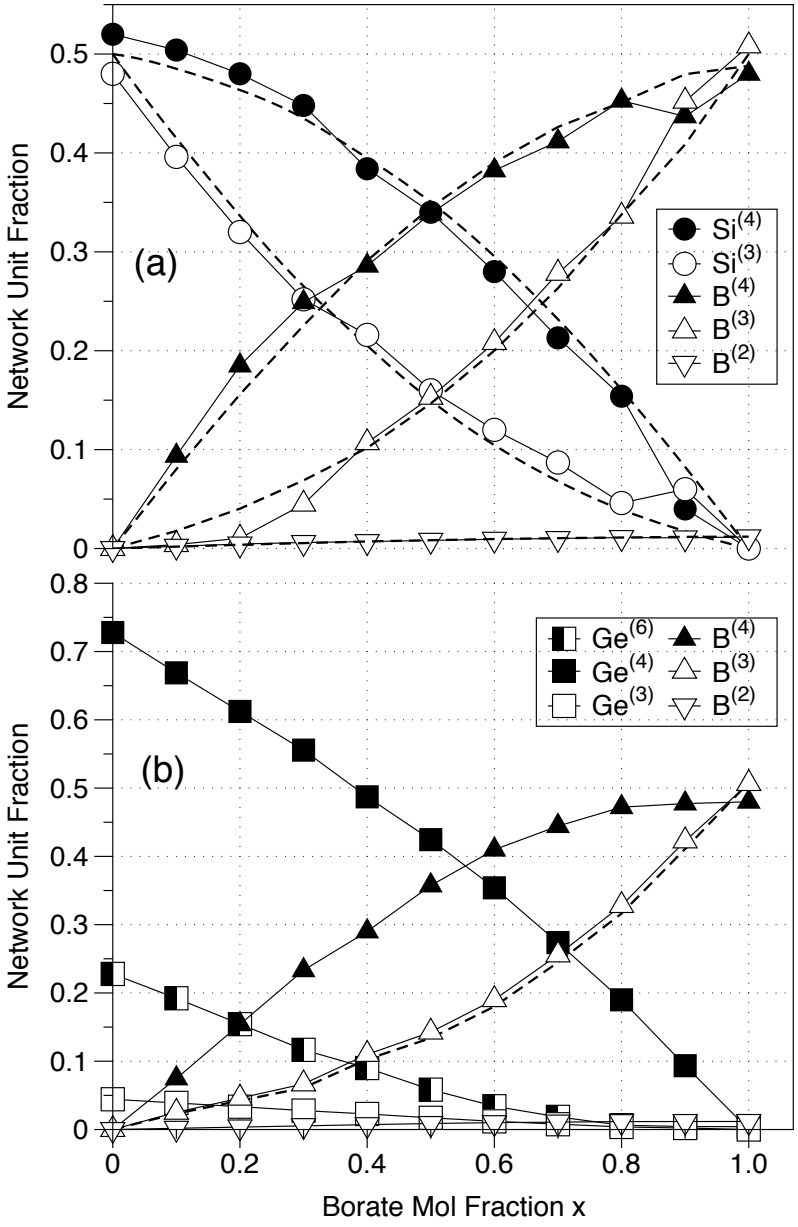

Figure 5 - 1 Molar fractions of $B^{(n)}$, $Si^{(n)}$, and $Ge^{(n)}$ network units as a function of the glass composition, *x*, (a) for sodium borosilicates, and (b) for sodium borogermanates. The fractions of $B^{(3)}$ and $B^{(4)}$ have been determined experimentally, the mole fractions of $Si^{(3)}$, $Si^{(4)}$, and $B^{(2)}$ are calculated from the measured values using molar and charge balances (see text). The dashed lines in (a) and (b), as well as the mole fractions of all germanium species, shown as square symbols, represent best-fit results using the equilibrium models described in the text.

and after rearranging, results in a polynomial of the second degree,

Eq. 5-20 (a) $$[Si^{(3)}]^2 + [Si^{(3)}]\left\{\left([B^{(4)}]\left(1+1/K_B\right)-x\right)\left(1+1/K_B\right)K_{TS}^{-1} - \left([Na]+1-x\right)\right\} + [Na]\left(1-x\right) = 0$$

The smaller of the roots of this polynomial represents the concentration of $Si^{(3)}$. The concentration of $Si^{(4)}$ is then inferred using Eq. 5-15(b). Hence, based on the knowledge of $[B^{(4)}]$ and the equilibrium constants K_B and K_{TS}, the concentrations of all silicon species can be calculated. A value of K_B = 40.66, is derived from the known concentrations of $B^{(2)}$ and $B^{(4)}$ in the binary alkali borate glass, as indicated by Eq. 5-7. The value of K_{TS} is more difficult to determine experimentally. It would require the knowledge of the equilibrium constants of reactions Eq. 5-6 and Eq. 5-11, which occur in two independent binary glass systems. The molar fractions of $B^{(3)}$ and $B^{(4)}$, as well as $Si^{(3)}$ and $Si^{(4)}$ in their respective binary compositions, are all very close to 0.5. Hence, the value of K_{TS} is essentially controlled by the ratio of the free oxygen concentrations in the binary alkali borates and alkali silicates, respectively, which are exceedingly small and therefore difficult to measure. Based on the electronegativity differences between boron and silicon, we can expect that the magnitude of K_{TS} is smaller than 1.

To demonstrate the trustworthiness of our equilibrium model, we now use it to derive the concentration of the silicon species while hypothesizing that the concentration of only one boron species, i.e., $B^{(4)}$, is known from measurement, in which case the straightforward molar and charge balances no longer suffice to calculate the mole fractions of the rest of the species present. We allow for one exception, namely the binary alkali borate glass, where we need the knowledge

of both the concentrations of $B^{(2)}$ and $B^{(4)}$ to determine the value of K_B. Essentially, we then employ the known $B^{(4)}$ species data to identify the optimal value for K_{TS}. To this end we also need the complementary expression to Eq. 5-21(a), which allows us to solve the equilibrium expressed by Eq. 5-13 for $[B^{(4)}]$. Substituting again Eq. 5-17 and Eq. 5-16(b) solved for $[Si^{(3)}] = [Na] - [B^{(4)}]\left(1 + 1/K_B\right)$ into Eq. 5-13' yields after similar rearrangements another second degree polynomial, this time in $[B^{(4)}]$,

Eq. 5-21 (b)

$$[B^{(4)}]^2\left(1+1/K_B\right)^2 - [B^{(4)}]\left(\left(1-x-[Si^{(3)}]\right)K_{TS} + \left([Na]+x\right)\left(1+1/K_B\right)\right) + [Na]x = 0\ .$$

In the final expression of Eq. 5-21 (b) we also used the equality $[Si^{(4)}] = 1 - x - [Si^{(3)}]$ derived from Eq. 5-15(b). The iterative procedure to determine the desired silicon species concentrations then alternates between solving Eq. 5-21 (a) and solving Eq. 5-21 (b) as follows: First an arbitrary value for K_{TS} is chosen, say 1.0, and then Eq. 5-21 (a) is solved for every *x*-value for which the concentration of the boron species is known. This yields an initial set of $[Si^{(3)}]$ values as a function *x*. Next, we search for an improved value of K_{TS} by solving Eq. 5-21(b) using the initial set of $[Si^{(3)}]$ repeatedly, progressing according to a non-linear least square fit algorithm until the error $\sum_i \left([B^{(4)}]_{\text{exp.}} - [B^{(4)}]_{\text{calc.}}\right)^2$ is minimized for a given this set of $[Si^{(3)}]$. The new value for K_{TS} is then used to solve for a new set of $[Si^{(3)}]$, as in step 1, based on a single evaluation of Eq. 5-21 (a). These iterations are continued until the value for K_{TS} has converged, which in the present case yields K_{TS} = 0.18. The resulting best-fit values for $[Si^{(3)}]$

and $[B^{(4)}]$ are shown as dashed lines in Fig. 1(a). For completeness sake, we also show the $[Si^{(4)}]$, $[B^{(2)}]$, and $[B^{(3)}]$ values calculated from these best-fit data using Eqs. (14), (15b) and (16b), and are shown as dashed lines. The agreement between experimental data and the curves derived from the reaction model is well within measurement uncertainties, especially considering that the model assumes a single equilibrium constant across the entire composition range. For these reasons, the reaction-based model a viable approach for predicting network species concentrations in MNF glasses.

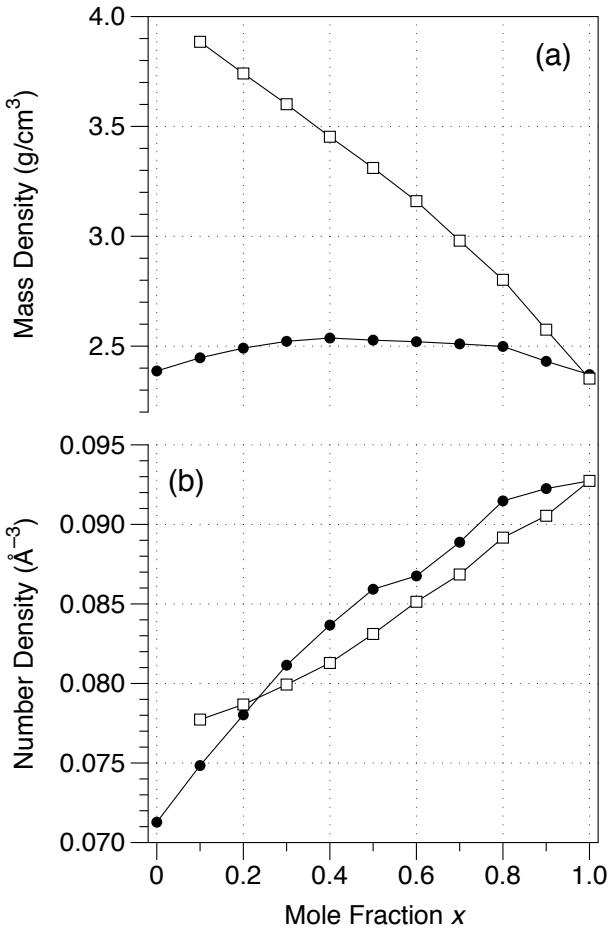

Figure 5 - 2 (a) Density for sodium borosilicate and sodium borogermanate glasses; (b) number density for sodium borosilicate and sodium borogermanate glasses.

A heightened challenge is presented by the NBG glasses, where the boron speciation is known from NMR experiments, but the germanium speciation is unknown. Before discussing the SRO in NBG glasses, let us carry the analysis of NBS glasses one step further, to demonstrate a strong correlation between the elastic properties of these glasses and the density of highly connected network building blocks. Although the principal design parameter for the two MNF glass series is the relative proportion of the two NFs, as expressed by the variable *x*, other quantities prove more useful in the present context. For example, it is generally understood that the elastic modulus is related to density at a fundamental level in that it provides a measure of the number of SRO structural units per unit volume capable of bearing load. The mass density is plotted in Figure 5 - 2(a) as a function of *x* for the two MNF glass systems. Notice that for the NBS system, the density exhibits a maximum as a function of *x*, which introduces the potential for ambiguity. Conversely, the number density, i.e., the inverse of the molar volume of the glass, which is calculated by dividing the density by the molar mass, or equivalently, by dividing the number of atoms per formula unit by the molar volume, varies monotonously as a function of *x* for both systems (Figure 5 - 2(b)). By eliminating the atomic mass, the number density reveals the packing efficiency within the structure even more so than the mass density. Despite the decrease in the total number of atoms per formula unit as a function of *x*, the number density increases with *x* upon replacing SiO_2 or GeO_2 with $BO_{1.5}$ for both glass systems, due to more densely packed structures at larger *x*. The number density for NBS glass varies from 0.0713 $Å^{-3}$ to 0.0927 $Å^{-3}$

and that for the NBG series varies from 0.0765 $Å^{-3}$ to 0.091.5 $Å^{-3}$, with the absence of a sample at $x = 0$.

In Figure 5 - 3 the longitudinal, Young's, bulk, and shear elastic moduli of the two glass systems are shown as a function of the mole fraction, the mass density, and the number density. While the longitudinal and shear moduli are measured directly using BLS, as per Eq. 5-3 and Eq. 5-4, the Young's modulus, *E*, and the bulk modulus, *K*, are readily calculated from the longitudinal and shear moduli according to

$$E = \frac{G\left(3M - 4G\right)}{M - G} \qquad \text{Eq. 5-21}$$

$$K = M - \frac{4G}{3} \qquad \text{Eq. 5-22}$$

In almost all cases, the elastic moduli exhibit a maximum as a function of *x*. For the NBS glasses, the longitudinal, Young's, and the shear modulus peak at x=0.4, and the bulk modulus at x=0.6. For the NBG glasses, the longitudinal, shear and Young's modulus reach a maximum at x = 0.4 while the bulk modulus decreases monotonously with *x*, yet exhibiting a weak curvature that echoes the behaviors of the other moduli. The change in modulus with *x* for the NBG series is smaller than for the NBS glass series. Notice that in both cases, the trend for the bulk modulus is slightly different than that for any of the other moduli. The data plotted in Figure 5 - 3(b) reveals a very steep increase and decrease of the moduli with mass density for sodium borosilicates. In fact, the trend in the data doubles back on itself sharply, which demonstrates the ambiguity that can result from using mass density as a means to relate properties to structure. Figure 5 - 3

(c), on the other hand, shows a continuously progressing dependence of the moduli on the number density. The data shows similar trends to those in Figure 5 - 3 (a), but it reveals that the packing effectiveness in silicates spans a wider range than in germanates. Note that the data for the binary sodium germanate glass is not available for characterization, and the corresponding data points are missing.

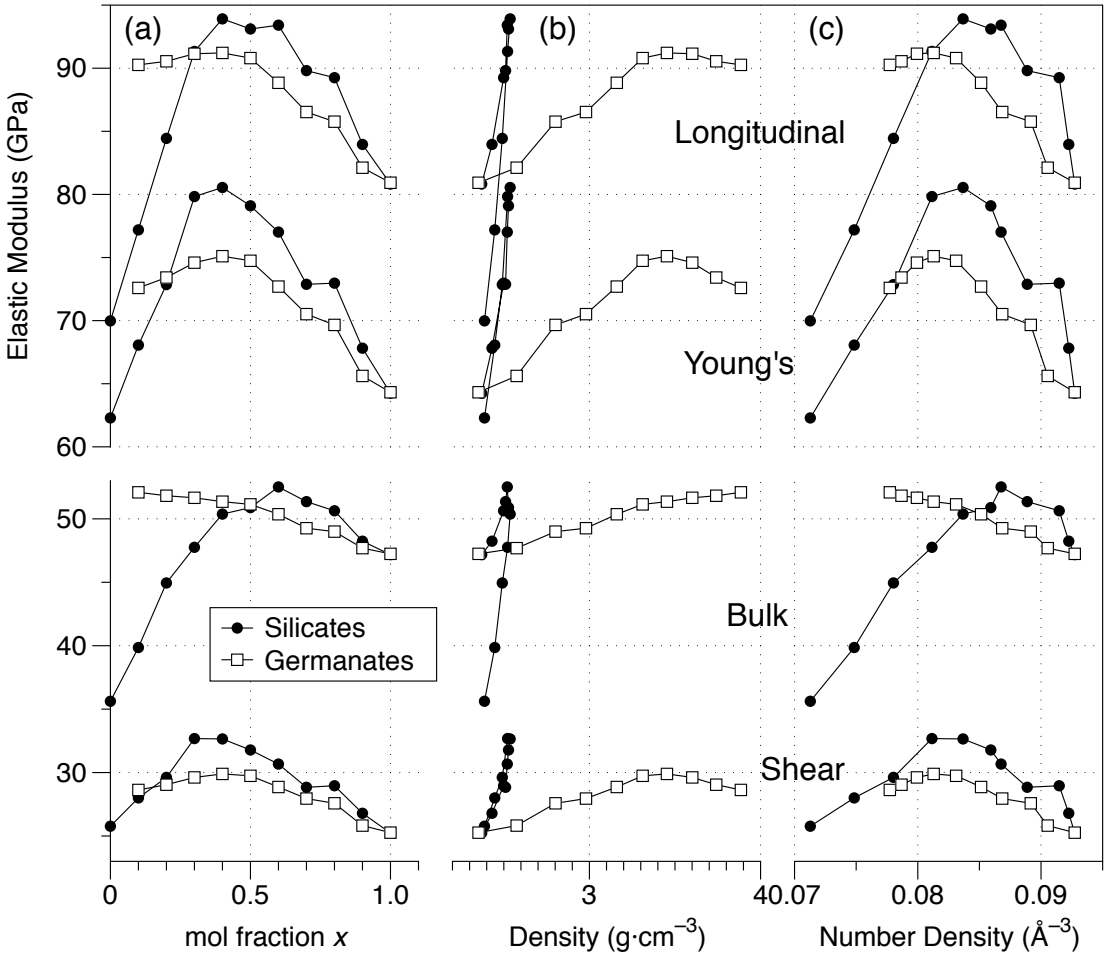

Figure 5 - 3 Longitudinal, Young's, bulk, and shear elastic moduli of the two sodium borosilicate and sodium borogermanate glass systems, (a) as a function of the borate mole fraction, (b) as a function of the mass density, and (c) as a function of the atomistic number density.

The number density, in atoms per unit volume, is a measure of how densely the atoms reside in a structure, and by inference, how effectively load is transferred between SRO structural units. Accordingly, it is generally accepted that the materials are stiffer and the elastic moduli are higher when the various SRO units are packed more densely.[11, 21] As a result, the elasticity of materials increases with their packing density.[22, 23] However, while in these two series of glasses, both longitudinal and shear modulus exhibit an initial increase, they reach a maximum followed by a decrease as a function of number density. The negative correlation between the elastic moduli on the number density on the right side of Figure 5 - 3(c) suggests a more intricate relationship between structural stiffness and packing density. Anomalous behaviors of the elastic modulus as a function of density have been reported earlier by one of the co-authors.[24, 25] In this earlier study the density change was induced by changing the pressure to which the glass structure is subjected, and a detailed analysis showed that the behavior can be explained as due to a progressive reconfiguration of the BO topology as a result of localized buckling transitions. In the present case structural changes are not effected by externally applied pressure but by changes in chemical composition, in particular, by varying the ratio of the two NFs.

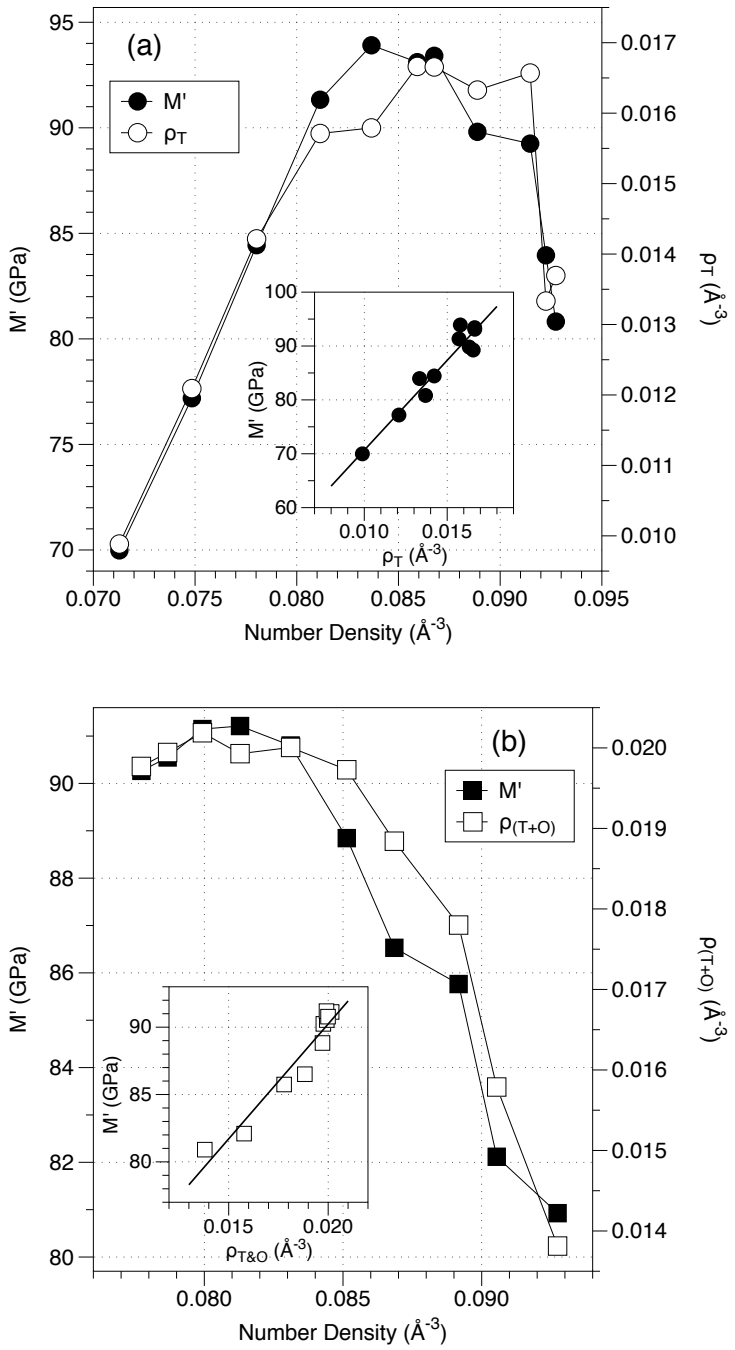

Figure 5 - 4 Longitudinal elastic modulus and combined tetrahedral and octahedral network unit number density as a function of the atomic number density, $\rho_{T\&O}$: (a) of sodium borosilicates, and (b) of sodium borogermanates. Inset: M plotted vs. $\rho_{T\&O}$ to establish the scaling factor between the two ordinate axes.

Next, the concept of number density is further refined so as to characterize the mechanical stiffness of the network structure in a more targeted fashion. For a network to be rigid to the effect of providing restoring forces to both shear and longitudinal deformations, units must be connected in all three spatial dimensions. This includes those NF cations that are connected to their neighbors via four or more BO, i.e., tetrahedrally and octahedrally coordinated elements. In Figure 5 - 4(a) the number density of tetrahedrally and octahedrally coordinated network cations, $\rho_{T\&O}$, is compared with the longitudinal modulus for the NBS glasses. The two data sets track one another very well. The longitudinal modulus is chosen to make this comparison, because it reflects the resistance to both shear and isotropic deformations. Given that the two quantities possess different physical dimensions, the comparison in Figure 5 - 4 requires scaling of one of the variables. The scaling factor is derived from the linear fit shown in the inset of the figure, where M is plotted vs. $\rho_{T\&O}$. For the NBS system the best fit of the data is achieved for $M = 37.3+3334\cdot\rho_T$, with a correlation of 0.96. Note that the linear fit is primarily used to establish scaling in a consistent way; a good linear fit does not imply that the two quantities indeed track each other, as this construct does not account for the maximum in the data. Nonetheless, the analysis shown in Figure 5 - 4 reveals that the longitudinal modulus is directly proportional to ρ_T within a narrow confidence band, and it is therefore considered to be a key descriptive parameter for relating structure to elastic properties.

With this information in mind, let us return to the characterization of the SRO in NBG glasses. Here again, the mol-fractions of two boron species are

known from NMR spectroscopy for the entire composition range, inferring the third using Eq. 5-14. However, none of the Ge species concentrations have been measured, and since there are three possible Ge species, the molar balance and charge neutrality requirement do not suffice to derive their concentrations. Here it is necessary to use our chemical equilibrium model to gain further insight. Restructuring Eq. Eq. 5-16 (a) yields

Eq. 5-23 $$[Ge^{(6)}] = \frac{1}{2}\left([Na] - [B^{(2)}] - [B^{(4)}]\right) - \frac{1}{2}[Ge^{(3)}] = A - \frac{1}{2}[Ge^{(3)}],$$

where *A* represents a grouping of all known quantities. Furthermore, the expression for the equilibrium constant of Eq. 5-12 can be rewritten as

Eq. 5-24 $$K' = K_{TG}\frac{[B^{(4)}]}{[B^{(2)}]} = \frac{[Ge^{(6)}][Ge^{(4)}]}{[Ge^{(3)}]^2} \Leftrightarrow [Ge^{(3)}]^2 K' = [Ge^{(6)}][Ge^{(4)}]$$

Substituting Eq. 5-15 (a) , solved for the concentration of $Ge^{(4)}$, and Eq. 5-24 in this expression yields

Eq. 5-25 $$[Ge^{(3)}]^2 K' = \left(A - \frac{1}{2}[Ge^{(3)}]\right)\left(1 - x - A - \frac{1}{2}[Ge^{(3)}]\right)$$

which after expanding and regrouping yields a polynomial of the second degree,

Eq. 5-26 $$\left(K' - \frac{1}{4}\right)[Ge^{(3)}]^2 + \frac{1}{2}[Ge^{(3)}]\left(1 - x\right) + A\left(A + x - 1\right) = 0$$

The positive roots of this polynomial provide the concentrations of $Ge^{(3)}$ as a function of the composition. The concentrations for $Ge^{(6)}$ and $Ge^{(4)}$ can then be calculated using Eq. 5-23 and Eq. 5-15(a), respectively. The only remaining unknown that needs to be determined before this can be done is the equilibrium constant *K'*. According to Eq. 5-25, it is composed of K_{TG} and the ratio of $[B^{(4)}]$ to $[B^{(2)}]$. On the face of it, this latter ratio is expressed as K_B in Eq. 5-7, except that

this equilibrium constant pertains to the binary alkali borate glass. However, using the constant value of K_B established for the binary alkali borate system to calculate [$B^{(3)}$] from the measured values of [$B^{(4)}$] in the ternary glasses, with Eq. 5-14 to eliminate [$B^{(2)}$], the dashed line in Figure 5 - 1 is obtained. The fact that this line very closely fits the measured [$B^{(3)}$] data points provides strong justification for the approach pursued here, in that it shows the equilibrium constants determined for the binary glass systems to hold across the entire ternary composition range, as was the case for the NBS glasses. The constancy of K_B in the ternary MNF glasses also substantiates our earlier assertion that the network units described by our equilibrium model are indeed primarily statistical entities and therefore subject to the rules of ideal mixtures.

Thus, it can also be assumed that K_{TG} and, consequently, K' are constant for all values of x. Short of the ability to actually measure the concentration of any of the Ge species, the expected strong correlation between the number density of tetrahedrally and octahedrally coordinated network units and the longitudinal modulus, as suggested by the behavior of the borosilicate data, is used to determine the value of K'. To this end, [$Ge^{(3)}$] is calculated from the positive roots of the polynomial in Eq. 5-26, and Eq. 5-15(a) and Eq. 5-23 are used to calculate the concentrations of the other two Ge species. Along with the measured [$B^{(4)}$], we compute $\rho_{T\&O}$. The result depends on K' and we choose as the most likely value for this equilibrium constant the one that provides the best correlation between M' and $\rho_{T\&O}$. In other words, the adiabatic elastic modulus of the glass is used to determine the relative proportion of Ge species as a function

of the glass composition, x. The result of this fitting procedure is shown in Figure 5 - 4(b). The scaling factor is given by $M' = 56.1 + 1706 \cdot \rho_{T\&O}$, with a correlation of 0.97. This fit is achieved with $K' = 115$, i.e., $K_{TG} = 2.83$. The corresponding Ge species concentrations are shown in Figure 5 - 1(b). In the binary sodium germanate glasses, about 73% of Ge is coordinated by four BO, 23% is coordinated by six BO, and 4% by three. This is very consistent with expectations, given that the maximum possible fraction of $Ge^{(6)}$ is 25%, and in the pertinent literature numbers close to this limit are reported.[26–28] Our analysis reveals that a non-negligible fraction of Ge carries NBO, which agrees with results of previous studies using Raman spectroscopy.[29, 30]

As to the relation between elastic properties and the short-range structural order in these glasses, the data shown in Figure 5 - 4 suggest that covalent bonding between NF units is responsible for the vast majority of load transmission. This is consistent with the perception that these glassy networks constitute relatively open structures, i.e., the directionality of the covalent bonds prevents atomic packing dense enough for non-bonded interactions to play a more significant role. In NBS glasses at high silicate concentrations, the introduction of modifier cations results in the creation of NBO, since silicon does not form octahedrally coordinated entities. With increasing x, as revealed by the data in Figure 5 - 1(a), $Si^{(3)}$ units deplete more rapidly than $Si^{(4)}$, and these are preferentially replaced by $B^{(4)}$ units. Hence the concentration of highly coordinated network units initially increases, until the rate of change in unit replacements, given by the slopes of the species concentrations with respect to x,

shifts towards $Si^{(4)}$ units being preferentially replaced by $B^{(3)}$. Consequently, at large *x* the density of highly coordinated network units decreases again, and so does the mechanical stiffness of the network.

Conversely, in the NBG glasses we observe strong network integrity, and therefore high moduli, already for the binary sodium germanate glass, as germanium preferentially enters six-fold coordination as opposed to accommodating NBO. The addition of boron does not add to the network connectivity, as there are few $Ge^{(3)}$ units to be replaced by $B^{(4)}$. In fact, upon increasing *x*, initially mostly $Ge^{(4)}$ are replaced by $B^{(4)}$, which is why $\rho_{T\&O}$ only decreases slightly. The weak maximum in the modulus data can be explained as the result of combining the effects of the delayed decrease in bonding density and the increase in packing density, which allows for non-bonded interactions to contribute the mechanical response of the network. At higher borate concentrations, $\rho_{T\&O}$ decreases more rapidly, which leads to a more compliant network.[31]

5.4 Conclusions

We studied the adiabatic elastic moduli in conjunction with the SRO structural characteristics of two series of MNF glasses, the sodium borosilicate glasses and the sodium borogermanate glasses. In both systems, the atomistic number density monotonically increases with borate concentration, while we observe that the longitudinal, shear and Young's modulus show maxima as a function of number density. To better understand the structural origin of

observed behaviors, we correlate the measured elastic moduli to measures of the network topology, as derived from the relative concentrations of network cations with two-, three-, four-, and six-fold coordination by BO. This required that we first complete the description of these network connectivity measures beyond the quantities known from direct NMR measurement. To this end we developed a statistical model based on formulating the reaction equilibria that underlie the formation of and conversion between the different network cation species.

We use the NBS system to demonstrate the efficacy of the model by ascertaining that the concentrations of all network cation species can be determined based only on the measurement of the concentration of $B^{(4)}$ as a function of the borate concentration, and the value of K_B calculated from the ratio of $[B^{(2)}]$ and $[B^{(4)}]$ measured for the binary alkali borate composition. The species concentrations so obtained are in very good agreement with the measured ones. With the mole fractions of all network species at hand, we evaluated parallels between the composition dependence of a number of measures for network connectivity and that of elastic moduli, and found that the longitudinal modulus is very strongly correlated with the number density of tetrahedrally connected network cations. This is in accordance with the requirement that for a network structure to resist both isotropic and shear deformation, its nodes must be linked up in all spatial dimensions.

Compared to the NBS glasses, the NBG system features one additional network unit, i.e., $Ge^{(6)}$, and therefore requires three constraints to determine the

relative proportions of all network units. Here we used the measured concentrations of two boron species and the equilibrium model that applied to this system. The equilibrium constant in this model is unknown for lack of the ability to measure the concentrations of germanium species, even in the binary compositions. We therefore used the expected strong correlation between the number density of tetrahedral plus octahedral network cations and the longitudinal modulus to calculate this equilibrium constant based on a non-linear least-square fit of the latter measure by the former. Accordingly, most germanium cations are four-fold coordinated and about one fifth of them are six-fold coordinated by BO. In addition, a non-negligible fraction of germanium carries NBO. Moreover, the strong correlation between elastic moduli and the number density of highly connected network units for both systems reveals that covalent bonding is responsible for the vast majority of load transmission, trumping the effect of atomic packing.

5.5 References

1. Y.B. Saddeek, A.M. Abousehly & S.I. Hussien, 'Synthesis and several features of the Na_2O-B_2O_3-Bi_2O_3-MoO_3 glasses,' *Journal of Physics D: Applied Physics* **40**, 4674 (2007)

2. V.K. Deshpande, 'Science and technology of glassy solid electrolytes,' IOP Conference Series: Materials Science and Engineering **2**, 012011 (2009)

3. D. Zielniok, C. Cramer & H. Eckert, 'Structure/property correlations in ion-conducting mixed-network former glasses: Solid-state nmr studies of the system Na_2O-B_2O_3- P_2O_5,' *Chemistry of Materials* **19**, 3162 (2007)

4. O.L. Anderson & D.A. Stuart, 'Calculation of activation energy of ionic conductivity in silica glasses by classical methods,' *Journal of the American Ceramic Society* **37**, 573 (1954)

5. T. Rouxel, 'Elastic properties and short to medium range order in glasses,' *Journal of the American Ceramic Society* **90**, 3019 (2007)

6. M.S. Gaafar, N.S.A. El-Aal, O.W. Gerges & G. El-Amir, 'Elastic properties and structural studies on some zinc-borate glasses derived from ultrasonic, ft-ir and x-ray techniques,' *Journal of Alloys and Compounds* **475**, 535 (2009)

7. M. Kodama, 'Ultrasonic velocity in sodium borate glasses,' *Journal of Materials Science* **26**, 4048 (1991)

8. M. Kodama, T. Hirashima & T. Matsushita, 'Anomalous behaviour of ultrasonic velocity in caesium borate glasses,' *Physics And Chemistry Of Glasses* **34**, 129 (1993)

9. M. Kodama, T. Matsushita & S. Kojima, 'Velocity of sound and elastic properties of Li_2O-B_2O_3 glasses,' *Japanese Journal Of Applied Physics* **34**, 2570 (1995)

10. I.Z. Hager, 'Elastic moduli of boron oxyfluoride glasses: Experimental determinations and application of makishima and mackenzie's theory,' *Journal of Materials Science* **37**, 1309 (2002)

11. A. Makishima & J.D. Mackenzie, 'Direct calculation of young's moidulus of glass,' *Journal of Non-Crystalline Solids* (1973)

12. A. Pedone, G. Malavasi, A.N. Cormack, U. Segre & M.C. Menziani, 'Insight into elastic properties of binary alkali silicate glasses; prediction and interpretation through atomistic simulation techniques,' *Chemistry of Materials* **19**, 3144 (2007)

13. P.J. Bray & J.G. O'keefe, 'Nuclear magnetic resonance investigations of the structure of alkali borate glasses,' *Phys. Chem. Glasses* **4**, 37 (1963)

14. W.J. Dell, P.J. Bray & S.Z. Xiao, '11B NMR studies and structural modeling of Na_2O-B_2O_3-SiO_2 glasses of high soda content,' *Journal of Non-Crystalline Solids* **58**, 1 (1983)

15. L.-S. Du & J.F. Stebbins, 'Nature of silicon-boron mixing in sodium borosilicate glasses: A high-resolution 11B and 17O NMR study,' *The Journal of Physical Chemistry B* **107**, 10063 (2003)

16. J.D. Epping, W. Strojek & H. Eckert, 'Cation environments and spatial distribution in Na_2O-B_2O_3 glasses: New results from solid state NMR,' *Physical Chemistry Chemical Physics* **7**, 2384 (2005)

17. J. Zhong & P.J. Bray, 'Change in boron coordination in alkali borate glasses, and mixed alkali effects, as elucidated by NMR,' *Journal of non-Crystalline Solids* **111**, 67 (1989)

18. V.K. Michaelis & S. Kroeker, '73Ge solid-state NMR of germanium oxide materials: Experimental and theoretical studies,' *The Journal of Physical Chemistry C* **114**, 21736 (2010)

19. M. Micoulaut, L. Cormier & G.S. Henderson, 'The structure of amorphous, crystalline and liquid GeO_2,' *Journal of Physics: Condensed Matter* **18**, R753 (2006)

20. J. Kieffer, 'Mechanical degradation and viscous dissipation in B_2O_3,' *Physical Review B* **50**, 17 (1994)

21. F.M. Ernsberger, 'Mechanical properties of glass,' *Journal of Non-Crystalline Solids* **25**, 293 (1977)

22. T. Deschamps, J. Margueritat, C. Martinet, A. Mermet & B. Champagnon, 'Elastic moduli of permanently densified silica glasses,' *Scientific Reports* **4**, (2014)

23. K.M. Heidemann, A. Sharma, F. Rehfeldt, C.F. Schmidt & M. Wardetzky, 'Elasticity of 3D networks with rigid filaments and compliant crosslinks,' *Soft Matter* **11**, 343 (2015)

24. L. Huang, L. Duffrene & J. Kieffer, 'Structural transitions in silica glass: Thermo-mechanical anomalies and polyamorphism,' *Journal of Non-crystalline Solids* **349**, 1 (2004)

25. L. Huang & J. Kieffer, 'Amorphous-amorphous transitions in silica glass. I. Reversible transitions and thermomechanical anomalies,' *Physical Review B* **69**, 224203 (2004)

26. D.D. Martino, L.F. Santos, A.C. Marques & R.M Almeida, 'Vibrational spectra and structure of alkali germanate glasses,' *Journal of Non-crystalline Solids* **293**, 394 (2001)

27. Y.D. Yiannopoulos, G.D. Chryssikos, E.I. Kamitsos, 'Structure and properties of alkaline earth borate glasses,' *Physics and Chemistry of Glasses* **9***,* 164 (2001)

28. Y.D. Yiannopoulos, C.P.E. Varsamis & E.I. Kamitsos, 'Medium range order in glass and thegermanate anomaly'effect,' *Chemical Physics Letters* (2002)

29. T. Furukawa & W.B. White, 'Raman spectroscopic investigation of the structure and crystallization of binary alkali germanate glasses,' *Journal of Materials Science* **15**, 1648 (1980)

30. H. Verweij & J.H.J.M. Buster, 'The structure of lithium, sodium and potassium germanate glasses, studied by raman scattering,' *Journal of Non-Crystalline Solids* **34**, 81 (1979)

31. Y.B. Saddeek, H.A. Afifi & N.S.A. El-Aal, 'Interpretation of mechanical properties and structure of TeO_2–Li_2O– B_2O_3 glasses,' *Physica B: Condensed Matter* **398**, 1 (2007)

CHAPTER 6

IONIC ACTIVATION AND ELASTIC PROPERTIES FOR MIXED NETWORK FORMER GLASS ELECTROLYTES

6.1 Introduction

Solid-state electrolytes exhibiting high ionic conductivity at room temperature are key to increasing the energy and power density of electrochemical energy storage devices, as well as ensuring their safe operation. Most commercially available lithium-ion batteries currently employ liquid electrolytes. Although these provide the best ion transport rate, if it leaks, the flammable solvent can create a severe fire hazard.[1, 2] Upon repeated charge-discharge cycles, deposition of lithium onto the anode can result in the growth of dendrites that eventually short circuit between anode and cathode, which results in the catastrophic malfunction of the device.[3, 4] More importantly, to improve the overall efficiency of battery deployment in applications such as electric vehicles and electronic devices, there exists a continued quest for batteries with increased energy density. Although energy density can be relatively easily improved by utilizing high-capacity or high-voltage cathode materials, the narrow electrochemical window of liquid electrolyte and the device structures required for

their containment are greatly limiting factors.[5] Compared to conventional cells that use liquid electrolytes, all solid-state batteries that fully eliminate the flammables not only solve the safety issue but also improve energy density. Solid electrolytes can assume a load-bearing role, while at the same time suppressing dendrite growth. Both features allow for a significant reduction in the spacing between electrodes, and such a material can offer a fundamental solution to the limited energy density.

Ionic conduction in glasses was discovered many decades ago.[6–10] These glasses have low thermal expansion, good transparency, a wide electrochemical stability window, high mechanical stiffness and hardness. It is easy to adjust their properties by varying their chemical composition, which makes glasses attractive candidates for solid-state electrolytes for lithium ion battery application.[11, 12] High elastic moduli are especially important for suppressing lithium dendrite growth on the anodes. Compared to their crystalline analogues, glasses have relatively good ionic conductivity due to open structure in amorphous state.

However, the cation conductivity in glass is still generally too low for practical use. In this context, the elastic properties of the glass are of particular interests because they originate from the interatomic forces and therefore are a measure of the bonding topology and of the overall structural integrity in the glassy network. Conversely, a highly cross-linked and stiff network is less likely to provide the compliance necessary for a swift passage of migrating cations. Hence, we may expect that structural stiffness and ionic mobility are affected in

opposing directions by the materials design parameters that control the network structure, it is therefore important to examine both properties conjointly. Although various properties of glasses have been extensively studied, very few studies have compared elastic moduli and ionic conductivity in a systematic way. To further elucidate the origin of the ionic transport in glasses and to identify the principal design criteria for solid electrolytes, we investigated the mechanical and transport properties of two mixed network-former (MNF) glass systems: $0.2Na_2O + 0.8[xBO_{1.5} + (1\text{-}x)SiO_2]$ (NBS) and $0.2Na_2O + 0.8[xBO_{1.5} + (1–x)GeO_2]$ (NBG). Upon increasing *x*, one formula unit of borate replaces two silica units, so as to maintain a constant balance of network cations.

6.2 Experimental

6.2.1 Dielectric Impedance Spectroscopy

Impedance spectroscopy was used to determine the ionic conductivities of bulk glass samples. All samples are between 20 and 30 mm in diameter and about 2 mm thick. They are polished to optical smoothness prior to measurements. Gold electrodes typically 20 mm in diameter and 100 nm in thickness are applied by sputtering. Samples are sandwiched between two polished stainless steel blocking electrodes and are measured from 0 to 300^{o}C using the Novocontrol broadband dielectric impedance spectrometer over the frequency range from 0.1 Hz to 10 MHz using a 1V of ac voltage.

6.3 Results and Discussion

In the following we analyze the behavior of the elastic moduli and ionic mobility for two families of glasses, and put them into relation with quantities reflective of prevalent structural elements. To this end, we first summarize what is known about the network topology of these glasses. Specifically, we assess the degree of connectivity within the network, which directly affects the mechanical stiffness of the glasses and at the same time defines migration pathways and the spatial configuration of modifier cation sites. Possible network units are: silicon coordinated by four oxygens, germanium coordinated by four or six oxygens, and boron coordinated by three or by four oxygens. The oxygen can be either bridging or non-bridging. Bridging oxygen (BO) atoms are shared between two network cations, whereas non-bridging oxygen (NBO) are bonded to only one network cation. As specified in our previous chapter we designate the coordination of a network cation by BO using the corresponding number in parenthesis as a superscript, conforming to the Q_n notation used in NMR spectroscopy analysis. We specify the proportion of BO and NBO in the subscript of the oxygen symbol. For example, $M^{(a)}O_{a/2+b}$ refers to network cation *M* that is coordinated by *a*+*b* total oxygen atoms of which *a* are BO and *b* NBO. Dividing the number of BO in the subscript of the O symbol by two indicates that they are shared between two cations.

In the MNF structures $B^{(2)}$, $Si^{(3)}$, and $Ge^{(3)}$ species each carry one charged NBO, whereas $B^{(4)}$ and $Ge^{(6)}$ have one, respectively two charged BO (CBO). The concentration of these species therefore determines the density of modifier

cation sites, and provides an estimate of the average jump distance overcome by these cations in an elementary migration step. In this study, the concentrations of $B^{(3)}$ and $B^{(4)}$ species have been directly measured using NMR spectroscopy for all glasses. Additional constraints, such as molar balances for network formers, e.g., for NBG glasses: $[B^{(2)}] + [B^{(3)}] + [B^{(4)}] = x$ and $[Ge^{(3)}] + [Ge^{(4)}] + [Ge^{(6)}] = 1–x$, and the requirement for charge neutrality, e.g., $[B^{(2)}] + [Ge^{(3)}] + [B^{(4)}] + 2[Ge^{(6)}] = [Na]$, where square brackets indicate mol fractions of these species, allow one to infer additional concentrations from the measured ones. For NBS glasses, the same equations apply when replacing Ge with Si and omitting the term $[Si^{(6)}]$. Hence, given that NBS glasses contain five network species, with three constraint equations and two species concentrations measured, the entire speciation is known. NBG glasses have six network species and the same number of constraints, which would require measurement of an additional species concentration. However, this was not possible due to limitations associated with NMR spectroscopy. Instead, we formulated a statistical thermodynamic model based on reaction balances between various network species, such as for example

Eq. 6-1 $$B^{(4)}O_{4/2} + 2Ge^{(3)}O^{-}_{3/2+1} \rightleftharpoons B^{(2)}O^{-}_{2/2+1} + Ge^{(4)}O_{4/2} + Ge^{(6)}O^{2-}_{6/2} \qquad K = \frac{[B^{(2)}][Ge^{(4)}][Ge^{(6)}]}{[B^{(4)}][Ge^{(3)}]^2}.$$

The equilibrium constants for the reactions that occur in ternary glass compositions, are obtained by using the observed strong correlation between adiabatic elastic moduli and the number density of highly coordinated network units, and employing an iterative non-linear least-square fitting procedure.

While the relative proportion of the two network formers, as expressed by the variable *x*, is the principal parameter for the design of the experiments, in terms of structural design of these glasses and property control, other quantities may prove useful. For example, it is generally understood that the elastic modulus is related to density at a fundamental level in that it provides a measure of the number of structural units per unit volume capable of bearing load. Given the large differences between the atomic masses of the network cations, the atomic number density, ρ_N, calculated as the density divided by the molar mass, or equivalently, the number of atoms per formula unit divided by the molar volume, proves to be most representative of the packing efficiency within the structure. For NBS glass ρ_N varies from 0.0713 $Å^{-3}$ to 0.0927 $Å^{-3}$ and that for NBG varies from 0.0765 $Å^{-3}$ to 0.0927 $Å^{-3}$, with absence of the sample at $x = 0$. Also, for both NBS and NBG systems ρ_N varies monotonically with borate mol fraction *x*. Hence, due to the straightforward mapping between the mol fraction and ρ_N, the latter provides additional information about the structural constitution of the glasses, without detracting from the dependence of various properties on the chemical composition of the system.

In Figure 6 - 1(a) the number densities of charged oxygen atoms, including NBO and BO associated with over-coordinated network cations, ρ_{O^-}, are plotted as a function of the borate mole fraction, *x*, for NBS (circles) and NBG (square) glasses. These number densities are derived from the molar fractions of the various network species that contribute charged oxygen atoms, as specified above. They are obtained through direct measurement, molar and charge

balances, and the application of our statistical thermodynamic model. The resulting quantities are plotted in Figure 6 - 1(b). The sums of these number densities, weighted by the number of charged oxygen they carry, yield the charged oxygen densities shown in In Figure 6 - 1(a) as symbols. The dashed and dotted lines represent the sodium number densities, ρ_{Na}, of these systems. As required by the condition of charge neutrality, lines and symbols should coincide. Indeed, for the NBG system they do, and the values agree to the fourth

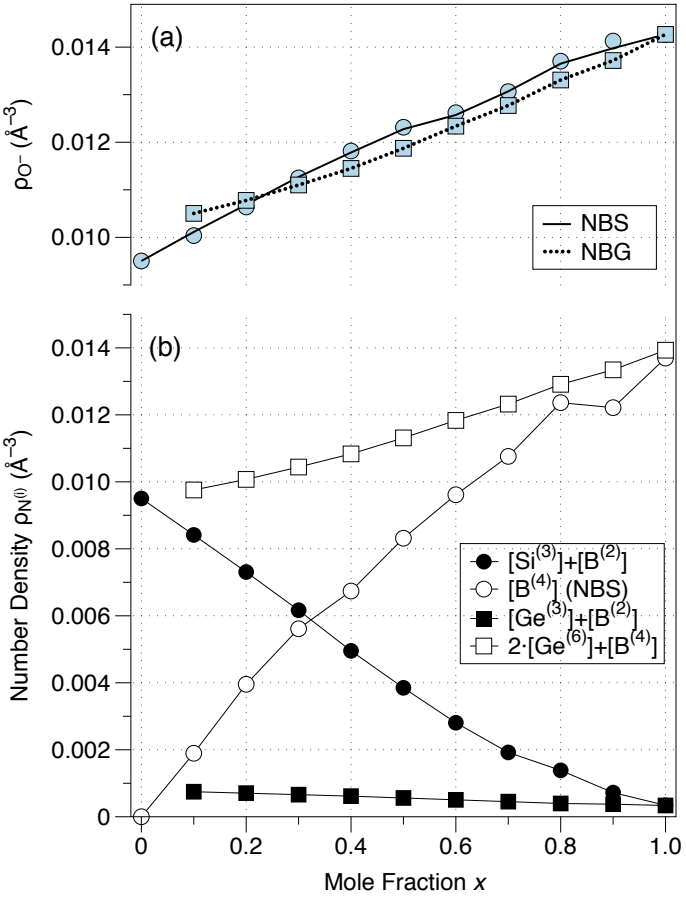

Figure 6 - 1 (a) Number density of charged oxygen species, ρ_{O^-}, for NBS (circles) and NBG (squares) glasses. The dashed and dotted lines represent the sodium number densities; (b) number densities of different combinations of network cation species. Circles represent the species in NBS glasses, and squares those in NBG glasses.

decimal place at a minimum. For the NBS system slight differences can be observed, notably at the x = 0.9 composition, where the measured boron species concentration markedly deviates from probable trends. Nevertheless, the agreement between expected and as determined number densities is excellent, which attests to the compositional accuracy of the samples and the quality of our analytical model. Note that, because the mol fraction of sodium is constant across the entire composition range, ρ_{Na}, and consequently, the charge oxygen number density ρ_{O^-}, exhibit the exact same composition dependence as the overall number density, ρ_N, except that the magnitude of the latter is obviously higher. Hence, data shown in Figure 6 - 1(a) illustrates the almost linear scaling between x and ρ_N.

Based to this analysis, we observe that the nature of the modifier cation sites significantly differs between the NBS and NBG systems. In the former, Na cations are predominantly accommodated by NBO sites in silica-rich glasses, and with increasing x sites switch over to the ones established by CBO, reaching near completion in the borate-rich glasses. Conversely, in NBG glasses modifier cation sites coordinated CBO dominate throughout the entire composition range. The few NBO sites gradually disappear as the borate concentration increases.

In the context of cation transport, ρ_{O^-}, represents the density of waymarkers for the migration of sodium. The ionic conductivity for both the sodium borosilicate and sodium borogermanate glasses show a so-called mixed glass former effect. The dependence of the ionic conductivity on the composition is non-linear and non-additive.[13] Figure 6 - 2 shows the ionic conductivity, σ,

derived from dielectric impedance spectroscopy measurements for both glass systems at several temperatures.

For NBS glasses, the ionic conductivity as a function of *x* exhibits a broad and shallow minimum between x=0.6 to 0.8, at all temperatures. For NBG glasses, the conductivity generally increases with *x*, but it could be argued that a weakly defined minimum is located at x= 0.2. Although the two plots are for slightly different temperatures, the silicates exhibit higher overall ionic conductivity than the germanates, especially at lower temperatures.

Comparing ionic conductivities with the data presented in Figure 6 - 1, one could argue that for NBG glasses σ and ρ_{O^-} follow a similar trend as a function of the borate concentration. This is, however, not the case for NBS glasses. At best one could conjecture that the minimum in the conductivity data somehow reflects the intersection between majority defect concentrations, i.e., NBO at high silica concentrations and CBO at high borate concentrations. This would imply that sodium cations preferentially hop between sites of the same type, i.e., from NBO to NBO and from CBO to CBO, while avoiding jumps between NBO and CBO. The reason for such selectivity is not at all obvious. Moreover, the minimum in conductivity would have to occur closer to x = 0.3, for this hypothesis to be plausible. The true explanation may therefore be found elsewhere.

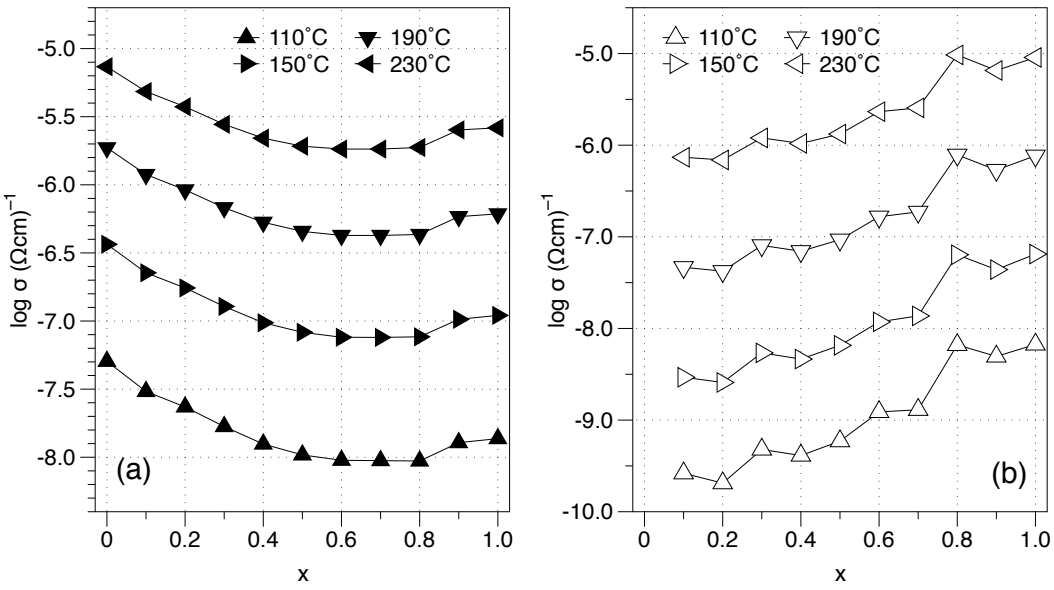

Figure 6 - 2 Ionic conductivity (a) for sodium borosilicate at 110°C, 150°C, 190°C and 230°C, and (b) for sodium borogermanate at 100°C, 140°C, 180°C and 220°C.

While much research has been devoted to understanding how glass composition and structure can enhance the mechanical properties of these materials,[14, 15] and, independently, their ionic conductivity,[10, 11, 16, 17] examining both properties jointly in a systematic way has not been done to a significant extent. Hence, the relationship between ionic mobility and the elastic response of the embedding structure remains by and large unclear. However, in view of developing better performing solid-state electrolytes, this knowledge is important.

While the longitudinal and shear moduli are measured directly using BLS, Young's modulus, *E*, the bulk modulus, *K*, and Poisson's ratio, ν, can be calculated from the longitudinal and shear moduli according to

Eq. 6-2 $$E = \frac{G(3M-4G)}{M-G}$$

Eq. 6-3 $$K = M - \frac{4G}{3}$$

Eq. 6-4 $$\nu = \frac{M-2G}{2M-2G}$$

The elastic moduli for the two series of glasses are shown in Figure 6 - 3 as a function of the number density. In almost all cases, the elastic moduli exhibit a maximum as a function of *x*. For NBS glasses, the longitudinal, Young's, and the shear moduli peak at ρ_N = 0.084, and the bulk modulus at ρ_N = 0.087. For NBG glasses, the longitudinal, shear and Young's moduli reach a maximum at ρ_N = 0.081 while the bulk modulus decreases monotonically with ρ_N, yet exhibiting a weak curvature that echoes the behaviors of the other moduli. The change in modulus with ρ_N for the NBG series is smaller than for the borosilicates. Notice that in both cases, the trend for the bulk modulus is slightly different than that for any of the other moduli.

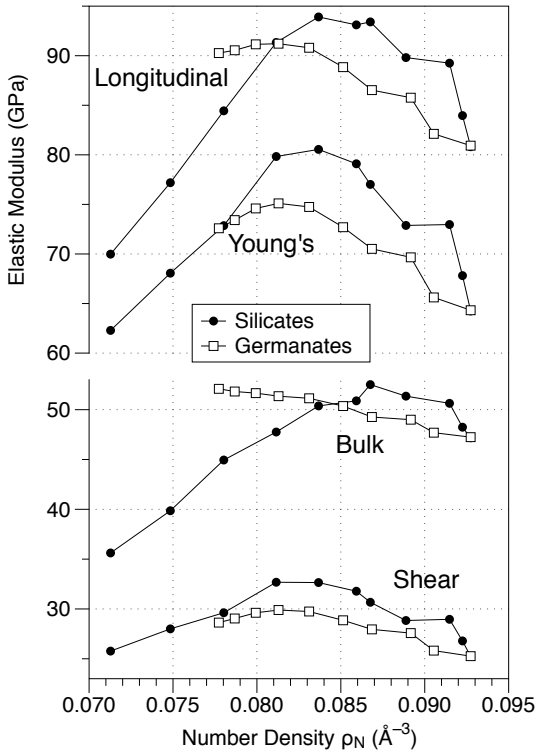

Figure 6 - 3 Longitudinal and shear elastic moduli as a function of the number density for the borosilicates and borogermanates.

The number density, in atoms per unit volume, is a measure of how densely the atoms reside in a structure, and by inference, how effectively load is transferred between structural building blocks. Accordingly, it is generally accepted that materials are stiffer and the elastic moduli are higher when they are packed more densely.[18, 19] As a result, the elasticity of materials increases with their packing density.[20, 21] However, while in these two series of glasses, both longitudinal and shear modulus exhibit an initial increase, they reach a maximum followed by a decrease as a function of number density. The observed behaviors therefore suggest a more intricate relationship between structural stiffness and packing density.

A detailed analysis of the relationship between elastic properties and the structural characteristics of the MNF glasses is described in previous chapter. In short, our investigation revealed a strong correlation between the number density of network cations coordinated by four or more bridging oxygen atoms, i.e., $Si^{(4)}$ and $B^{(4)}$ in NBS glasses and $Ge^{(4)}$, $Ge^{(6)}$ and $B^{(4)}$ in NBG glasses, and the adiabatic elastic moduli. This is because tetrahedral and octahedral units are required to achieve connectivity in three dimensions, giving rise to restoring forces in response to both shear and longitudinal deformation. Hence, for inorganic MNF glasses the number of BO is the prevalent factor responsible for stiffness because the strong covalent bonds between network building blocks increase the load-bearing capacity of the glassy network, while non-bridging oxygen opens the glass network and renders it mechanically more compliant.[22]

Given that ionic conductivity and elastic moduli exhibits opposite trends in terms of slopes and extrema in their composition dependence, it is natural to compare the elastic modulus with the inverse of ionic conductivity, namely, the ionic resistivity, ρ_e, as shown in Figure 6 - 4, where we used the fact that on a log-scale resistivity and conductivity are simply related as $-\log \sigma = \log \rho_e$. Here we plot the logarithm of the resistivity and the bulk modulus on independent scales and observe that the two measures track one another very well. The units of eV/Å^3 are chosen for the elastic modulus to reveal its nature as the capacity to store elastic energy per unit volume. Using independent scales for this comparison is indicated because the two quantities are measured in different units, and it simply amounts to a linear scaling of one quantity relative to the other. The insets of Figure 6 - 4 show the quality of this linear correlation. The slope resulting from the linear regression of the data is used to scale the left- and right-hand side vertical axes for the comparison. As is apparent, the resistivity and modulus data follow one another very closely. This linear correlation can be written as

Eq. 6-5 $$-\ln\sigma = aK + b\,,$$

The bulk modulus was chosen for the purpose of the argument, but the expression can be generalized to encompass both shear and volumetric deformations, as detailed below. In principle it is possible that the coefficients *a* and *b* are different if this scaling is performed for the conductivity data at a different temperature. Therefore, to accommodate the most general scenario, we begin by considering these coefficients to be temperature dependent.

Furthermore, given that conductivity follows an Arrhenius relationship, we can write

Eq. 6-6 $$\sigma(T) = \sigma_0 e^{-E_a/k_B T} \Leftrightarrow -\ln\sigma(T) = -\ln\sigma_0 + E_a/k_B T ,$$

where σ_0 is a pre-factor that depends weakly on temperature and E_a is the activation energy for ion hopping. Substituting the expression of Eq. 6-6 for the left-hand side of Eq. 6-5 yields

Eq. 6-7 $$-\ln\sigma_0 + E_a/k_B T = a\, f(\lambda,\mu) + b \Rightarrow E_a = A(T) f(\lambda,\mu) + B(T),$$

where $A(T) = a k_B T$ and $B(T) = k_B T(b + \ln\sigma_0)$. We also replaced the bulk modulus with a more general expression characterizing elastic deformation, namely a linear combination of the two Lamé coefficients, λ and μ, which describe all linear elastic deformations in an isotropic solid and conveniently separate diagonal and off-diagonal coefficients from the elasticity tensor. Since the activation energy is observed to be constant over the temperature range investigated, we can assume that the terms on the right-hand side of Eq. 6-7 are either weak to begin with or they mutually compensate. Either way, the need to consider the temperature dependence of $A(T)$ and $B(T)$ is only as strong as doing so for the activation energy itself.

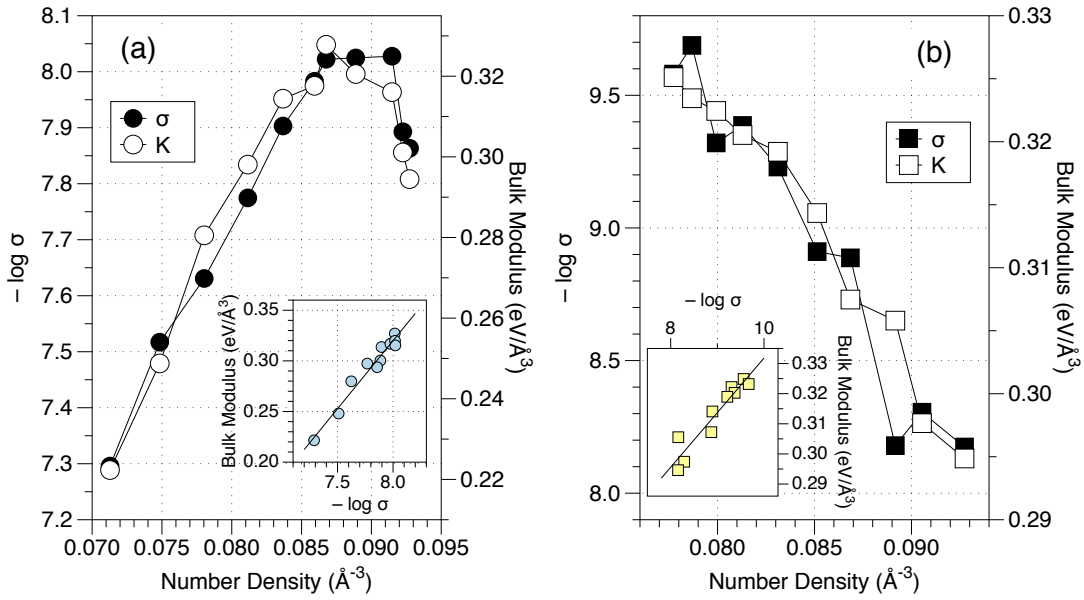

Figure 6 - 4 Comparison between the dependence on the atomic number density of the bulk modulus and the logarithm of ionic resistivity for NBS and NBG glass systems. Insets: Correlation between the two quantities. The linear slope serves to scale the two independent ordinates for the comparison.

To advance with our analysis, we examine the energy associated with the event of a sodium cation hopping from one stable site to another. As the cation moves along its trajectory, the system experiences a change in its potential energy, which amounts to the aforementioned activation energy within the framework of the transition state theory. To evaluate this energy, we follow an approach similar to the one developed by Anderson and Stuart.[23] Throughout the cation hopping process the only changes in atomic positions that are known determinately are those of the cation itself. Hence, the first installment towards the activation energy arises from the Coulomb interactions between the migrating cation and the charged species at the cation equilibrium sites. The atoms are assumed to be stationary; they remain in their ground state position during the

jump. The removal of the cation from such a site is the basic requirement for a jump to occur, while the “ground-state” neighbors must remain behind for the displacement to be finite. For lack of explicit models of the atomic structure of these glasses, the jump distances must be estimated in a mean-field approximation based on the NBO and CBO number densities shown in Figure 6 - 1.

The MNF glass systems contain two types of charge oxygen species that can arrange into modifier cation sites, NBO and CBO. It is generally understood that, in systems where network modification results predominantly in the formation of NBO, the stable sites for the modifier cations are NBO pairs, as depicted in Figure 6 - 5(a), which provide energy minima as a result of strong Coulomb interactions. However, little is known about modifier cation sites involving CBO. We therefore carried out the calculations described in the following for different configurations, depicted in Figure 6 - 5 (b)-(h). In cases where the sodium sites involve only a single CBO, we found that either the gap between CBOs is too small to accommodate a second sodium site, as shown in Figure 6 - 5 (b), or assuming the scenario shown in Figure 6 - 5 (c), the jump distance may be reasonable, but the midpoint between CBOs is the location with the lowest Coulomb energy for sodium, and hence there is no activation barrier. We conclude that CBOs also must pair up to form stable sodium sites, and they must include a charge-balancing second sodium cation near each of the migrating cation’s start position and ending positions.

The requirement for pairing charged oxygen species effectively lowers the sodium site number density and increases the jump distance to a reasonable value. Furthermore, the pairing requirement allows for combining one NBO and one CBO into a stable sodium site. This, however, does not complicate our calculations because, discounting possible effects of network topological constraints, the sodium site density in the MNF systems can now be calculated as the sum of the NBO and CBO number densities divided by two. This density, and what is known from the literature about the sodium-oxygen nearest neighbor distances, [24] then defines the dimensions in the schematic shown in Figure 6 - 5 (e)-(h). Based on these measures and atomic positions, we compute the difference of this Coulomb energy when the migrating cation is at the midpoint between cation sites, or saddle point (SP) and its ground state (GS) according to

Eq. 6-8 $$E_C = \sum_{i=1}^{6}\sum_{j>i}^{7}\frac{Z_i Z_j e^2}{4\pi\varepsilon_0 r_{ij}}\Big|_{SP} - \sum_{i=1}^{6}\sum_{j>i}^{7}\frac{Z_i Z_j e^2}{4\pi\varepsilon_0 r_{ij}}\Big|_{GS}$$

Essential for the derivation that follows is that the positions of these atoms can be considered representative of their energetic ground state and they are static during the jump process. All displacements other than that of the migrating cation are accounted for in the elastic strain energy derived in the next several paragraphs. The cation jump distance changes slightly as boron replaces silicon or germanium, respectively, hand hence, E_C exhibits a weak linear dependence on the number. Our results are in good agreement with values reported in the literature.

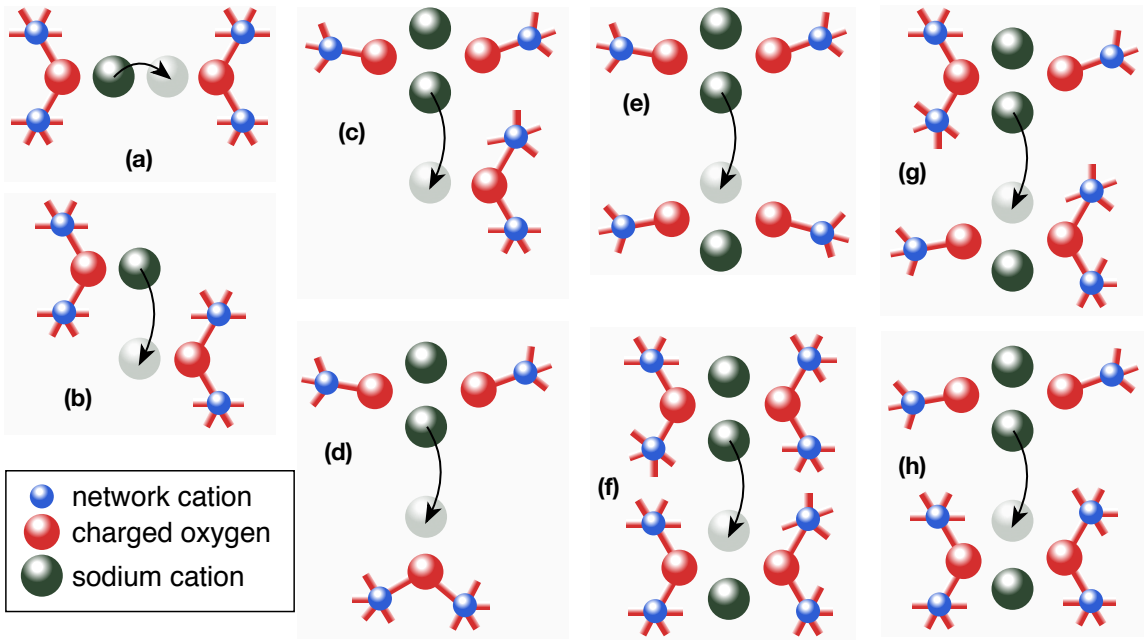

Figure 6 - 5 Schematic of the ground state configurations of sodium cation sites and possible jump patterns. Configurations (a) and (b) illustrate jumps between cation sites involving only a single CBO. In the first case the distance between sites, assuming uniform distributions of CBOs is too short. The most stable position for the cation is halfway between the CBOs. For scenario (b), the jump distance is increased based on a uniform distribution of sodium cations in space, but again the most stable position for sodium is hallway between the CBOs. Configurations (c) and (d) show possible jump patterns involving a pair of NBOs and a single CBO. For these the Coulomb energy exhibits a steady slope between sites, i.e., no activation barrier separates the cation sites, and only one of the positions is stable. Configurations (e) through (h) show sites made up by pairs of charged oxygen atoms, either NBO, CBO, or mixtures thereof. The density of these sites is half the number density of charged oxygen atoms, which results in a reasonable spatial separation, and the jumps are characterized by a finite difference in the Coulomb energy between GS and SP.

According to transition state theory the probability for a cation to jump between stable sites is based on comparing the energy difference between the ground state to the saddle point along the minimum energy trajectory of the cation with the thermal energy imparted on the system, using Boltzmann statistics. When the cation advances from its stable site surrounded by NBO or

CBO, which approximately corresponds to the bottom of the energy well for this particle, to the midpoint between stable sites raises its energy increases for two reasons: one is that its distance from the charge-compensating charged oxygen has increased, working against an attractive force, and the other one is due to the repulsive forces of structural moieties that obstruct the passage of the cation towards its new site. The physical picture underlying transition state theory does, however, not imply that all of the kinetic energy (k_BT) required to overcome the activation barrier (E_a) be imparted in the migrating cation. Indeed, considering that a typical activation energy is of the order of 1 eV per atom, if this had to manifest as kinetic energy of on single atom, the local temperature would exceed 10,000 K. Rather, it is dispersed within the cation's immediate vicinity. The resulting thermal motion of the surrounding structure still rises momentarily above its base level, and eventually provides a fortuitous constellation that facilitates the passage of the cation.

The magnitude and direction of atomic displacements, and the spatial extent of the affected region, i.e., what atoms participate in this enhanced activity, can only be surmised. Short of knowing the atomic configurations surrounding the pair of cation sites involved in the jump, the excess energy associated with the underlying structural deformation cannot be calculated explicitly, and we must treat this region using a mean-field approach, considering all displacements of structural moieties, other than the hopping cation, as purely elastic. To this end, we consider the expression for the energy U associated with elastic deformations[25]

Eq. 6-9 $$U = U_0 + \frac{1}{2}\lambda \sum_i \varepsilon_{ii}^2 + \mu \sum_i \sum_{k>i} \varepsilon_{ik}^2 ,$$

where λ and μ are again the Lamé coefficients introduced with Eq. 6-7, U_0 is the energy of the structure in the ground state and ε_{ik} are the elements of the symmetric strain tensor. Eq. 6-9 represents a Taylor expansion of the energy as a function of the strain and relative to the ground state. In this approximation, the first order derivative terms vanish because all forces are balanced in the ground state. We can regroup the strains into components that are purely shear and purely hydrostatic by using the identity

Eq. 6-10 $$\varepsilon_{ik} = \left(\varepsilon_{ik} - \frac{1}{3}\delta_{ik}\varepsilon_{ll} \right) + \frac{1}{3}\delta_{ik}\varepsilon_{ll} ,$$

and substituting into Eq. 6-9,

Eq. 6-11 $$\Delta U = \frac{1}{2}\left(\lambda + \frac{2}{3}\mu \right) \sum_l \varepsilon_{ll}^2 + \mu \sum_i \sum_{k>i} \left(\varepsilon_{ik} - \frac{1}{3}\delta_{ik}\varepsilon_{ll} \right)^2$$

of which the first term on the right hand side represents the energy stored in isotropic deformations, and the second term the energy stored in shear deformations. In this expression, $\lambda + \frac{2}{3}\mu = K$ is the bulk modulus, and $\mu = G$ is the shear modulus. Note that the quantity defined by Eq. 6-11 has the units of energy per unit volume. To calculate the energy per migrating cation, we need to multiply ΔU with the volume of the region that is deformed in order to facilitate the cation jump, V_a. This volume is not known *a priori*, and neither are the values of the sums of strains in Eq. 6-10, which we will designate by $\omega_K = \frac{1}{2}\sum_l \varepsilon_{ll}^2$ and

$\omega_G = \sum_i \sum_{k>i} \left(\varepsilon_{ik} - \frac{1}{3}\delta_{ik}\varepsilon_{ll} \right)^2$ for convenience. Based on their definitions, however, we know that both ε_K and ε_G are positive quantities. We rewrite Eq. 6-11 in a more compact form,

Eq. 6-12 $$E_\Delta = V_a\left(K\omega_K + G\omega_G\right) = V_a\left(\omega_K + \omega_G\right)\left[K\xi + G\left(1-\xi\right)\right] = \Phi\left[K\xi + G\left(1-\xi\right)\right]$$

where E_Δ is the elastic energy per migrating cation. The weighting factor $\xi = \omega_K / \left(\omega_K + \omega_G\right)$ describes the relative proportions of the elastic energy stored in isotropic vs. shear deformation according to Eq. 6-11. Here we combine the affected volume and strain-dependent quantities into one variable $\Phi = V_a\left(\omega_K + \omega_G\right)$, since neither are known explicitly. However, and effective value of the product of the two can be obtained from our analysis. The sum of the Coulomb and elastic energies equate to the activation energy, and we can rewrite Eq. 6-7 as

Eq. 6-13 $$E_a = A(T) f(\lambda,\mu) + B(T) \equiv E_C + E_\Delta = E_C + \Phi\left[K\xi + G\left(1-\xi\right)\right]$$

From our experiments we know the activation energy for sodium migration, as well as the bulk and shear moduli, and E_C is calculated as detailed above. We can now fit our data to yield the best values for the quantities Φ and ξ. *A priori* we again must assume that these quantities may have composition dependences. In Eq. 6-13 ξ represents the balance between bulk and shear deformation, which strictly varies between 0 and 1, while Φ is a measure of the strain field and the spatial extent of the affected structure. We assume that only Φ depends on composition. This is justified since both quantities occur as a product in the equation. Furthermore, we assume that Φ varies smoothly with

composition. In other words, we do not expect sudden discontinuities when the composition changes slightly. For the fitting procedure we first choose an arbitrary value for ξ and compute estimates of the quantities $\Phi_i^{\text{est}} = \left(E_{a,i} - E_{C,i}\right) \Big/ \left[K_i \xi^{(n)} + G_i \left(1 - \xi^{(n)}\right)\right]$ for each data point. We then fit a fifth order polynomial to the set of estimated Φ_i^{est} as a function of the number density. Based on the fit values for Φ, we can reevaluate the right hand side of Eq. 6-13 and calculate the cost function $\sum_i \left\{E_{a,i} - E_{C,i} - \Phi_i^{\text{fit}} \left[K_i \xi^{(n)} + G_i \left(1 - \xi^{(n)}\right)\right]\right\}^2$, which serves to optimize the value of ξ. Since ξ is strictly bound to a narrow range, considering the desired precision, finding the best value for ξ is done using a simple binary search.

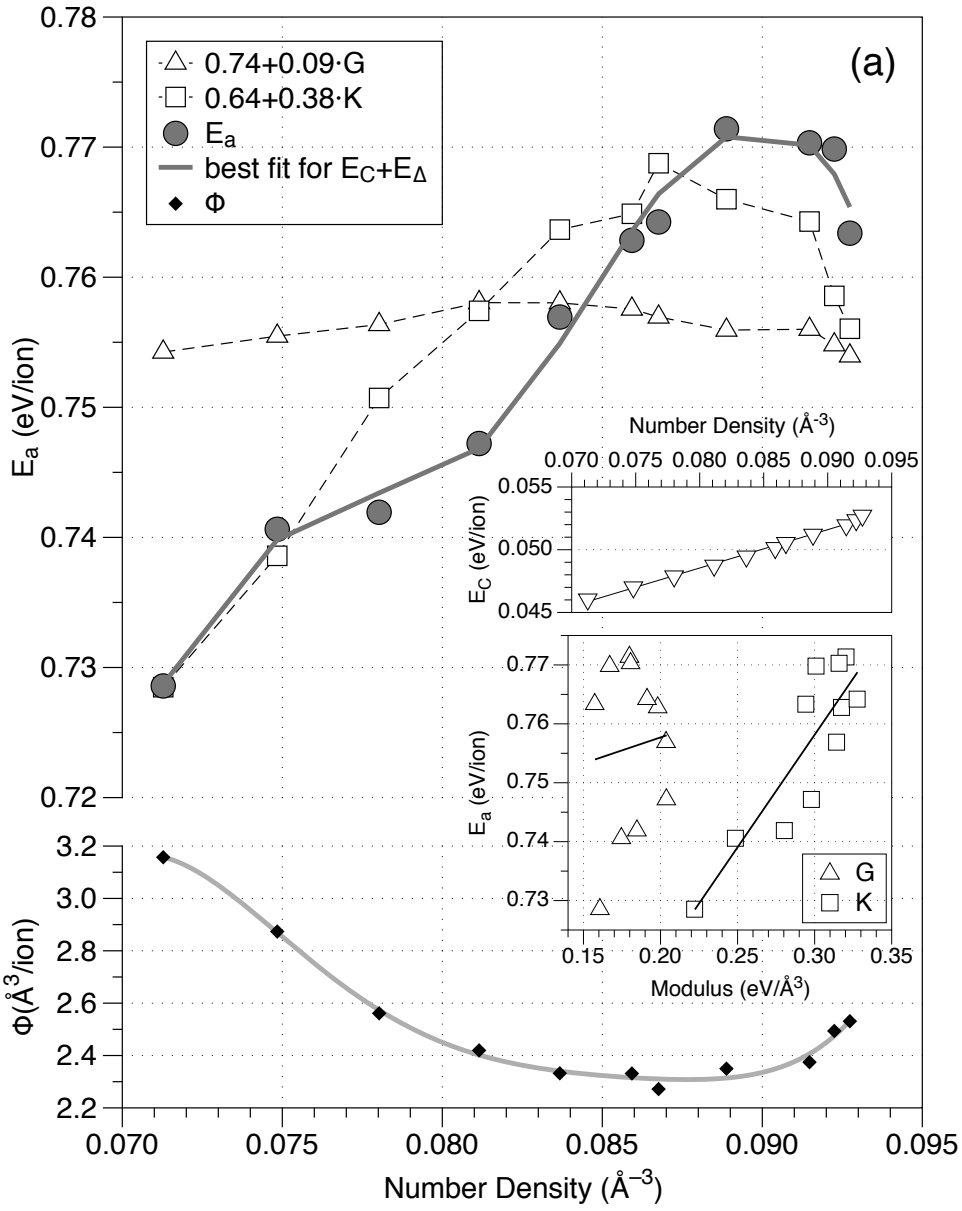
(a)
0.74+0.09·G
0.64+0.38·K
Ea
best fit for EC+EΔ
Φ
Ea (eV/ion)
Φ(Å3/ion)
Number Density (Å−3)
Number Density (Å-3)
EC (eV/ion)
Modulus (eV/Å3)
G
K

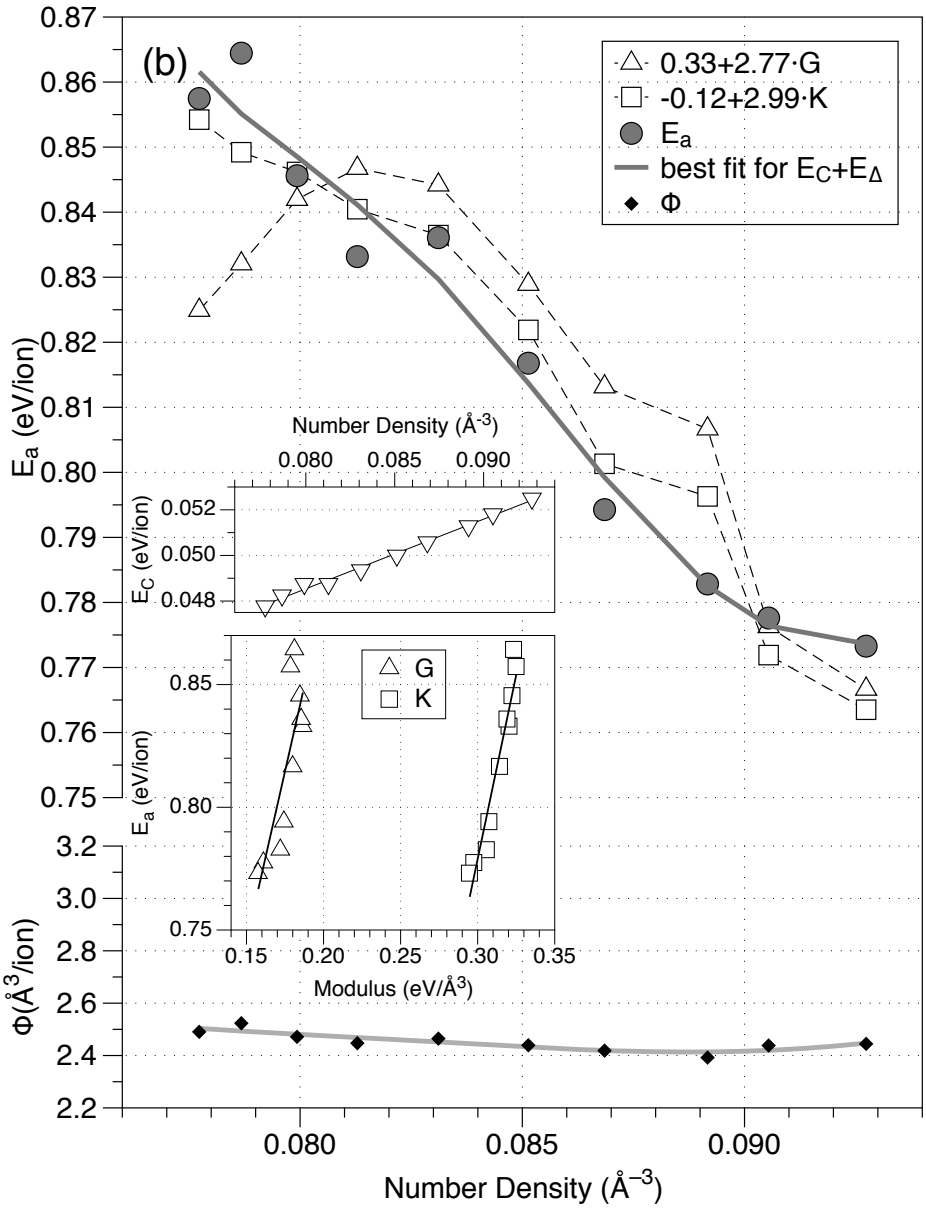

Figure 6 - 6 Comparison between measure activation energies for sodium ion migration (solid circles) and those calculated based on the best fit of the right-hand side expression in. In Eq. 6-13, as a function of the atomic number density. (a) shows the data for sodium borosilicate and (b) for sodium borogermanate glasses. The lower portion of the graphs show the values for Φ using the best fit value of ξ. Inset: the lower part shows the correlation between activation energy and shear, respectively, bulk moduli. The lines represent linear best fits of these data, which are used to project the shear and bulk moduli onto the energy scale. The upper part shows the calculated Coulomb energy as a function of the number density.

The results of the fitting procedure are shown in Figure 6 - 6 (a) and (b). In the upper section of each graph, the filled circles represent the measured activation energies for sodium ion migration, plotted as a function of the atomic number density. The solid line represents the best fit of this data based on the above procedure. One important finding of our analysis is that the best fits obtained are for $\xi = 0.9$ in the case of NBS glasses, and $\xi = 1.0$ in the case of NBG glasses. Accordingly, the excess local structural deformations associated with the cation jump are predominantly, if not purely hydrostatic, and not shear. This is in contrast to previously published analyses of ion migration in glasses based on the Anderson-Stuart model, in which the elastic deformation energy is typically evaluated using the shear modulus.[23, 26] To illustrate this further, we superimposed hypothetical activation energies that are calculated with the assumption that the entire activation barrier can be described as pure shear elastic energy (open triangles) or pure hydrostatic elastic energy (open squares). The hypothetical energies are computed using the measured shear, respectively, bulk moduli, which represent energies per volume, into energies per ion using a linear scaling relationship derived from the fit lines shown in the lower part of the inset. The corresponding scaling relationships are listed in the figure legends. Both, comparing the so-projected hypothetical activation energies with the measure ones and the quality of the correlation in the upper parts of the insets reveal that the bulk modulus aligns significantly better with the measured activation energies than the shear modulus.

This finding, along with the magnitude of the factor Φ, allows us to envision some aspects of the jump process more confidently. Recall that Φ represents the volume affected by the cation jump multiplied with a sum of squared strains. We perceive that the atoms in this volume are displaced in a way that is favorable to the cation jump, which we now understand to be cooperatively outward, so as to establish a mostly isotropic local expansion. To determine the size of the region so affected, we need to estimate the strains associated with the deformation. From neutron diffraction [27] we know that the at room temperature is about 5% of the bond distances. Since we consider that at the moment of the cation jump, displacements occur in unison we assume that the average value of the diagonal elements of the strain tensor are 5% as well. Here we ignore the off-diagonal strain components, given the strong weight of the hydrostatic components revealed by our analysis. Accordingly, we estimate the affected volume to range between 260 $Å^3$ and 350 $Å^3$ in the borosilicates, and between 260 $Å^3$ and 280 $Å^3$ in the borogermanates. This is about three to four times the volume that can statistically be attributed to any given sodium cation in the structure, which is reasonable in the context of our understanding of the modified network structure.

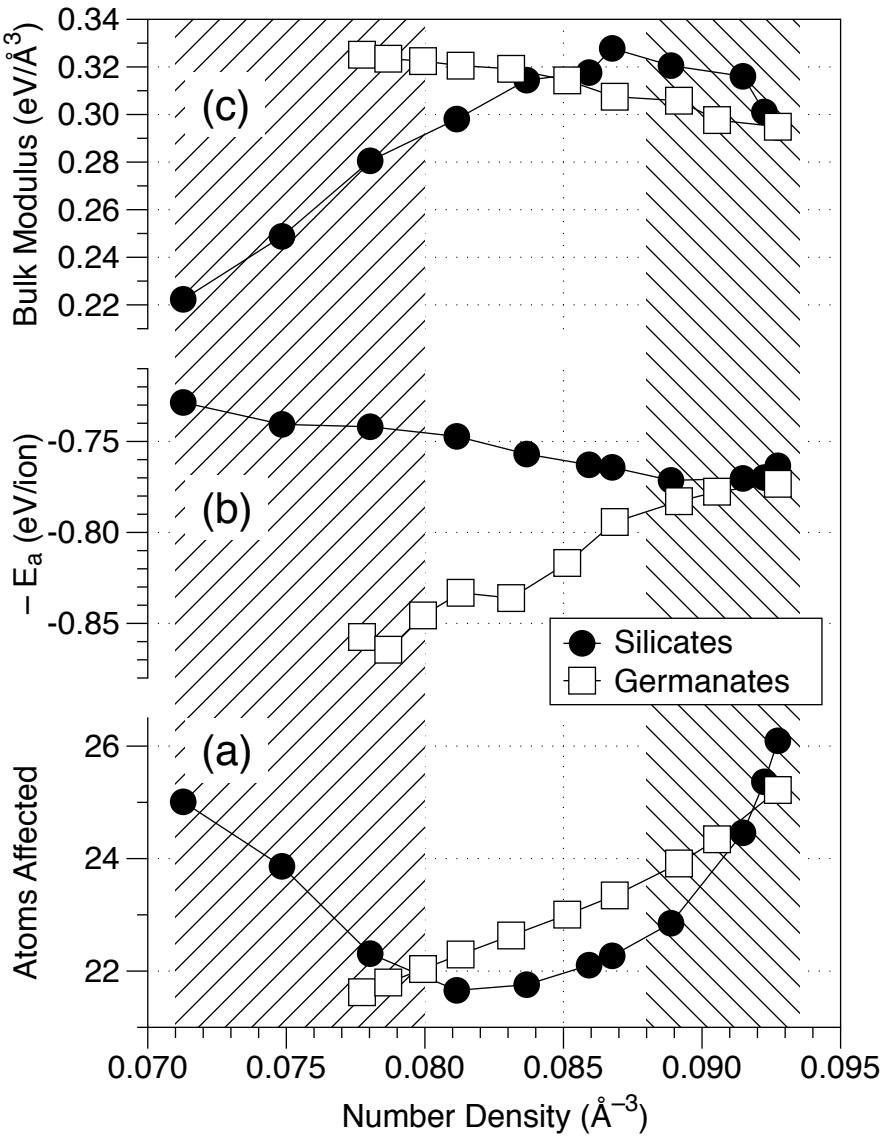

Figure 6 - 7 (a) Negative of the activation energy, which provides a measure of the ion mobility on a logarithmic scale, as a function of the number density; (b) number of atoms whose motion is affected per sodium cation during its activated hopping process. Filled circles represent data for silicates and open square data for germanates.

Another way of looking at the affected volume in a given glass is to account for the number of atoms they contain, simply by multiplying with the respective number densities. This number of affected atoms in each system is shown in Figure 6 - 7a as a function of the number density. For comparison, in Figure 6 -

7(b) we show the negative values of the activation energy, which provides a measure of the cation mobility on a logarithmic scale. We see that for NBG glasses, the number of affected atoms correlates quite well with the cation mobility. The larger the number of affected atoms, the lower the activation energy, and the higher the cation mobility. For NBS glasses a correlation between the two quantities is less obvious. However, closer examination reveals that there are some similarities in number density dependence. At low number densities both the cation mobility and the number of affected atoms decrease, whereas at high number densities both quantities again follow the same, albeit reverse trend. To fully appreciate these subtleties we also need to take the stiffness of the structure into consideration. For convenient comparison, we plot the bulk modulus for each system as a function of the number density in Figure 6 - 7(c).

In particular, to elucidate the relationship between these quantities and the cation migration mechanisms, we envision the atoms onto which the activation energy is imparted as the grouping of structural entities whose concerted motion must be in accord with the jump of a sodium cation in its midst. Accordingly, the number of affected atoms is a characteristic of the cation hopping mechanism, and a target that has to be achieved by realizing atomic displacements in the proper directions and with sufficient magnitude. This condition entails two aspects: one is the element of fortuity associated with the local cooperative motion, and the other is adequate supply of energy. Intuitively, one might expect that the more atoms are involved in the cation jump, the more difficult it is to

achieve proper synchronization of their motion. On the other hand, participation of a larger number of atoms may provide more choices for creating a passable configuration for the cation. Given that, without exception the cation mobility increases with the number of affected atoms, we conclude that the latter interpretation applies, or at least, that more than one single sequence of cooperative displacements can facilitate the cation jump. We would, however, like to emphasize that the data at our disposal does not directly inform about the entropy of motion during the jump process.

Let us now examine the other aspect, the magnitude of displacement. Following the conventional representation of heat capacity in condensed matter, the corresponding local accumulation of thermal motion is best described as a superposition of thermal phonons. To achieve a strong concentration of energy requires the coincidence of a larger number of phonons with relatively short wavelength, i.e., high energies. Hence, if the cation jump mechanism involves the cooperative motion of fewer atoms, it likely results in higher activation energy. Conversely, if a larger number of atoms are involved in the process, the necessary degree of energy concentration is lessened, and can be achieved with the superposition of fewer and lower-energy phonons. This explains the behavior observed for the NBG glasses, as well that of the borosilicates at high number density. In this regime, the elastic modulus of both systems is high, phonon wavelengths are relatively long, and the both mobility and the number of affect atoms increase with decreasing modulus.

Towards low number densities, the stiffness of borogermanates increases and for this system the aforementioned trend prevails. However, the number density dependence of the bulk modulus for the borosilicates decouples from that of the borogermanates. The structure of the borosilicate glasses becomes significantly more compliant towards low number densities, while the activation energy decreases and number of affected atoms increases. This behavior is consistent with the ability to focus the energy necessary for atomic displacements with a smaller number of phonons, especially as they decrease in wavelength in a less rigid structure.

6.4 Conclusions

We studied the adiabatic elastic moduli and ionic transport properties for two series of mixed-network former glasses, the sodium borosilicate glasses and the sodium borogermanate glasses conjointly. In both systems, the longitudinal, shear and Young's modulus show maxima as a function of composition, which is a result of two competing structural factors. These trends closely mirror the number densities of highly coordinated network units, i.e., tetrahedral boron and silicon in NBS glasses, and tetrahedral boron and germanium, as well as octahedral germanium in NBG glasses. These units provide connectivity in three dimensions, which is required for the network to oppose both isotropic and shear deformation. For both systems, the bulk modulus demonstrates different compositional trend than the other moduli and, importantly, the bulk modulus exhibits a strong correlation with the negative logarithm of the ionic conductivity,

as well as the activation energy for ion conduction, at all compositions. We use an extension of the Anderson-Stuart model to further elucidate the cation migration mechanisms in these structures, simultaneously accounting for the observed behaviors in ion mobility and structural rigidity. Our analysis reveals that elastic deformations of the structure surrounding the migrating cation are almost purely hydrostatic instead of shear for both systems.

Furthermore, we derive a measure of the expanse of the affected local environment, e.g., the number of atoms that partake in the activated process of a cation jump. This process requires a certain degree of coincidence in atomic displacements and confluence of energy. While the former is based on exploring the degrees of freedom for atomic motion in real space, the latter can be described as the fortuitous superposition of thermal phonons, and thus depends on the wave character of this manifestation, and ultimately on the elastic properties of the glass structure. We find that in mechanically stiff structures fewer atoms tend to be involved in a cation jump, which requires higher-frequency phonons to focus the thermal energy onto these participating atoms. Consequently, the activation energy is high and cation mobility low. Conversely, in more compliant structures the necessary energy concentration can be achieved by superimposing lower-frequency phonons, which translates to a lower activation energy and higher cation mobility. Accordingly, structures with high hydrostatic mechanical stiffness are likely characterized by low ion mobility, but it may be possible for a structure to exhibit both high ionic conductivity and shear elastic modulus. Overall, it appears that the confluence of energy, i.e., achieving

the required phonon population, is the most constraining factor, and that number of cooperative atomic displacements that lead to a cation jump is comparably larger.

6.5 References

1. K. Xu, 'Nonaqueous liquid electrolytes for lithium-based rechargeable batteries,' *Chemical Reviews* **104(10)**, 4303 (2004)

2. J.M. Tarascon & M. Armand, 'Issues and challenges facing rechargeable lithium batteries.,' *Nature* **414**, 359 (2001)

3. D. Aurbach, E. Zinigrad, Y. Cohen & H. Teller, 'A short review of failure mechanisms of lithium metal and lithiated graphite anodes in liquid electrolyte solutions,' *Solid State Ionics* **148**, 405 (2002)

4. X.W. Zhang, Y. Li, S.A. Khan & P.S. Fedkiw, 'Inhibition of lithium dendrites by fumed silica-based composite electrolytes,' *Journal of The Electrochemical Society* **151**, A1257 (2004)

5. J. Li, C. Ma, M. Chi, C. Liang & N.J. Dudney, 'Solid electrolyte: The key for high voltage lithium batteries,' *Advanced Energy Materials* **5**, (2015)

6. D. Kunze & W. Van Gool, 'Fast ion transport in solids,' *North Holland, Amsterdam* 495 (1973)

7. W. Van Gool, 'Fast ion transport in solids, solid state batteries and devices.' *Proceedings of the NATO-Sponsored Advanced Study Institute of Fast Ion Transport in Solids, Solid State Batteries And Devices, Belgirate, Italy 5-15 September 1972,* (1973)

8. A. Bunde, K. Funke & M.D. Ingram, 'Ionic glasses: History and challenges,' *Solid State Ionics* **105**, 1 (1998)

9. M.D. Ingram, 'Ionic conductivity and glass structure,' *Philosophical Magazine B* **60**, 729 (1989)

10. J.L. Souquet, 'Ionic transport in amorphous solid electrolytes,' *Annual Review of Materials Science* **11**, 211 (1981)

11. J. Swenson & L. Börjesson, 'Correlation between free volume and ionic conductivity in fast ion conducting glasses,' *Physical Review Letters* **77**, 3569 (1996)

12. V.K. Deshpande, 'Science and technology of glassy solid electrolytes,' IOP Conference Series: Materials Science and Engineering **2**, 012011 (2009)

13. R. Christensen, G. Olson & S.W. Martin, 'Ionic conductivity of mixed glass former 0.35 Na_2O+0.65[xB_2O_3+(1–x)P_2O_5] glasses,' *The Journal of Physical Chemistry B* **117**, 16577 (2013)

14. T.Y. Wei, Y. Hu & L.G. Hwa, 'Structure and elastic properties of low-temperature sealing phosphate glasses,' *Journal Of Non-Crystalline Solids* **288**, 140 (2001)

15. J. Jäckle, L. Piché, W. Arnold & S. Hunklinger, 'Elastic effects of structural relaxation in glasses at low temperatures,' *Journal of Non-Crystalline Solids* **20**, 365 (1976)

16. A. Pradel & M. Ribes, 'Ionic conductive glasses,' *Materials Science and Engineering: B* **3**, 45 (1989)

17. S.W. Martin, 'Ionic conduction in phosphate glasses,' *Journal of the American Ceramic Society* **74**, 1767 (1991)

18. A. Makishima & J.D. Mackenzie, 'Direct calculation of young's moidulus of glass,' *Journal of Non-Crystalline Solids* (1973)

19. F.M. Ernsberger, 'Mechanical properties of glass,' *Journal of Non-Crystalline Solids* **25**, 293 (1977)

20. T. Deschamps, J. Margueritat, C. Martinet, A. Mermet & B. Champagnon, 'Elastic moduli of permanently densified silica glasses,' *Scientific Reports* **4**, (2014)

21. K.M. Heidemann, A. Sharma, F. Rehfeldt, C.F. Schmidt & M. Wardetzky, 'Elasticity of 3d networks with rigid filaments and compliant crosslinks,' *Soft Matter* **11**, 343 (2015)

22. Y.B. Saddeek, H.A. Afifi & N.S.A. El-Aal, 'Interpretation of mechanical properties and structure of TeO_2–Li_2O–B_2O_3 glasses,' *Physica B: Condensed Matter* **398**, 1 (2007)

23. O.L. Anderson & D.A. Stuart, 'Calculation of activation energy of ionic conductivity in silica glasses by classical methods,' *Journal of the American Ceramic Society* **37**, 573 (1954)

24. U. Hoppe, D. Stachel & D. Beyer, 'The oxygen coordination of metal ions in phosphate and silicate glasses studied by a combination of x-ray and neutron diffraction,' *Physica Scripta* (1995)

25. E.M. Lifshitz, L.P. Pitaevskii & V.B. Berestetskii, 'Landau-lifshitz course of theoretical physics,' *Statistical Physics* (1980)

26. D. Mcelfresh & D.G. Howitt, 'Activation enthalpy for diffusion in glass,' *Journal of the American Ceramic Society* **69**, C 237 (1986)

27. G.D. Gatta, S.D. Jacobsen, P. Vignola, G. J. McIntyre, G. Guastella & L.F. Abate, 'Single-crystal neutron diffraction and raman spectroscopic study of hydroxylherderite, $CaBePO_4$ (OH, F),' *Mineralogical Magazine* **78**, 723 (2014)

CHAPTER 7

ORGANIC-INORGANIC HYBRID ELELCTROLYTES

7.1 Introduction

Polymer-based solid electrolytes with high ionic conductivity are highly desired for application in lithium ion batteries. Polymer based electrolytes have several advantages over conventional liquid electrolytes such as improved safety, high energy density, the ability to process them into thin films, and the ease of control over shape and size. PEO-based polymer electrolytes attracted a lot of attention as the material for this application because of its stability in contact with lithium metal, good solvation power and its ability to form complexes with alkali metals such as lithium.[1–3] However, because ion conduction occurs predominantly within amorphous region of the polymer as a liquid-like motion of the cation assisted by the segmental reorientation, the semi-crystallinie nature of PEO limits the conductivity of the electrolytes, especially at low temperatures. Furthermore, the mechanical strength of solid polymer electrolyte is far lower than desired to suppress the lithium dendrite growth on the anode.

As mentioned in chapter 4, introducing nanoparticles is one effective strategy to improve the ionic conductivity. However, the composite material derived from that still suffers from poor mechanical strength. The problem of

dispersion and particle agglomeration limits the amount of the particles that can be effectively incorporated.[4] Alternatively, organic-inorganic hybrid materials, which have an organic ion conducting polymer and a stiff inorganic phase, with the two components covalently bonded to each other, provide potential advantages over physically mixed composite materials such as good thermal, mechanical and chemical stability.[5–8] Our materials design target is to simultaneously combine the strong solvation power from the polymer, mechanical rigidity, and the wide electrochemical stability window from the inorganic network.

In this study, we use PEO containing a desired amount of dissociated lithium salt as the ion conducting organic phase and the silica as the inorganic phase. Silica is selected because it is mechanically strong and has a wide electrochemical stability window, which does not limit the overall cell potential. Sol-gel synthesis is commonly used as low temperature processing route for silica materials. By using functionalized alkoxysilanes, organic species can be covalently bonded to the silica backbone.

As a baseline reference for comparison with the hybrid materials, we also fabricated a composite consisting of a polymer-silica blend. To this end we also used the sol-gel method for the hydrolysis and condensation of the silica precursors without functional groups, while a low molecular weight polyethylene glycol was present in the solution. However, for this type of material, phase separation is a concern.[9] Incorporating more than 60% polymer typically results in phase separation. Moreover, only short chain polymer or oligomer can be

blended into the solution because longer chain polymers require a large amount of solvent, which limits the condensation of the process and inhibits gelation.

Therefore, chemical bonding between the organic-inorganic phase is necessary in order to achieve full control over materials design aspects such as organic/inorganic ratio, molecular weight of polymer, bonding types between the two phases. In this study, two synthesis routes are explored, both involving sol-gel reactions of functionalized alkoxysilanes. The first method is a so-called one pot method in which the organic and inorganic precursors are combined before hydrolysis and condensation. Our design strategy is to start with coupling silane with homobifunctional polymer, which results in an organoalkoxysilanes hybrid precursor, so that both ends of the polymer are able to interact with inorganic precursors. Conversely, we investigate hybrids that use monofunctional polymer, which leaves one side of the polymer unattached and, thus, affording it higher segmental mobility. Later, we compare them to hybrids derived by a second synthesis route, in which a highly porous but percolating inorganic phase is formed before infiltrating it with reactive organics. With this two-step method, a continuous silica network is ensured, with organic phases filling in the pores of network. A complete systematic study of the effects of polymer molecular weight, organic-to-inorganic ratio, and degree of bonding between the organic and inorganic phases on various material properties, especially ionic conductivity, are discussed as well as the structure-property relationships.

7.2 Experimental

7.2.1 Materials

Poly(ethylene glycol) (PEG M_w 200, 400, 1000, 2000, 4000, 8000, 10000, 20000, Aldrich), poly(ethylene glycol) methyl ether (MPEG M_w 350, 550, 750, 2000, 5000, Aldrich), Methoxy Polyethylene Glycol Amine (MPEG-NH_2 Mw 2000, 5000), 3-Isocyanatopropyl)triethoxysilane (IPTS, Aldrich), 3-Glycidyloxypropyl) trimethoxysilane (GLYMO, Aldrich), tetraethyl orthosilicate (TEOS, Aldrich), hydrochloric acid (HCl, Aldrich), ammonium hydroxide (NH_3OH, Aldrich) and ethanol (200 proof, Fisher) were used as purchased. Lithium perchlorate ($LiClO_4$, Aldrich) was dried at 120°C for 72h in vacuum prior to use.

7.2.2 Synthesis of Hybrid Materials

All chemical reagents are commercially available (Aldrich) and were used without further purification. PEG-silica-$LiClO_4$ were synthesized using two different methods, the one-pot method and the two-step method. For hybrid materials derived by either method, the resulting materials are rubbery, transparent, and free-standing films.

7.2.3 One-Pot Synthesis Method

Hybrid precursors are synthesized before the sol-gel reaction. Precursors are made by reacting a saline coupling agent, namely a functionalized saline to a functionalized polymer. In particular, mixing IPTS and PEG at a molar ratio of 2:1 results in PEG with two triethoxysilane attached to the end of the chain. Mixing poly(ethylene glycol) methyl ether (MPEG) with IPTS at a molar ratio of

1:1 results in PEG with triethoxysilane attached to only one side of the chain. Both precursors were made at 90°C through the alcoholysis reaction between the isocyanate group and the hydroxyl groups on the polymer, which yields urethanes.[10] The desired quantity of $LiClO_4$ salt is added to the hybrid precursor and is stirred for 20 hours. In this study, we use a lithium concentration of EO/Li=10 throughout the investigation, which was found to give reasonably high conductivities during our preliminary investigations. We use Fourier transform infrared (FTIR) to monitor the reaction until completion, which is evidenced by total disappearance of the isocyanate peak at 2270 cm^{-1}.

Two types hybrid materials based on the two aforementioned hybrid precursors are prepared, one with both sides of the polymer chains covalently bonded to silica backbone (PEG-silica series) and the other one with only one side of the polymer chain bonded to silica (MPEG-silica series). For both hybrid materials, the hybrid precursors and tetraethyl orthosilicate (TEOS) are dissolved in ethanol with EtOH/Si-O=1.5, which controls the PEG weight fraction in the sample. Distilled water (H_2O/Si-O=1) is added upon stirring, and HCl is added as a catalyst with HCl/Si-O=0.005. After 24h, NH_4OH is added with NH_4OH/HCl=3 to finish the acid-base catalyzed sol-gel process. After vigorous stirring for 30 minutes, the sol is poured into polystyrene mold, where gelation occurs after a time ranging between 10 minutes to several hours. The gel is aged for 24 h and extracted from the mold. The samples are then washed with ethanol for 72 hours with fresh ethanol changed every 24 hours. Finally, samples are dried at ambient conditions for 5 days to allow the slow evaporation of ethanol, and

subsequently at 55 ˚C for 3 days in an vacuum oven to obtain the PEG-silica-$LiClO_4$ xerogel. A schematic of the structure of the PEG-silica is shown in Figure 7 - 1. The MPEG-silica series are similar but with one side of the polymer chains free to move. Here, we use P and MP to indicate the polymer molecular weight for the PEG-silica and MPEG-silica series and W to indicate the polymer weight fraction in the two series.

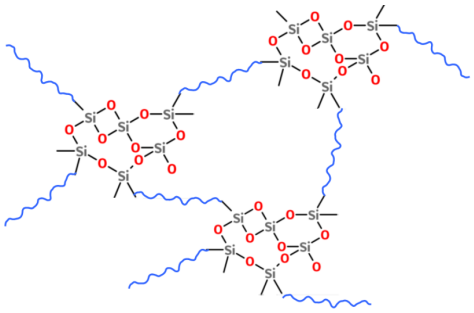

Figure 7 - 1 Schematic of hybrid materials synthesized with one-pot method

7.2.4 Two-Step Synthesis Method

In this process, an inorganic silica network is created first using the sol-gel route. TEOS and a desired amount of silane coupling agent, in this study GLYMO, is dissolved in ethanol. H_2O is added upon stirring with a H_2O/ Si-O =1. An acid base catalysis method similar to the one used in the one-pot method is used. In the meantime, MPEG-NH_2 is dissolved into ethanol along with $LiClO_4$ at EO/Li ratio of 10. After gelation, the wet gel is taken out and washed with ethanol before submerging into the polymer-salt solution to allow for solvent exchange. The glycidyl groups grafted on the silica backbone react with the amine groups on the polymer chains to anchors the polymer chain on the silica

network. After a week, the swelled gel is taken out washed with ethanol for multiple times to wash off unreacted species. The drying process is similar to that of the one-pot method. TGA was performed for each sample to verify the organic content because this solvent exchange is a diffusion driven process and whether full control of the polymer weight fraction is not obvious *a priori*, since the polymer uptake depends on silica structure, polymer solution concentration, polymer chain length, etc.

7.2.5 Impedance Spectroscopy

Ionic conductivities were measured with NovoControl Broadband impedance spectroscopy analyzer. All samples were measured from 293K to 413K with amplitude of 10 mV and in the frequency range between 10 mHz and 10MHz. Samples of ~20 mm diameter and ~1 mm thickness were sandwiched in between two stainless steel electrodes. Measurements are done with both increasing and decreasing temperature form 20˚C to 120˚C.

7.2.6 Brillouin Light Scattering

We use Brillouin light scattering to measure the elastic properties of the hybrid materials. In our experimental setup, we use a Coherent Verdi solid-state laser with a wavelength of 532 nm to illuminate the samples at incident powers of 40 mW or less. The spectrum of scattered light is analyzed using a Sandercock six-pass Tandem Perot Fabry-Pérot interferometer and the interpretation of the spectrum is based on the generalized hydrodynamic theory. The frequency shifts, ω, is related to the velocity of the propagating sound waves in the scattering medium *c* as $\omega = qc$, where *q* is the wavevector of the probed phonon.

In our experimental setup, hybrid materials samples are fabricated as flat discs with parallel surfaces, which allows us to use the so-called platelet geometry where the incident light enters and the scattered light exits the sample through parallel faces, and the sample plane bisects the incident and scattered direction. As in platelet geometry, [11, 12] the phonon wavevector can be calculated by $q = 2sin\alpha/\lambda_0$, where $\lambda_0$is the wavelength of the incident light and the α is the angle between the incident light and the plane normal of the sample. From that the sound wave velocity can be calculated,

Eq. 7-1 $$c = \frac{\omega}{q} = \frac{\omega\lambda_0}{2sin\alpha},$$

The elastic storage modulus, is derived from the density of the sample and the sound velocity

Eq. 7-2 $$\mathrm{M}'(\omega) = \rho_0 c^2 = \frac{\rho_0\omega^2}{q^2}$$

7.2.7 Differential Scanning Calorimetry (DSC)

DSC measurements were performed using a TA 2000 calorimeter. Samples were cooled down to –70°C and measurements were performed up to 150°C with a heating rate 20°C /min for two runs. Glass transition temperatures, Tg, were determined from the midpoint of the experimental curve step.

7.2.8 SAXS

The small angle X-ray scattering measurements of all hybrid xerogels were obtained at the beam line 12-ID-B at the Advanced Photon Source (APS) at Argonne National Laboratory (ANL). All samples were solid xerogel that were dried completely and stored in a desiccator right before the measurement. The

X-ray wavelength was λ = 0.62 Å, and the scattering intensity was averaged over 5 measurements and is expressed as a function of the Q. Q is the scattering vector Q = (4π/λ), where λ is the wavelength of the X-rays, and 2θ is the scattering angle. Measurements were performed across the 0.004 $Å^{-1}$ < Q < 1.03 $Å^{-1}$ region. The exposure time for each sample was 0.5 s, and the scattered X-rays (12 keV) were registered by a CCD detector. The scattered intensity has been corrected for absorption and instrument background. Glassy carbon is used to calibrate all data in absolute intensity.[13] The "Irena" package for SAXS data analysis, "Unified Modeling" module was used to determine scatterer size and size distributions.[14]

7.3 One-Pot Derived Hybrids

The objective of this work is to explore the effect of PEG chain length and weight fraction on various characteristics of the PEG-Silica-$LiClO_4$ hybrid material, including thermal properties, ionic conductivity, mechanical properties, and structure. Results for the one-pot derived hybrids are presented first, and subsequently they are compared with the ones for two-step derived samples.

7.3.1 X-ray Diffraction

X-ray diffraction measurements were performed to investigate the crystallinity of the hybrid material, which is a key factor in ionic conductivity in polymer. Figure 7 - 2 show XRD patterns for pure initial materials $LiClO_4$, MPEG and the samples with different polymer molecular weight. Silica as part of the component is not shown here as is known that the sol-gel

derived silica structures are amorphous. Characteristic peaks in the diffraction patterns shown for $LiClO_4$, MPEG show that they are semi-crystalline. The XRD for hybrid MPEG-silica samples with different polymer molecular weight show a very broad peak centered at 22˚. This indicates that the hybrid samples are amorphous even with 70 wt % of the polymer embedded. A similar behavior is observed for the PEG-silica series. Moreover, all the peaks attributed to crystalline $LiClO_4$ disappear once the salt is dissolved in the hybrid samples, which confirms that $LiClO_4$ as the lithium source is fully dissociated with in the solid hybrid material.

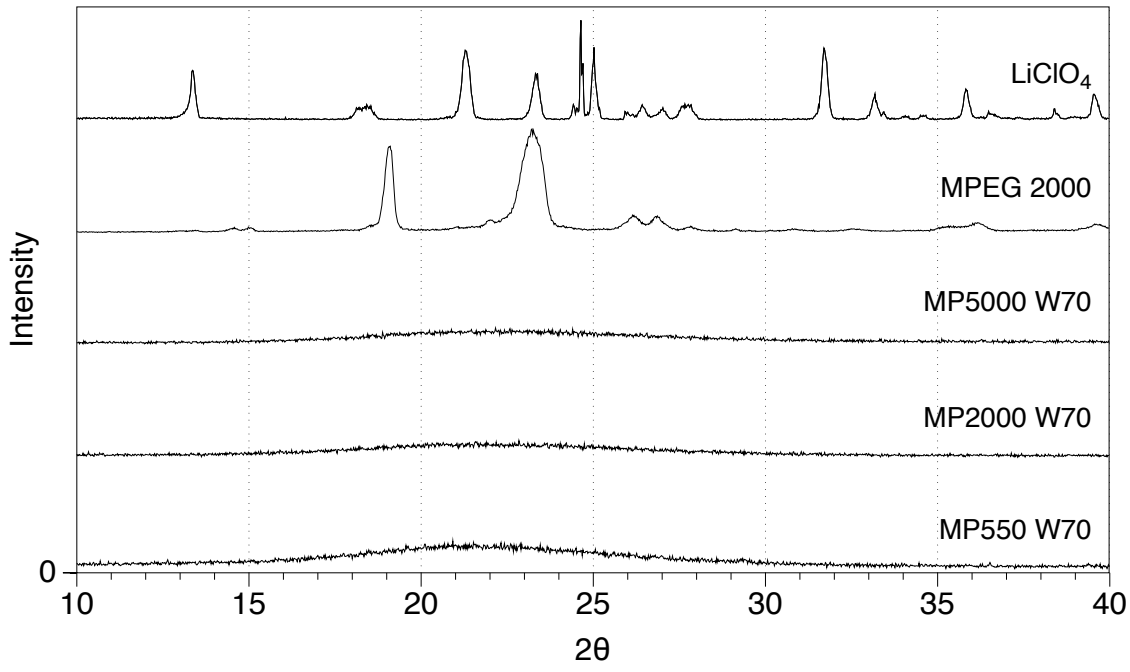

Figure 7 - 2 XRD patterns of $LiClO_4$, MPEG and hybrid MPEG-silica samples with Mw 5000,2000 and 550.

7.3.2 Thermal Properties

Glass transition temperatures of polymer materials reveal information related to segmental mobility, which directly affects the ion transport and mechanical properties of these materials. Figure 7 - 3 shows the DSC isotherms for hybrids with different PEG weight fractions and chain lengths. The glass transition temperature, T_g, is determined as the midpoint of the transition range between the two flat regions of the temperature trace. Figure 7 - 3(a) shows PEG-silica hybrids with different PEG weight fractions. The effect of the PEG weight fraction on T_g can be clearly seen. T_g decreases monotonically from 6.2˚C for W30 to -41.9˚C for W70 and the transition is more discernable with increasing PEG content. Figure 7 - 3(b) shows temperature traces for the MPEG-silica series containing different PEG Mw. Hybrids with higher polymer Mw generally have lower glass transition temperatures, because longer chains have higher segmental mobility. The glass transition is sharper and lower for high PEG concentrations, which indicates that relaxation time distribution is narrower. The observed broader glass transitions at low PEG weigh fractions and with small PEG Mw might be due to PEG silica interactions, which cause a difference in the relaxation times of PEG chains. T_g is usually tentatively associated with the chain mobility in a polymer. It is therefore expected that the mobility of polymer is higher with more PEG and high Mw PEG. No other thermal events are observed above T_g, including melting endotherm, which confirms the amorphous nature of the polymer phase.

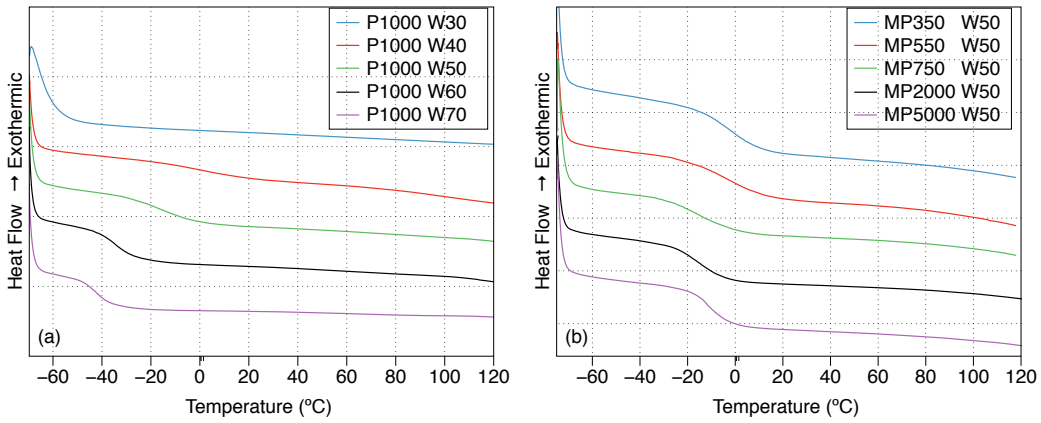

Figure 7 - 3 DSC thermal trace for (a) PEG-silica series with increasing PEG weight fraction b) MPEG-silica series with increasing polymer chain length.

7.3.3 Ionic Conductivity

Figure 4 - 4 (a) shows a representative Nyquist plot for sample MP750 W60 at two different temperatures, with a depressed semicircle at high frequencies that represents the bulk material conductivity and a tilted spike at lower frequency due to diffusion of the ions to the electrodes.[15] We use a standard parallel RC circuit with a Warburg element added in series with the resistor to fit the curves. The diameter of the semicircle decreases with increasing temperature, as the resistance of the electrolytes decreases. An example of a more detailed temperature dependence of hybrids for MP750 is presented as Arrhenius plots in Figure 5b, showing a noticeable deviation from linear in the ionic conductivity dependence on the reciprocal temperature. The ionic conductivity increase with increasing polymer weight fraction for both series, because the polymer phase is the ion conducting phase. For example, MEPG-silica series with polymer Mw 750, the ionic conductivity increase by four orders of magnitude at 40°C with polymer weight fraction from W40 to W80. The

temperature dependence doesn't follow Arrhenius behavior strictly. However, it follows the VTF (Vogel-Tamman-Fulcher) temperature dependence,

$$\text{Eq. 7-3} \qquad \sigma(T) = AT^{-1/2}\exp\left(\frac{-B}{R(T-T_0)}\right)$$

which is a modified Arrhenius equation commonly observed in polymer based ionic conductor, indicating that the ion mobility is originated from chain segmental motion. [4, 16–18] In this equation, A is a pre-exponential factor and B is the pseudo activation energy. The activation energy is calculated from the fitting of the VTF equation. For this MP750 example, activation energy decrease from about 100 kJ/mol at W40 to about 65KJ/mol at W80 (Figure 7 - 4(c)). Similar trend holds for both PEG-silica and MEPG-silica series with various PEG Mw. These findings indicate that more PEG will be preferred for the hybrid electrolyte because it is the PEG phase that act as the main ion conduction phase.

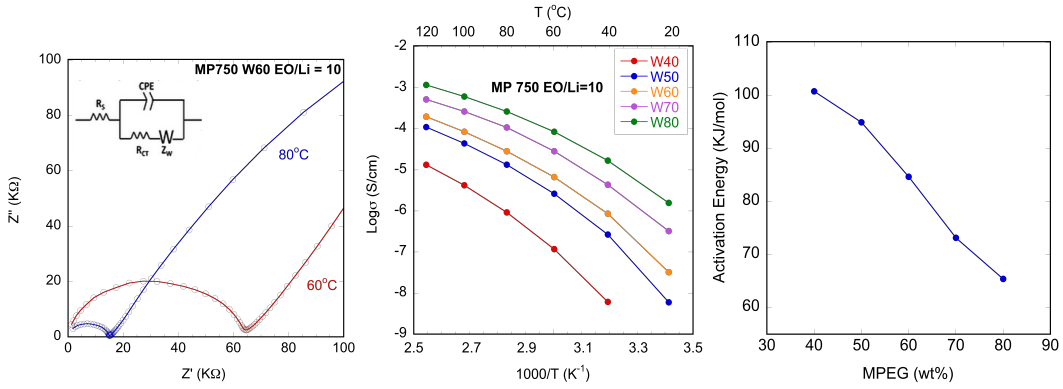

Figure 7 - 4 (a) A representative Nyquist plot with equivalent circuit (b)Arrhenius plot for MPEG 750 with different PEG weight fraction and b) calculated activation energy.

Figure 7 - 5 demonstrate the effect of polymer Mw for both the MPEG-silica and PEG-silica series on ionic conductivity. Similar general trends are observed that the conductivity increases with increasing polymer Mw. For PEG-silica series

the conductivity fluctuates with small changes when Mw increases up until 2000. Then conductivity increase sharply with Mw. MPEG-silica series on other other hand, demonstrate a general increasing trend with increasing Mw, plateaus at Mw 5000. Since the mobility is from the chain reorientation, shorter polymer chains have smaller degree of freedom, especially when then end of the polymer chains are fixed to inorganic phase. For higher Mw polymer, however, the chain mobility reaches a maximum when individual chains are entangled together and the mobility of segments are less effected by the end groups. This is represented as the plateaus in Figure 7 - 5 at high Mw.

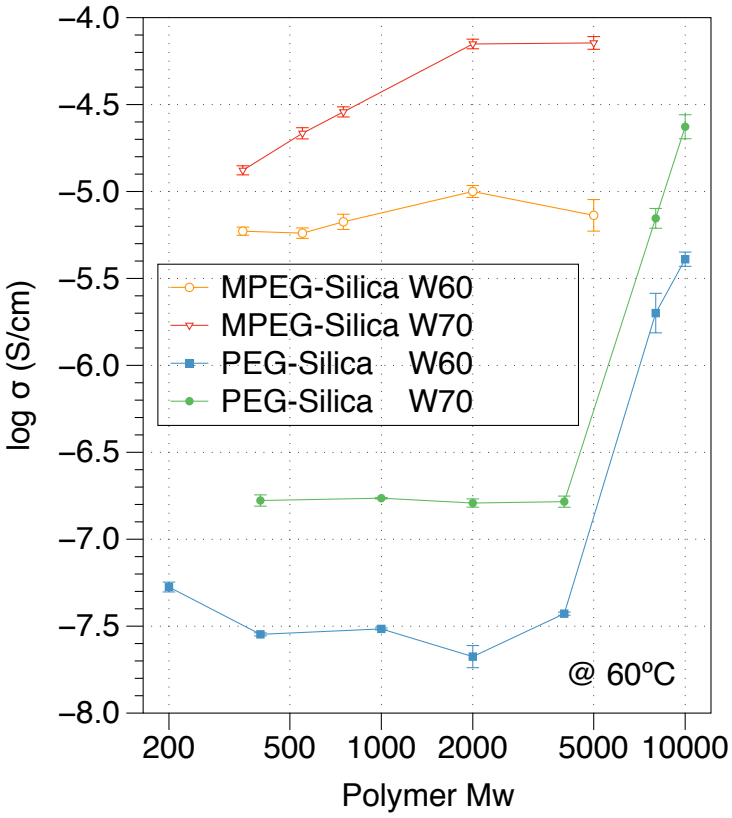

Figure 7 - 5 The effect of molecular weight on ionic conductivity for PEG-silica and MPEG-silica series.

Comparing the two series, MPEG series show more than two orders of magnitude higher conductivities than that of PEG-silica series at similar polymer Mw and weight fraction. The observed enhancement in MPEG-silica series indicate that if one side of the polymer is left to move freely, the mobility is higher which increase the ionic conductivity, while the whole structure is still fully amorphous. Another possible reason is that the polymer segments that are close to the end groups being anchored to the silica may not have much degree of freedom to move. So considering the part of polymer that can move effectively, for the same Mw, the PEG-silica series have smaller fraction of such effect segments than the MPEG-silica series. On the other hand, this also confirms that anchoring one side of the polymer has strong enough effect on limit tendency to form crystallinity. And the amorphous nature of silica phase might also play a role in helping suppressing crystallinity.

7.3.4 Mechanical Properties

Figure 7 - 6 shows the density data for PEG-silica-$LiClO_4$ and MPEG-silica-$LiClO_4$ with 50 wt. %, 60 wt. % and 70 wt. % for various polymer Mw. The density decreases with the increasing polymer weight fraction because polymer has a lower density than silica. The density for PEG-silica series increases with polymer molecular weight. This suggests that as polymer chain length becomes longer, the packing of the polymer is slightly more effective. chain entanglement may have helped compact in the silica matrix. For MPEG-silica series, density initially decreases with chain length, reaching a minimum at Mw = 750, and then

increases for larger chain lengths. This may indicate that polymer chains that are too short have small flexibility for entanglement leave more free volume.

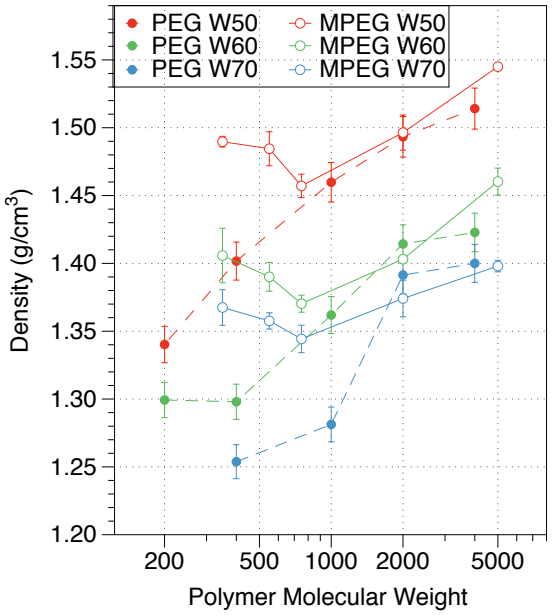

Figure 7 - 6 Density of PEG-silica and MPEG-silica series. Density increase with polymer weight fraction.

BLS was used to measure the longitudinal and shear moduli of the samples. For sol-gel derived material, the mechanical properties are largely affected by the degree of shrinkage, residual solvent and network microstructure. All the gels are dried completely before the Brillouin scattering measurement to make sure that samples fabricated following different synthesis route are comparable. Figure 7 - 7 shows the elastic moduli of the PEG-silica and MPEG-silica hybrid series with different polymer weight fraction. Similar to conventional composite materials, for hybrids, the modulus decreases with the increase of polymer contents. The effect of polymer Mw, however, is not as obvious. By a slight margin, the hybrids with longer chains demonstrate a better performance, which is more discernable

at low polymer concentrations. Comparing the elastic property of the MPEG-silica and PEG-silica series, they are within a similar range, neither one is showing an obviously better performance. For both series of hybrids, the elastic moduli are higher than that of reported values for silica-PEO composites with similar ratio,[19–22] although most of the studies are on PEO with much higher molecular weights and very few studies have been done on PEG-silica hybrid materials with high silica concentrations due to the poor miscibility of these two materials.[23, 24] Our novel materials provide examples for hybrid solids with lower PEG Mw and of reasonably high elastic modulus without phase separation.

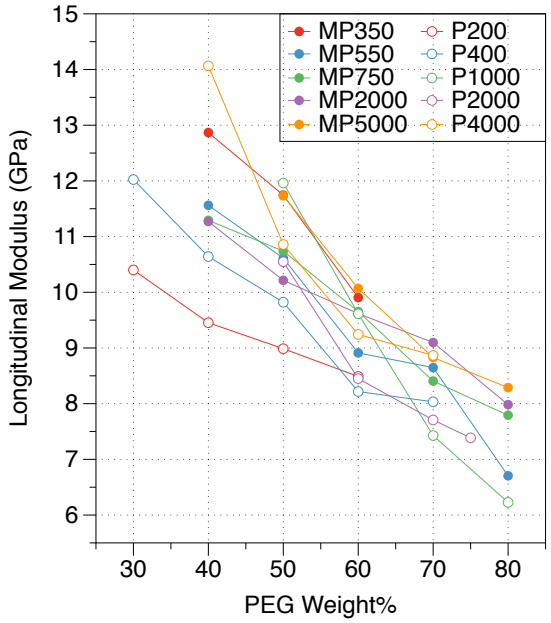

Figure 7 - 7 The longitudinal adiabatic modulus of PEG-silica and MPEG-silica series.

7.3.5 Structural Characterization

To fully understand the origin of aforementioned properties, better information about structural characteristics most be known. All the materials we

fabricated are highly transparent and rubbery, which indicates there are no particle or clusters larger than visible light wavelength. Because sample materials were subject to gelation, a continuous network exists throughout the system. Several microstructures are possible for such silica-hybrid materials in which covalent bonds exist between the organic and inorganic phases. In terms of phase connectivity, depending on their relative volumetric proportions, either the polymer is embedded in the inorganic network, silica clusters are embedded in a polymer matrix, or percolating organic and inorganic networks are mutually interpenetrating each other. In terms of microstructure, the fact that covalent bonds exist between the organic and inorganic phases ascertains homogeneity even at the molecular scale. Conversely, a simple blend of the two phases, as is the case for the aforementioned reference composite, could easily result in the separation between silica rich and polymer rich phases.

Structural characterizations are done using SAXS and TEM in a complementary way. Figure 7 - 8 (a) shows a dark field TEM image of one-pot derived hybrid sample P20000W50. Small bright clusters are embedded in a dark background. The EDS results show that the heaviest element is silicon which should appear as brightest spots. Therefore silica phase forms small clusters homogeneously distributed throughout the polymer backbone in the xerogel. Some other studies on different organic-silica hybrid materials report the development of similar microstructures when organic and inorganic phases are mixed during the sol-gel process.[19, 25–27] With this knowledge, SAXS is used to further examine the feature sizes of the samples.

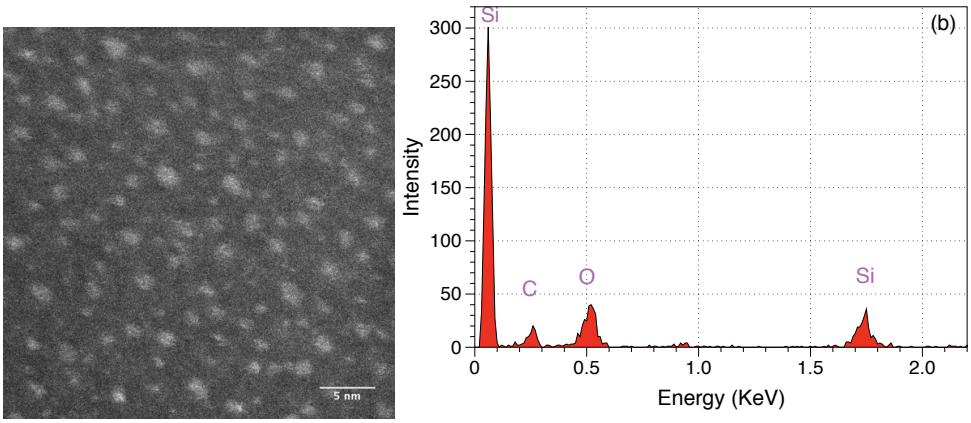

Figure 7 - 8 a) TEM image and b) EDS results of hybrid sample P20000W50.

Figure 7 - 9 (a) shows the SAXS spectra for P10000 with different polymer contents, from W40 to W80. Figure 7 - 9(b) shows the SAXS spectra for PEG-silica series with polymer Mw from 200 to 35000. Similarly, the effects of polymer weight fraction and polymer Mw on structure for MPEG-silica series are presented in Figure 7 - 9 (c) and (d). All spectra exhibit a single peak with the peak maximum shifting towards smaller wavenumbers, q, when the polymer concentration or polymer chain length increases, which indicates an increase in feature size. In SAXS the contrast is relative, this feature can be either polymer or silica or air. However, peaks usually indicate strong spatial correlation resulting from periodic fluctuation in electron density. The interference effects weaken as the feature size increase, since the left side of the peak becomes flatter and eventually becomes negative in slope. As revealed by TEM imaging, clusters of silica form in the polymer matrix. We therefore interpret the position of the SAXS peak to correspond to the spacing between silica rich clusters. Moreover, the spatial correlation of the clusters, which is represented as interference structure factor, becomes weaker the larger the spacing between

clusters. Based on this interpretation, the average and most probable distance between silca clusters can be estimated by $d = 2\pi/Q_{max}$. Accordingly, spacing for the P20000W50 sample is about 2.0 nm, which agrees with the intercluster spacing observed in TEM.The average intercluster distance as a function of polymer weight fraction and polymer Mw is presented in Figure 7 - 10. Polymer with larger molecular weight causes the silica clusters to farther separate, suggesting that the polymer chains prefer self-entanglement over enveloping the silica clusters.

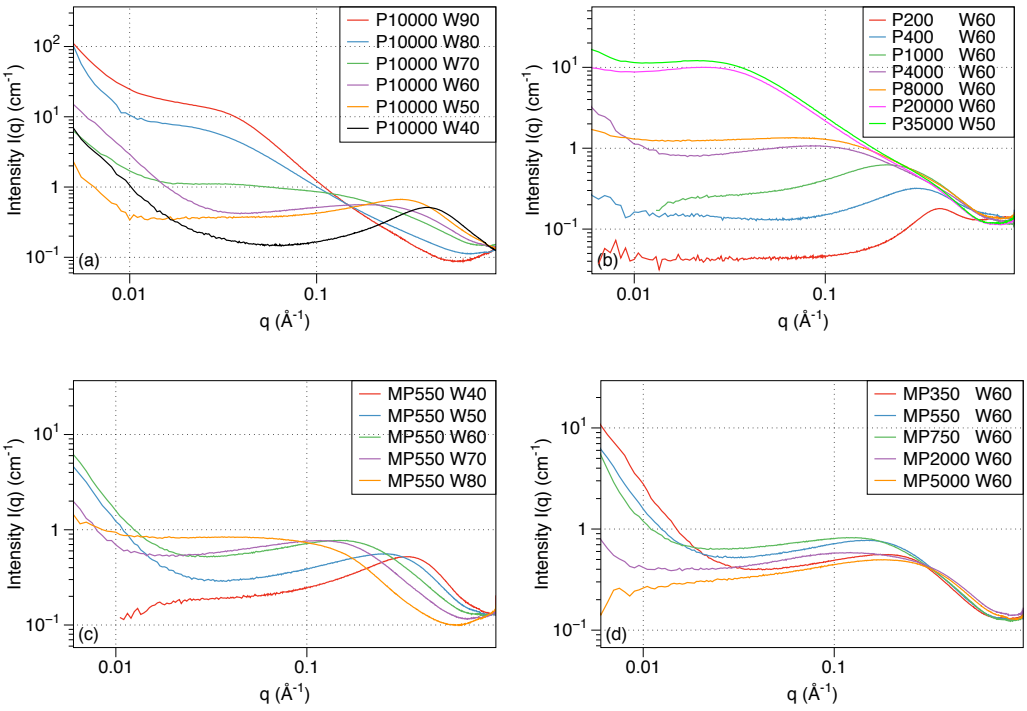

Figure 7 - 9 SAXS spectra for (a) P10000 with various polymer fraction b) PEG-silica series with different polymer molecular weight at W60 (c) MP550 series with various polymer fraction (d) MPEG-silica series with different polymer molecular weight.

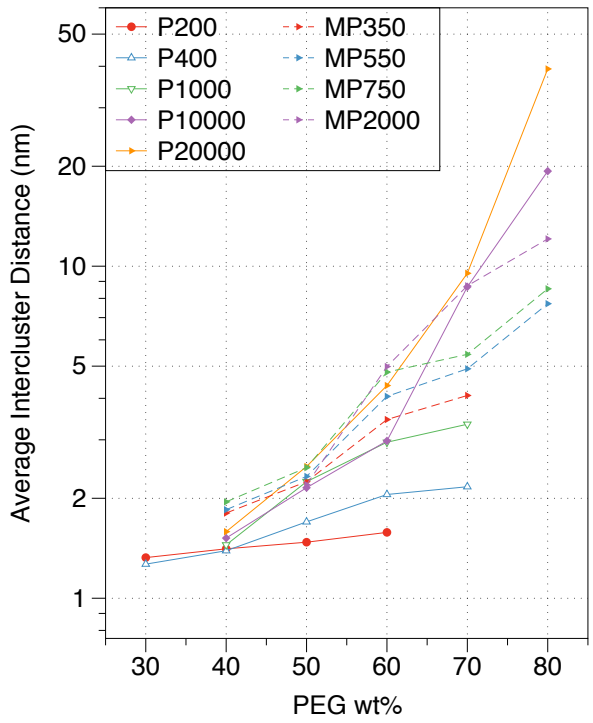

Figure 7 - 10 Average intercluster distance as a function of polymer weight fraction for different polymer Mw.

7.4 Two-step Derived Hybrids

The two-step synthesis method is developed with the purpose of fabricating hybrid materials containing a silica backbone that is continuous and percolates in three dimensions. In comparison to the material obtained using the one-pot method, with the two-step synthesis we expect to achieve a wider electrochemical stability range and higher elastic moduli, by making full use of the structural benefits associated with the stiff and chemically inert silica network, without compromising ionic conductivity by controlling the pore size. The materials design approach is to first create the silica backbone while controlling pore size through solution chemistry, and then insert the polymer and allow it to covalently bond to silica.

7.4.1 Chemical Characterization

FTIR and Raman are used to monitor the reaction process. In the epoxide-primary amine reaction, the epoxide ring that has been grafted onto the silica network is opened by a nucleophilic NH_2 group at the end of the short chain polymers. Organosilane GLYMO shows the signal from epoxide group Ring-stretch ("breathing") at 1254 cm^{-1}, and stronger asymmetric ring deformation and symmetric ring deformation at 908 and 855 cm^{-1}. The IR spectrum of final hybrid product contains no peaks from epoxide, which establishes that reaction took place. Higher resolution Raman spectroscopy is used to further verify if all the reactive sites are completely reacted. However, the epoxy peak overlaps with the shoulders of other peaks in the hybrid, so it can not be fully ascertained that all sites are reacted as designed. In fact, it is likely that there remain unreacted residual sites within the silica network, which are buried in the network and not easily accessed by polymer.

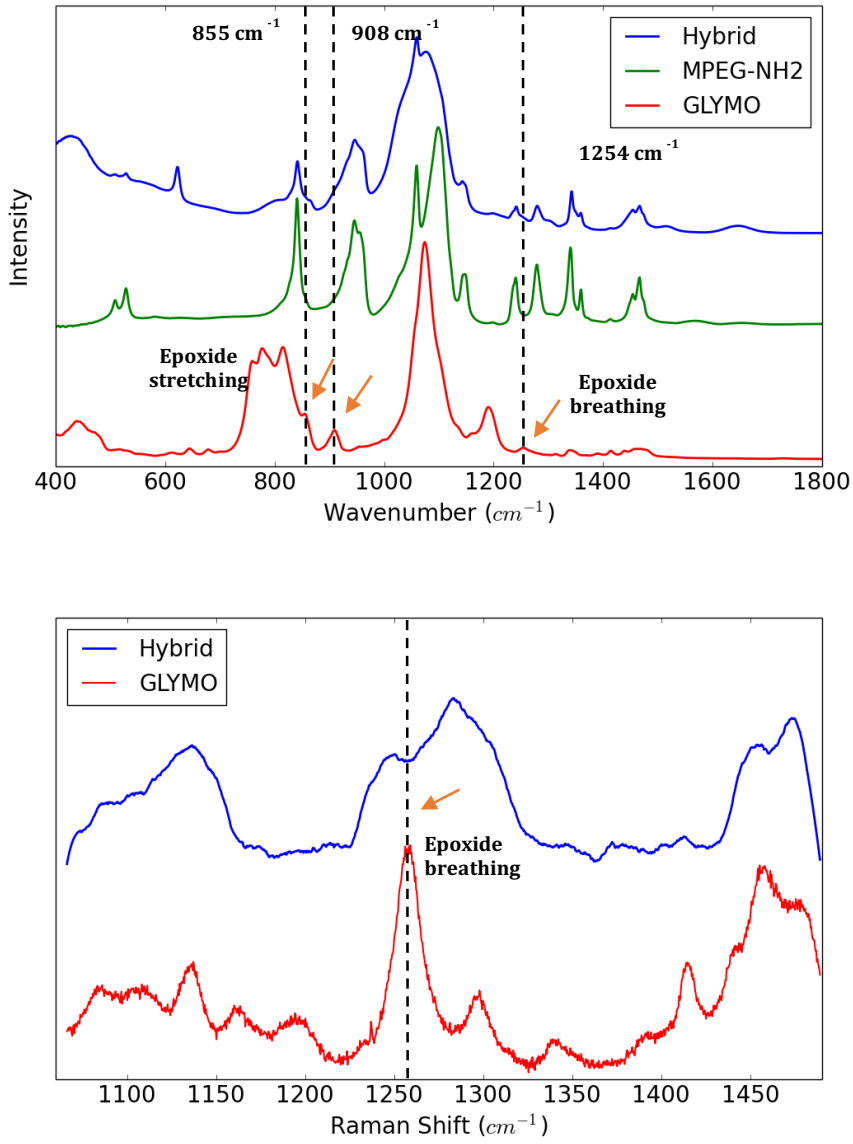

Figure 7 - 11 FTIR and Raman spectra of two-step hybrid system.

7.4.2 Ionic Conductivity

The effect of polymer content on ionic conductivity is shown in Figure 7 - 12 (a). The conductivity generally follows the VTF temperature dependence and the conductivity increases with the amount of polymer embedded. Compared to the hybrids derived with one-pot method with similar polymer Mw, the conductivity-

polymer weight fraction relation follows the same trend at a fixed temperature. This indicates that the shape of PEG phases and its connectivity with inorganic have almost no effect on the conductivity of hybrid materials. Furthermore, with the same amount of polymer in the hybrids, the one-pot and two-step methods produce materials with comparable ionic conductivity. However, with the two-step method, at least 10 wt. % more polymers can be incorporated. Based on our results for the one-pot derived hybrids, more polymer phase is desired to achieve higher conductivity, and accordingly the two-step synthesis approach allows us to drive ionic conductivity up by half an order of magnitude with 10 wt. % more PEG.

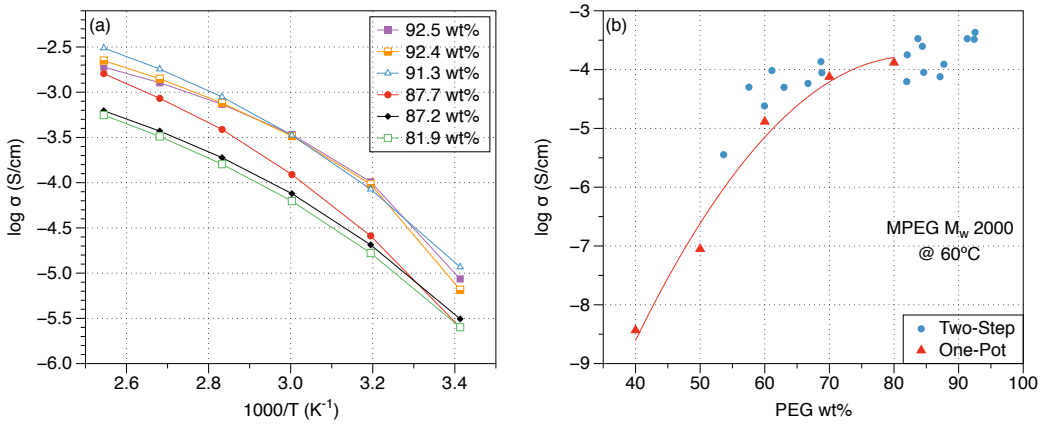

Figure 7 - 12 a) Arrhenius plot for two-step derived hybrid materials with different PEG weight fraction. b) effect of PEG weight fraction on ionic conductivity for one-pot and two-step derived hybrids.

7.4.3 SAXS

For the two-step hybrids, the SAXS spectra exhibit no distinct peaks. Instead, they display a generally decreasing slope with increasing *q*. Such behavior indicates that no dominant particles size exists within this range. From the synthesis procedure, it is known that the continuous silica network is formed

before hybridization with polymer. Log I(q) vs. log q plots are shown in Figure 7 - 13, the slope in the Porod region corresponds to the exponent in Porod's law, which vary between -1.73 to -3.

Eq. 7-4 $$\lim_{q\to\infty} I(q) \propto S' \quad q^{-(6-d)}$$

This suggests that at least one component of the hybrid material assumes the geometry of a self-similar mass fractal object. Correspondingly, fractal geometry with relatively low fractal dimensions are characteristic for low-density silica network structures. For sol-gel derived silica phase catalyzed with acids, the quasi-linear growth of inorganic network is favored due to the PH value of the reaction condition.[28]

It is also discernable in some of the spectra that more than one size scales are present. At smaller *q* value, the large feature are the polymer phases embedded in the pores. At larger q value, the small features are the mass fractal of the network.

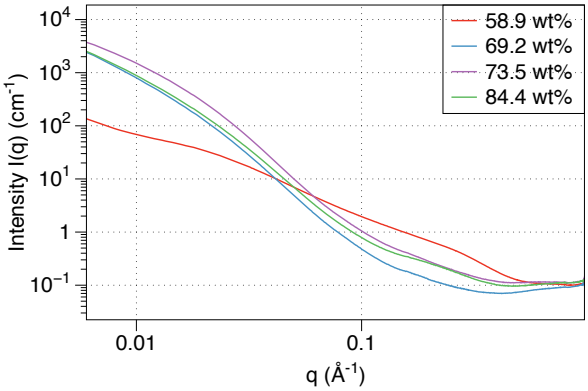

Figure 7 - 13 SAXS spectra of two-step derived hybrids show mass fractal structures.

7.4.4 Mechanical Properties

In the two-step synthesis, the polymer solution infiltrates the pores when the gel is wet, and therefore, the silica backbone remains continuous after hybridization. TGA results show that more polymer can be accommodated by the silica network pores, without disturbing the connectivity in this phase, compared to the one-pot method, in which silica poly-condensation and grafting of the organic chains occurs simultaneously. With large polymer weight fraction the resulting gel consists of an inorganic framework with open pores filled with polymer. It can be viewed as a modified "aerogel", with air replaced by polymer. In the field of aerogel research, polymers are often considered a reinforcement for the silica aerogel.[29–33] So the effect that the amount and molecular weight of polymer has on the elastic properties of the hybrid material are of interest.

We measured the density and elastic moduli of the samples. Incorporating the organic species into the inorganic network is a diffusion driven process, which also depends on the pore structure of the silica network, the concentration of reactive groups in solution, the pressure, and the temperature at which the reaction takes place. This constitutes a wide parameter space to control, and given the relative novelty of our materials synthesis approach, learning to navigate this parameter space resulted in data with significant scatter wide margins of certainty. The relative proportions of organic and inorganic species in each sample is determined with TGA measurement.

The densities are roughly within the same range as those of the one-pot derived samples. However, the density shows a very weak dependence on

polymer concentration compared to the behavior of the one-pot derived hybrids. So instead of developing a higher density when more polymer is embedded in the pores of preformed network, because the gel is still surrounded by solution it is actually capable of adjusting the pore sizes when different amounts of polymer is anchored to the backbone, so that it always ends up with a self-optimized structure. Similarly, the measured moduli data exhibit significant scatter. Many variables in sol-gel processing affect the rigidity of the final network. Although they are characterized by a different microstructure, the elastic moduli of the one-pot derived and the two-step derived hybrids fall within the same range of magnitude. Although it is still in the early stage of material development and full control over the materials properties is not yet achieved, even with as much as 95% polymer, the longitudinal modulus is above 7 GPa, which is definitely higher than most of the other reported polymer composites and even the one-pot derived hybrid materials.

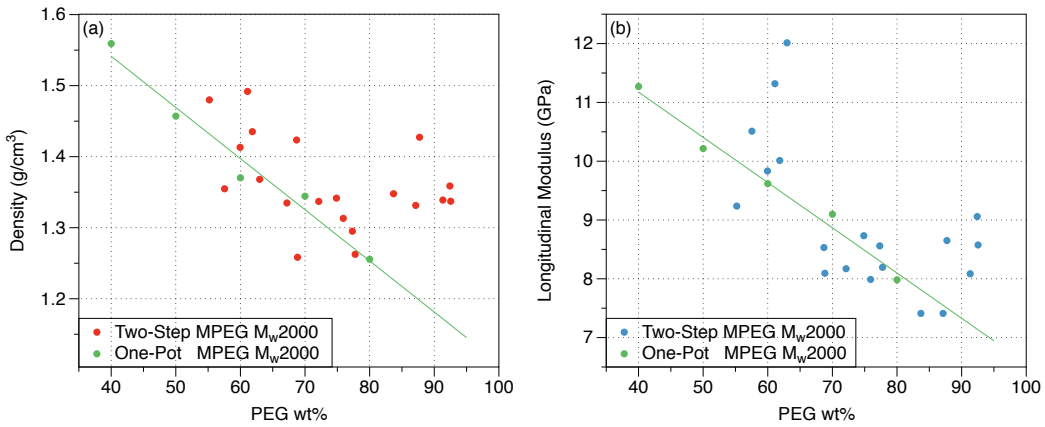

Figure 7 - 14a) Density and b) longitudinal modulus of two-step derived hybrids.

Although the microstructure of the one-pot and the two-step derived hybrids are completely different, the effect of polymer molecular weight and the polymer concentration on various properties are similar. The main advantage of the two-step method is that it provides the opportunity to incorporate more polymer while still maintaining a continuous network structure. Therefore, it has great potential for further material development. As an ion conductor, the present hybrid electrolytes still have modest ionic conductivity at room temperature. Even though it is not comparable to that of liquid electrolyte, our system shows increasing conductivity with increasing polymer weight fraction and chain length. More importantly, the fact that the mechanical properties and the ionic conductivity appear to be largely decoupled, resolves a major materials design impasse with polymer based electrolytes,[34] which is that chain mobility and mechanical rigidity exhibit opposing trends. Independent control over mechanical and transport behaviors provides the opportunity for optimizing the two properties separately. For the two-step derived hybrid, the structure of the inorganic framework can be controlled via the solution chemistry, so that if a more open structure with more accessible functional groups are preformed, more polymer can be incorporated. Many factors can affect the structure of the silica phase, though the kinetics of hydrolysis and condensation, including acid and base catalysts, type and amount of solvents, water : alkoxide ratio. Some other parameters, such as lithium concentration, type of counter anion, chemical bonding between polymer and silica network, have not been optimized yet in this

current study. Overall, the hybrid materials offer outstanding mechanical thermal stability and promising ionic conductivity.

7.5 Conclusions

There are many benefits of introducing covalent bonds between organic inorganic phase to fabricate hybrids. By simple blending, the resulting materials have only one type of microstructure, which is polymer matrix with particles embedded. Even though particle sizes and volume fractions can be varied, the structure and property control is still limited. By introducing covalent bonds between organic and inorganic phases, the structure can be modified via processing conditions and the chemistry of the precursors for the sol-gel synthesis.

This study focus on the material development of PEG-silica hybrid electrolytes, with silica being the structural phase and PEG with the dissolution of $LiClO_4$ being the ionic conducting phase. The present study confirms that hybrid electrolytes fabricated by the sol-gel method not only have purely amorphous structure as desired, but also demonstrate good mechanical and thermal properties. Two different series of hybrids are synthesized using the one-pot method, the PEG-silica series and the MPEG-silica series. The effects of polymer Mw and polymer weight fraction on mechanical, thermal, conductivity, and structure are investigated. Our results show that MPEG-silica series demonstrate several orders of magnitude higher conductivity due to the greater freedom for segmental motion in the polymer chains. Additionally, it is found that larger polymer concentration and longer chain lengths are desired for better ionic

conductivity. With a two-step process, in which the organic phase is incorporated into a preformed inorganic network during a second step, a larger weight fraction of polymer can be achieved.

SAXS and TEM results show that silica rich clusters form in the one-pot derived samples with the distance between such clusters increase with polymer chain length and weight fraction, while a three-dimensional continuous silica network forms in the two-step derived hybrids, which is reflected by the characteristic features of mass fractals in the SAXS spectra. Comparable effects of polymer weight fraction on conductivity are observed although the hybrids possess a very different microstructure. The mechanical properties of the hybrids derived by either method have a similar dependence on the polymer weight fraction and molecular weight. More importantly, both types of hybrid show higher elastic moduli than most previously reported composites with similar organic-inorganic ratio, and with even higher polymer molecular weight.

As an ion conductor, the room temperature conductivity is not yet high enough for practical application as solid-state electrolyte. However, the decoupling of the ionic conductivity from the mechanical properties are unique in our system, which offers the opportunity to tune parameters so as to maximize both mechanical stiffness and ion mobility. The development of hybrid electrolytes for practical use in advanced rechargeable lithium batteries is therefore highly likely.

7.6 References

1. D.E. Fenton, J.M. Parker & P.V. Wright, 'Complexes of alkali metal ions with poly (ethylene oxide),' *Polymer* **14**, 589 (1973)

2. Gray F.M. 1991. *Solid Pmer Electrolytes*. VCH New Tork etc.

3. P.V. Wright, 'Electrical conductivity in ionic complexes of poly (ethylene oxide),' *Polymer International* **7**, 319 (1975)

4. W. Wang, E. Yi, A.J. Fici, R.M. Laine & J. Kieffer, 'Lithium ion conducting polyethylene oxide-based solid electrolytes containing active or passive ceramic nanoparticles,' *The Journal of Physical Chemistry C* (2017)

5. K. Dahmouche, M. Atik, N.C. Mello, T.J. Bonagamba, H. Panepucci, M.A. Aegerter & P. Judeinstein, 'Investigation of new ion-conducting ormolytes: Structure and properties,' *Journal of Sol-Gel Science and Technology* **8**, 711 (1997)

6. H.M. Kao & C.L. Chen, 'An organic–inorganic hybrid electrolyte derived from self assembly of a poly (ethylene oxide)–poly (propylene oxide)–poly (ethylene oxide) triblock copolymer,' *Angewandte Chemie International Edition* **43**, 980 (2004)

7. H.-M. Kao, T.-T. Hung & G.T.K. Fey, 'Multinuclear solid-state NMR characterization, ion dissociation, and dynamic properties of lithium-doped organic- inorganic hybrid electrolytes based on ureasils,' *Macromolecules* **40**, 8673 (2007)

8. M.M. Silva, S.C. Nunes, P.C. Barbosa, A. Evans, V. De Zea Bermudez, M.J. Smith & D. Ostrovskii, 'Sol–gel preparation of a di-ureasil electrolyte doped with lithium perchlorate,' *Electrochimica Acta* **52**, 1542 (2006)

9. B.M. Novak, 'Hybrid nanocomposite materials—between inorganic glasses and organic polymers,' *Advanced Materials* **5**, 422 (1993)

10. G. Raspoet, M.T. Nguyen, M. Mcgarraghy & A.F. Hegarty, 'The alcoholysis reaction of isocyanates giving urethanes: Evidence for a multimolecular mechanism,' *The Journal Of Organic Chemistry* **63**, 6878 (1998)

11. M. Aldridge, C. Shankar, C. Zhen, L. Sui, J Kieffer, M. Caruso a& J, Moore, 'Combined experimental and simulation study of the cure kinetics of DCPD' *Journal of Composite Materials* (2010)

12. J. Krüger, L. Peetz & M. Pietralla, 'Brillouin scattering of semicrystalline poly (4-methyl-1-pentene): Study of surface effects of bulk and film material,' *Polymer* (1978)

13. F. Zhang, J. Ilavsky, G.G. Long, J.P.G. Quintana, A.J. Allen & P.R. Jemian, 'Glassy carbon as an absolute intensity calibration standard for small-angle scattering,' *Metallurgical and Materials Transactions A* **41**, 1151 (2010)

14. J. Ilavsky & P.R. Jemian, 'Irena: Tool suite for modeling and analysis of small-angle scattering,' *Journal of Applied Crystallography* **42**, 347 (2009)

15. A.K. Arof, S. Amirudin, S.Z. Yusof & I.M. Noor, 'A method based on impedance spectroscopy to determine transport properties of polymer electrolytes,' *Physical Chemistry Chemical Physics* **16**, 1856 (2014)

16. N.K. Karan, D.K. Pradhan, R. Thomas, B. Natesan & R.S. Katiyar, 'Solid polymer electrolytes based on polyethylene oxide and lithium trifluoro-methane sulfonate (peo–licf 3 so 3): Ionic conductivity and dielectric relaxation,' *Solid State Ionics* **179**, 689 (2008)

17. M.G. Mclin & C.A. Angell, 'Ion-pairing effects on viscosity/conductance relations in raman-characterized polymer electrolytes,' *Journal of Physical Chemistry* **95**, 9464 (1991)

18. Y. Tominaga, V. Nanthana & D. Tohyama, 'Ionic conduction in poly (ethylene carbonate)-based rubbery electrolytes including lithium salts,' *Polymer Journal* **44**, 1155 (2012)

19. P. Hajji, L. David, J.F. Gerard, J.P. Pascault & G. Vigier, 'Synthesis, structure, and morphology of polymer–silica hybrid nanocomposites based on hydroxyethyl methacrylate,' *Journal of Polymer Science Part B: Polymer Physics* **37**, 3172 (1999)

20. H.J. Walls, J. Zhou, J.A. Yerian, P.S. Fedkiw, S.A. Khan, M.K. Stowe & G.L. Baker, 'Fumed silica-based composite polymer electrolytes: Synthesis, rheology, and electrochemistry,' *Journal of Power Sources* **89**, 156 (2000)

21. J. Xu, W. Shi & W. Pang, 'Synthesis and shape memory effects of Si–O–Si cross-linked hybrid polyurethanes,' *Polymer* **47**, 457 (2006)

22. E. Burgaz, 'Poly (ethylene-oxide)/clay/silica nanocomposites: Morphology and thermomechanical properties,' *Polymer* **52**, 5118 (2011)

23. P.P. Chu, M.J. Reddy & H.M. Kao, 'Novel composite polymer electrolyte comprising mesoporous structured SiO_2 and PEO/Li,' *Solid State Ionics* **156**, 141 (2003)

24. M.J. Reddy & P.P. Chu, '7 Li NMR spectroscopy and ion conduction mechanism in mesoporous silica (SBA-15) composite poly (ethylene oxide) electrolyte,' *Journal Of Power Sources* **135**, 1 (2004)

25. C.J.T. Landry, B.K. Coltrain, M.R. Landry, J.J. Fitzgerald & V.K. Long, 'Poly (vinyl acetate)/silica filled materials: Material properties of in situ vs fumed silica particles,' *Macromolecules* **26**, 3702 (1993)

26. K.A. Mauritz, ‘Organic-inorganic hybrid materials: Perfluorinated ionomers as sol-gel polymerization templates for inorganic alkoxides,’ *Materials Science and Engineering: C* **6**, 121 (1998)

27. D. Tian, S. Blacher & R. Jérôme, ‘Biodegradable and biocompatible inorganic–organic hybrid materials: 4. Effect of acid content and water content on the incorporation of aliphatic polyesters into silica by the sol-gel process,’ *Polymer* **40**, 951 (1999)

28. B.L. Cushing, V.L. Kolesnichenko & C.J. O’connor, ‘Recent advances in the liquid-phase syntheses of inorganic nanoparticles,’ *Chemical reviews* (2004)

29. M.A.B. Meador, C.M. Scherzer, S.L. Vivod, D. Quade & B.N. Nguyen, ‘Epoxy reinforced aerogels made using a streamlined process,’ *ACS Applied Materials & Interfaces* **2**, 2162 (2010)

30. G. Zhang, A. Dass, A.-M.M. Rawashdeh, J. Thomas, J.A. Counsil, C. Sotiriou-Leventis, E.F. Fabrizio, F. Ilhan, P. Vassilaras & D.A. Scheiman, ‘Isocyanate-crosslinked silica aerogel monoliths: Preparation and characterization,’ *Journal of Non-Crystalline Solids* **350**, 152 (2004)

31. J.P. Randall, M.A.B. Meador & S.C. Jana, ‘Polymer reinforced silica aerogels: Effects of dimethyldiethoxysilane and bis (trimethoxysilylpropyl) amine as silane precursors,’ *Journal of Materials Chemistry A* **1**, 6642 (2013)

32. Y. Duan, S.C. Jana, B. Lama & M.P. Espe, ‘Reinforcement of silica aerogels using silane-end-capped polyurethanes,’ *Langmuir* **29**, 6156 (2013)

33. Y. Duan, S.C. Jana, B. Lama & M.P. Espe, ‘Self-crosslinkable poly (urethane urea)-reinforced silica aerogels,’ *RSC Advances* **5**, 71551 (2015)

34. J.F. Snyder, R.H. Carter & E.D. Wetzel, ‘Electrochemical and mechanical behavior in mechanically robust solid polymer electrolytes for use in multifunctional structural batteries,’ *Chemistry of Materials* **19**, 3793 (2007)

CHAPTER 8

CONCLUSIONS AND FUTURE WORK

8.1 Conclusions

This research focused on the materials development of solid ion conducting materials for battery electrolyte applications. Work has been performed on three types of materials, Li+ ion conducting PEO-nanocomposites, Na+ conducting mixed network former glasses and Li+ conducting organic-inorganic hybrid materials. Through the work presented in this thesis, we have identified the key parameters and design criteria in each type of material. Major findings are concluded as follows:

(1) PEO-nanocomposite electrolytes incorporating LATP active ceramic nanoparticles demonstrate remarkably higher ionic conductivity than those incorporating passive particles. This enhancement is attributed to cation transport within the interphase region surrounding the particles, which achieves percolation at low nanoparticle loading. The development of this interphase structure is influenced by the active nature of the LATP filler, and the inherent conductivity of the interphase is estimated to be three to four times higher than the maximum measured value.

(2) For NBS and NBG glasses, in addition to non-linear, non-additive mixed-glass former effects, maxima are observed in longitudinal, shear and Young's moduli with increasing atomic number density. A statistical thermodynamic model based on reaction balances between various network species is formulated. Combining the NMR data of boron species and the adiabatic elastic modulus, the model can be applied to calculate the molar fraction of all SRO structural units, including the ones for Ge species. This new analysis reveals that the structural characteristic predominantly responsible for effective mechanical load transmission in these glasses is a high density of network cations coordinated by four or more bridging oxygens, as it provides for establishing a network of covalent bonds among these cations with connectivity in three dimensions.

(3) The ionic conductivities in our NBS and NBG glasses exhibit non-linear, non-additive mixed network former behavior, and a Vogel-Tamman-Fulcher temperature dependence. Strong correlation exists between bulk modulus and the negative logarithm of the ionic conductivity, which essentially amounts to activation energy for ion conduction. An approach that expands upon the Anderson-Stuart model is used to describe the cation migration mechanisms, in which the activated process involves a jump by the migrating particle and transient reversible displacement of atoms in the immediate vicinity of the cation. Accordingly, a cation jump affects the motion of between 20 and 30 surrounding

atoms. Furthermore, it is observed that elastic deformations in the affected volume are almost purely hydrostatic and hardly shear.

(4) For NBS and NBG glasses, the activation energy is provided by thermal phonons in the materials. Because the energy must be concentrated momentarily in a space within the affected volume via localized superposition of phonons with different wavelengths, for the same degree of phonon localization, stiffer networks require a higher phonon energy. Similarly, more localized energy requires the superposition of phonons extending to higher frequencies and shorter wavelengths. So, the more compliant the structure and the larger the affected volume, the higher the ionic conductivity. Moreover, larger numbers of atoms may provide more choices for creating a passable configuration for the cation; the energy concentration can then be achieved with the superposition of fewer and lower-energy phonons.

(5) In organic-inorganic hybrid materials, two different synthesis routes are used. One-pot synthesized hybrid samples have ionic conducting polymer as the matrix with nano-sized silica particles embedded, while two-step derived hybrids have a continuous silica network as the structural backbone and polymer in the pores of this network. For one-pot derived electrolytes, we observe that the ionic conductivity increases with the concentration of PEG and PEG molecular weight to an extent. Compared to hybrids with both sides of the PEG chains anchored to the inorganic phase, the ionic conductivity increases when only one side of the PEG chain is anchored. Although ionic conductivity dependences on PEG weight fraction and PEG molecular weight are similar, the two-step method allows the

incorporation of more PEG while maintaining reasonably high mechanical stability.

8.2 Future Work

Materials with high ionic conductivity are desirable for their applications in all-solid-state batteries. Based on the knowledge of ion conducting mechanisms in PEO-nanocomposites and mixed-network former glasses, organic-inorganic hybrid materials have been developed which show potential for more suitable electrolytes in this application. Some possible directions for future research to further enhance desired material properties are presented here.

(1) For PEO-nanocomposite electrolytes with active nanoparticles such as LATP, due to the existence of highly conductive interphase, ionic conductivity can be maximized through complete dispersion of a larger nanoparticle loading, so that all bulk polymer is converted to interphase. Proper dispersants must be identified, or appropriate chemical surface modification may need to be performed on the particles to minimize particle-particle interactions while not perturbing the formation of a highly conductive interphase. For example, tethering the particle with PEG oligomer could help dispersion while maintaining interphase.

(2) For mixed-network-former glasses, the bulk moduli are strongly correlated with the ionic activation energy and ionic conductivity. Suppression of dendrite growth, however, relies more on the shear moduli of the electrolytes. The design of materials that provide low bulk moduli while maintaining reasonably high shear moduli could be the next focus in glassy electrolyte development.

(3) In the study for organic-inorganic hybrid materials, perchlorate anions were used as the counter ion for Li^+ to have low anion mobility. However, a lithium salt with a larger anion such as bis(trifluoromethane)sulfonimide lithium (LITFSI) may provide better performance. Furthermore, if the anion is anchored within the backbone, the transference number would be further improved.

(4) Another issue when using the two-step synthesis method is the difficulty in controlling the organic-to-inorganic material ratio. A controlled parametric study could be performed to map out this ratio depending on different combinations of the time and temperature of the solvent exchange process in the second step.